CARBON NANOSHEETS AND CARBON NANOTUBES BY RF PECVD

A Dissertation
Presented to

The Faculty of the Department of Physics
The College of William and Mary in Virginia

In Partial Fulfillment
Of the Requirements for the Degree of

Doctor of Philosophy

---

by

Mingyao Zhu

September, 2006

Reproduced with permission of the copyright owner. Further reproduction prohibited without permission.

APPROVAL SHEET

This dissertation is submitted in partial fulfillment of
the requirements for the degree of

Doctor of Philosophy

Mingyao Zhu

Approved by the Committee, September 2006

Dennis M. Manos, Chair

Brian C. Holloway

William J. Kossler

Anne C. Reilly

David W. Thompson
Department of Chemistry

Reproduced with permission of the copyright owner. Further reproduction prohibited without permission.

Dedicated to my parents and my husband

Reproduced with permission of the copyright owner. Further reproduction prohibited without permission.

TABLE OF CONTENTS

Acknowledgements ix

List of Tables x

List of Figures xii

Abstract xxiv

Chapter 1: Introduction 2

1.1 Introduction to carbon nanostructures and PECVD 2

1.2 Organization of dissertation 6

Chapter 2: Characterization Tools for Carbon Nanostructure Material Analysis 11

2.1 Introduction 11

2.2 Scanning electron microscopy (SEM) and Energy dispersive X-ray spectroscopy (EDS) 12

2.3 Transmission electron microscopy (TEM) and Selected area diffraction (SAD) 14

2.4 Atomic force microscopy (AFM) 15

Reproduced with permission of the copyright owner. Further reproduction prohibited without permission.

2.5 Raman and FT-IR spectroscopy 17

2.6 X-ray diffraction (XRD) 19

2.7 Auger electron spectroscopy (AES) and X-ray photoelectron spectroscopy (XPS) 20

2.8 Particle induced X-ray emission (PIXE) and elastic recoiled detective analysis (ERDA) 22

2.9 Four-point resistivity measurement 24

2.10 Other characterization methods for applied properties 26

2.10.1 Field emission (FE) measurement 26

2.10.2 Thermal desorption spectroscopy (TDS) 27

2.10.3 Brunauer-Emmett-Teller (BET) surface area measurement 28

2.11 Summary 28

Chapter 3: RF PECVD System Design and Operation Modes 44

3.1 Introduction 44

3.2 RF PECVD system setup 47

3.2.1 RF PECVD system setup 47

3.2.2 Matching network for RF PECVD 49

3.3 Plasma coupling modes and deposition conditions 52

3.3.1 Inductive coupling mode 52

3.3.2 Capacitive coupling mode 53

Chapter 4: CNT Deposition and Properties 62

4.1 Introduction of CNT synthesis 62

4.2 Nanosphere lithography (NSL) for catalyst patterning 64

Reproduced with permission of the copyright owner. Further reproduction prohibited without permission.

4.2.1 Introduction 64

4.2.2 Single-layer and double-layer NSL 65

4.2.3 NSL for carbon nanotube catalyst patterning 67

4.3 Deposition and characterization of CNT 69

4.3.1 Structure and properties of typical CNT 69

4.3.2 CNT deposited under other conditions 70

4.4 Field emission of CNT-based, back-gated devices 72

4.5 Summary 73

Chapter 5: Carbon Nanosheet: Experimental Deposition and Characterization 90

5.1 Introduction of CNS synthesis 90

5.2 Deposition and properties of typical CNS 92

5.2.1 Typical CNS deposition 92

5.2.2 SEM and TEM of typical CNS 92

5.2.3 AES and XPS of typical CNS 94

5.2.4 PIXE, ERDA, and TDS of typical CNS 95

5.2.5 Raman and FTIR of typical CNS 96

5.2.6 X-ray diffraction of typical CNS 99

5.2.7 Field emission of typical CNS 100

5.2.8 Four-point resistivity of typical CNS 102

5.2.9 BET surface area of typical CNS 104

5.3 Parametric study of carbon nanosheet growth 105

5.3.1 Substrate temperature 107

Reproduced with permission of the copyright owner. Further reproduction prohibited without permission.

5.3.2 Methane concentration 108

5.3.3 Input RF power 109

5.3.4 Total gas pressure 110

5.4 Modification and application of carbon nanosheets 111

5.4.1 Aligned CNS deposition 111

5.4.2 CNS from other gas compositions 112

5.4.3 Metal coating on CNS for catalyst support 114

5.4.4 Preliminary results of CNS-based, back-gated field emission devices 114

5.5 Summary 116

Chapter 6: Carbon Nanosheet: Interpretive Model of Growth Mechanism 149

6.1 Introduction 149

6.2 A phenomenological growth mechanism of CNS 150

6.2.1 Optical emission spectra of inductively and capacitively coupled plasma 151

6.2.2 Interpretive model for CNS growth 152

6.2.3 Role of the electric field in CNS growth 155

6.3 Parametric study analysis 156

6.3.1 Substrate temperature 157

6.3.2 Methane concentration 158

6.3.3 Input RF power 158

6.3.4 Total gas pressure 159

6.4 Summary 161

Reproduced with permission of the copyright owner. Further reproduction prohibited without permission.

Chapter 7: Conclusion and Future work 170
7.1 Conclusion 170
7.2 Future work 174
Bibliography 178
Appendix A: Acronyms 184
Vita 187

Reproduced with permission of the copyright owner. Further reproduction prohibited without permission.

ACKNOWLEDGEMENTS

I wish to express my most sincere appreciation to Prof. Dennis M. Manos and Prof. Brian C. Holloway, for their years of patient work with me, valuable criticism and constructive advising, without which this work could not have been done. I am honored to have had the opportunity to study under their guidance.

I am indebted to Dr. Jianjun Wang (now of Intel Inc.) for his unconditional help in each and every step of this research. His knowledge, persistency, and optimism are invaluable to this work. I also want to thank him for being good friend.

Thank my committee members, Prof. William J. Kossler, Prof. Anne C. Reilly, and Prof. David W. Thompson of Chemistry, for agreeing to serve. I especially appreciate their comments on the manuscripts.

I wish to express my gratitude to our research group members, they are: Dr. Ronald A. Outlaw, Dr. Benjamin L. French (now of Intel Inc.), Dr. Xin Zhao, Kun Hou, Dr. Sigen Wang (now of University of North Carolina at Chapel Hill), Dr. Nimel Theodore, Ron Quinlan, and Peter Miraldo.

I also want to acknowledge the exceptional support of the Physics Department, the Department of Applied Science, and the Applied Research Center, especially to Amy L. Wilkerson, Bernadette A. Kulas, Lydia C. Whitaker, Richard Proper, Paula C. Perry, Sylvia Stout, Carolyn Hankins, Natalie Pearcy, and Olga Trofimova. I want to thank Dr. V. Shutthanandan of Pacific Northwest National Lab for his kind assistance with PIXE and ERDA experiments, and Ms. Kerry Siebein of University of Florida for her help on HRTEM. Thanks to Ms. Barbara G. Monteith, for her tremendous help with my dissertation writing.

I would like to thank my friends, Wen Gao, Hui Tian, Xin Zhao, Shuyan Zhang, Haibin Zhao, Zhengmao Zhu, Jing Zhang, Sheng Peng, and Ping Tang, for the great friendship and the unforgettable moments we spent together during the past six years.

Last, I want to express my deepest appreciation to my family. Thanks to my mother, father, and sister, for believing in me, encouraging me, and selflessly supporting me. Special thanks to my husband, for years of love, help, and understanding.

Reproduced with permission of the copyright owner. Further reproduction prohibited without permission.

LIST OF TABLES

Table 1.1: Definition and values of carbon nanotube parameters 10

Table 2.1: List of the techniques used for carbon nanostructure characterization in this work 43

Table 3.1: Comparison of the inductively and capacitively coupled plasma used to synthesize carbon nanosheets and carbon nanotubes in this work 61

Table 4.1: List of calculated values of size and distance of the catalyst dots patterned by single-layer and double-layer nanosphere lithography using spheres with diameters of 419 nm, 269 nm, 171 nm, and 100 nm, respectively 79

Table 5.1: Comparison of typical carbon nanosheet surface area of to that of activated charcoal and the theoretical surface areas of single-, double-, and triple-layered graphite sheets 131

Reproduced with permission of the copyright owner. Further reproduction prohibited without permission.

Table 6.1: Parameters for CNT and CNS deposition in the RF PECVD system 163

Table 6.2: Trends in growth rate and orderliness of CNS as their growth parameters, including substrate temperature, CH_4 concentration, input RF power, and total gas pressure, change 166

Reproduced with permission of the copyright owner. Further reproduction prohibited without permission.

LIST OF FIGURES

Figure 1.1: Structures of fullerene molecules: (a) C_{60}; (b) C_{70}; and (c) C_{80}. (From Dresselhaus, M. S., Dresselhaus, P. C., Saito, R, Endo, M, in *Carbon Nanotubes: Preparation and Properties*, 1997. Reprinted with permission of CRC Press, Inc.) 8

Figure 1.2: (a) A 2-D graphene sheets presenting the parameters specify a nanotube. (b) Structure of a single-walled carbon nanotube with one end detached. (From Dresselhaus, M. S., Dresselhaus, P. C., Saito, R, Endo, M, in *Carbon Nanotubes: Preparation and Properties*, 1997. Reprinted with permission of CRC Press, Inc.) 9

Figure 2.1: Schematic of a scanning electron microscope, illustrating the work principle. (From Reimer, L., in *Scanning Electron Microscopy: Physics of Image Formation and Microanalysis*, 1998. Reprinted with permission of Springer-Verlag.) 29

Reproduced with permission of the copyright owner. Further reproduction prohibited without permission.

Figure 2.2: Secondary electrons (SE), backscattered electrons (BSE), Auger electrons (AE), and X-rays (X) are generated when incident electrons (IE) strike a specimen surface . . . 30

Figure 2.3: A picture of the Hitachi S-4700 FE-SEM at the College of William and Mary . . . 31

Figure 2.4: Schematic diagram of typical TEM with EDS, STEM, and EELS capability. (From Fultz, B. Howe, J. M., in *Transmission Electron Microscopy and Diffractometry of Materials*, 2002. Reprinted with permission of Springer-Verlag.) . . . 32

Figure 2.5: The Joel JEM HR-TEM at the University of Florida's Major Analytical Instrumentation Center (MAIC) . . . 33

Figure 2.6: Schematic view of the principle of tapping mode AFM. The sample symbolized by the circles is scanned by means of a piezoelectric translator . . . 34

Figure 2.7: The Veeco Dimension 3100, located at the Applied Research Center, Newport News, VA . . . 35

Figure 2.8: The inVia dispersive Raman spectroscope at the College of William and Mary . . . 36

Reproduced with permission of the copyright owner. Further reproduction prohibited without permission.

Figure 2.9: Schematics of the diffraction principle (a) and different diffraction geometries (b-d) used in crystalline structure detection. (a): The Bragg relation for the lattice constant, diffraction angle, and the X-ray wavelength. (b): θ-2θ geometry. (c): grazing incidence angle asymmetric Bragg (GIAB) geometry. (d): grazing incidence X-ray scattering (GIXS) geometry 37

Figure 2.10: Schematic diagram of electron emission in Auger (a) and photoelectron (b) processes. Open circles indicate electrons involved in the processes 38

Figure 2.11: (a): Schematic diagram of PIXE setup. (From Johansson, S. A. E., in *Particle-Induced X-Ray Emission Spectrometry*, 1995. Reprinted with permission of John Wiley & Sons, Inc.) (b): ERDA geometry, M, Z, E are the mass, atomic number, and energy of a particle, subscription 1 and 2 represent incident and recoiled particles, α, β, and θ are the incident, recoil, and scattering angles, respectively 39

Figure 2.12: (a) Schematic diagram of a 4-point probe resistivity measurement configuration for an asymmetric film. Metal tips are placed along the sample's circumference. When a current is delivered from tip 1 to tip 2, and the voltage between tips 4 and 3 is measured. (b) An example of contact configurations for a symmetric film shape 40

Figure 2.13: (a) Picture of the 4-point probe at ARC. (b) An enlarged photo of the 4 tips and a standard resistance for calibration 41

Reproduced with permission of the copyright owner. Further reproduction prohibited without permission.

Figure 2.14: Schematic diagram of a typical (a) diode and (b) triode field emission measurement setup 42

Figure 3.1: Schematic of typical parallel plate capacitor RF discharge (RF diodes) system configuration. 55

Figure 3.2 Schematics of high-density (a) Microwave driving ECR, (b) Helicon, (c) Cylindrical inductive RF, and (d) planar inductive RF plasma discharges. 56

Figure 3.3 Schematic of the planar inductively coupled RF PECVD apparatus for carbon nanostructure synthesis 57

Figure 3.4: A picture of the RF PECVD system. Some parts are labeled, others are either blocked or inside of the chamber, therefore, not visible in this picture 58

Figure 3.5: (a) Equivalent circuit of the direct connection of RF power source and the plasma discharge. (b) Equivalent circuit of a matching network placed between the RF source and the discharge 59

Figure 3.6: Schematic diagram of the distribution of the induced electromagnetic field in planar inductively coupled plasma in cylindrical coordinates, as shown on right 60

Reproduced with permission of the copyright owner. Further reproduction prohibited without permission.

Figure 4.1: Schematics showing the nanosphere lithography (NSL) processes 76

Figure 4.2: Schematics of single-layer nanosphere lithography (NSL). Holes between the adjacent spheres are triangular-shaped and form a hexagonal pattern 77

Figure 4.3: Schematics of double-layer nanosphere lithography (NSL). Holes are hexagonal-shaped and form a triangular pattern. 78

Figure 4.4: Top-view (a) and side view (b) AFM images of the 419 nm polystyrene nanospheres spin-coated on a Si substrate. The spheres self assembled to a periodic array. 80

Figure 4.5: Single-layer (a) and double-layer (b) pattern of Ni islands coated on the substrate after removal of the self-assembled polystyrene nanosphere masks, 419 nm in diameter 81

Figure 4.6: AFM images of single-layer (a) and double-layer (b) Ni islands coalesced to round dots after heating and etching in inductive plasma 82

Figure 4.7: SEM images of randomly oriented CNT grown at typical conditions. (a) Low magnification image shows the overall morphology of the CNT. (b) The hexagonal pattern of the Ni catalyst at the root of each CNT. (c) High magnification image indicates a base-growth mechanism of typical CNT 83

Reproduced with permission of the copyright owner. Further reproduction prohibited without permission.

Figure 4.8: High resolution transmission electron micrographic of a typical CNT sample. A hollow center is observed between the parallel fringes, which are parallel to the tube axis 84

Figure 4.9: Raman spectrum of a typical CNT sample. The excitation laser wavelength is 514 nm 85

Figure 4.10: Low magnification (a) and high magnification (b) SEM images of aligned CNT arrays deposited on a SiO_2/Si substrate with +50 V DC bias applied during deposition 86

Figure 4.11: SEM image of a one-dimensional CNT structure deposition using capacitively coupled CH_4/H_2 plasma for 5 minutes. Other conditions are the same as typical CNT depositions 87

Figure 4.12: Schematics of a novel back-gated field emission device, using CNT as the cathode material 88

Figure 4.13: Low magnification (a) and high magnification (b) SEM images of the cathode lines in a CNT-based back-gated device. The street areas between the lines were cleaned by HF dipping 89

Figure 5.1: Representative SEM images of typical CNS deposited with 40% CH_4

Reproduced with permission of the copyright owner. Further reproduction prohibited without permission.

in H_2, at 100 mTorr total gas pressure, 680 °C substrate temperature, and 900 W RF power. (a): Top view image shows the 2-D surface morphology of the CNS. (b): Enlarged image shows the CNS edge is ~1 nm thick. (c): CNS on a curved Ni TEM surface, showing both top and cross-section views. (d): Enlarged image of CNS on curved surface, showing vertical orientation of the CNS. (e): Cross-section view of as-deposited CNS on cleaved SiO_2/Si substrates 118

Figure 5.2: SEM images of CNS deposited on (a): Si, (b): graphite, (c): stainless steel, (d): Ta, (e): Quartz (SiO_2), and (f): Al_2O_3 substrates reveal similar surface morphologies, regardless of the substrate material 119

Figure 5.3: (a) TEM image showing CNS grown directly on a grid. (b)-(d) HRTEM of single pieces of nanosheets showing double parallel fringes with a distance 0.34-0.37 nm at the edge of CNS. (e) The electron diffraction pattern of CNS observed in TEM, matches that of a graphitic structure 120

Figure 5.4: AES (a) and XPS (b) spectra of typical CNS samples have only C features, with a negligible amount of O from absorbed water due to ambient exposure 121

Figure 5.5: PIXE spectra of CNS coated on Si and graphite substrates. The fitted data reveals a Si peak only from CNS on Si substrates. No element is detected for CNS grown on graphite substrates, indicating extremely low contamination Concentrations 122

Reproduced with permission of the copyright owner. Further reproduction prohibited without permission.

Figure 5.6: Both ERDA (a) and TDS (b) measurements indicate large amounts of H incorporated into CNS 123

Figure 5.7: (a) Raman spectrum of typical CNS samples using a 514 nm excitation laser wavelength. The first order peaks and second-order over-tunes are labeled. (b) Low energy peaks observed from typical CNS samples using a 633 nm excitation laser wavelength 124

Figure 5.8: Raman spectra of typical CNS excited by three different wavelength lasers. Note how the position and/or the intensity changes with variation in laser energy/ wavelength 125

Figure 5.9: Representative absorption FTIR spectrum of typical CNS. The C-H stretching vibrational mode and C=C stretching vibrational mode were observed in the spectrum 126

Figure 5.10: Asymmetric glancing angle XRD spectrum of a typical CNS sample. The (101) reflection indicates a crystalline structure 127

Figure 5.11: Two field emission I-V curves of typical CNS showing (a) a turn-on field of ~7.8 V/μm and (b) a total emission current of 28 mA. The insets illustrate corresponding Fowler-Nordheim plots. The straight lines indicate unsaturated exponential field emission behavior 128

Reproduced with permission of the copyright owner. Further reproduction prohibited without permission.

Figure 5.12: The I_{max} *vs.* t curves of two CNS samples showing stable electron emission over (a) 200 hours and (b) 120 hours. No degradation was observed in either sample 129

Figure 5.13: Sheet resistance of CNS on quartz substrates measured by a 4-point probe at various probe currents. The measurements are reproducible for probe currents greater than 3×10^{-5} A 130

Figure 5.14: SEM images of CNS deposited for (a) 90 sec, (b) 2 min, (c) 4 min, (d) 8 min at 680 °C substrate temperature, 100 mTorr total pressure, and 1000 W input RF power. (e): Peeled-off CNS from the sample shown in (d), and (f): magnified image of the area within the red frame in (e) showing the base layer under the vertically oriented sheets 132

Figure 5.15: SEM images of CNS deposited on Si substrates at various substrate temperatures of (a) 630 °C, (b) 655 °C, (c) 680 °C, (d) 730 °C, (e) 780 °C, and (f) 900 °C 133

Figure 5.16: (a) the growth rate and (b) the I_D/I_G ratio in Raman spectrum of CNS deposited at various substrate temperatures 134

Figure 5.17: SEM images of CNS deposited on Si substrates using (a) 10%, (b) 20%, (c) 40%, (d) 60%, (e) 80%, and (f) 100% CH_4 in H_2 135

Reproduced with permission of the copyright owner. Further reproduction prohibited without permission.

Figure 5.18: (a) the growth rate and (b) the I_D/I_G ratio in Raman spectrum of CNS deposited at various CH_4 in H_2 concentrations 136

Figure 5.19: SEM images of CNS deposited on Si substrates at input RF powers of (a) 400 W, (b) 500 W, (c) 800 W, (d) 1000 W, and (e) 1200 W 137

Figure 5.20: The growth rate and the I_D/I_G ratio in Raman spectrum of CNS deposited with different input RF powers 138

Figure 5.21: SEM images of CNS deposited on Si substrates at total gas pressures of (a) 20 mTorr, (b) 50 mTorr, (c) 100 mTorr, (d) 200 mTorr, (e) 300 mTorr, and (f) 400 mTorr 139

Figure 5.22: The growth rate and the I_D/I_G ratio in Raman spectrum of CNS deposited at various total gas pressures 140

Figure 5.23: (a) Schematics of the experimental setup for aligned CNS formation. (b) Schematics showing the area on the substrate where aligned CNS formed, and the direction of the aligned CNS 141

Figure 5.24: SEM images of aligned CNS deposited near the grounded Ta electrode on a heavily doped Si wafer. (a): lower magnification (b): higher magnification images 142

Reproduced with permission of the copyright owner. Further reproduction prohibited without permission.

Figure 5.25: SEM images of sheet-like structure deposited on Si substrates in inductive plasmas from (a) 10%, (b) 20%, (c) 40%, (d) 80%, (e) 80% at a lower magnification, and (f) 100% C_2H_2 in H_2 gases. Other conditions are the same as typical CH_4/H_2 CNS depositions 143

Figure 5.26: SEM images of sheet-like structure deposited on Ni nano-dots patterned Si substrates in inductive plasmas. The gas composition varied from (a) 40%, (b) 60%, and (c) 80% C_2H_2 in NH_3 gases. Other conditions are the same as typical CH_4/H_2 CNS depositions 144

Figure 5.27: SEM images reveal the rough surface morphologies of CNS coated with (a) 2nm Pt and (b) 2 nm Ni via evaporation. (c) TEM micrograph of Pt coated CNS. (d) A high resolution TEM micrograph of Pt coated CNS reveals Pt particles 3-5 nm in diameters 145

Figure 5.28: Schematics of CNS-based "buried line" back-gated triode field emission device 146

Figure 5.29: (a): Top view and (b) cross-section view SEM images of a blanket layer of as-deposited CNS on both the line and the street areas of a back-gated device. (c): Top view and (d): cross-section view SEM images of patterned CNS on the lines only 147

Reproduced with permission of the copyright owner. Further reproduction prohibited without permission.

Figure 5.30: Emission current (*I*) *vs.* the back-gate voltage (*V*) behavior of a CNS-based buried-line, back-gated device. The diode field is fixed at 9 V/μm 148

Figure 6.1: Optical emission spectra for inductively coupled plasma of typical CNS deposition and capacitively coupled plasma for CNT deposition. The collection times were 300 ms and 2000 ms, respectively 164

Figure 6.2: A schematic representing the CNS growth mechanism. C^g = "crystalline" graphitic carbon; C^d = defect site carbon; H= atomic hydrogen 165

Figure 6.3: Peak intensities of the OES for the plasma used for CNS deposition at various CH_4 concentrations. The CH peak intensity increases with CH_4 concentration, while the atomic hydrogen peaks decrease. 167

Figure 6.4: Optical emission peak intensities as functions of the input RF power. (a) All the peaks plotted increase with input RF power, and (b) the atomic hydrogen to growth species intensity ratio also increases with input RF power 168

Figure 6.5: Optical emission peak intensities as functions of the total gas pressure. (a) All the peaks plotted decrease with total gas pressure, and (b) the atomic hydrogen to growth species intensity ratio also decreases with total gas pressure 169

Reproduced with permission of the copyright owner. Further reproduction prohibited without permission.

ABSTRACT

A planar antenna RF plasma enhanced chemical vapor deposition apparatus was built for carbon nanostructure syntheses. When operated in inductive and capacitive plasma discharging modes, two carbon nanostructures, carbon nanotube (CNT) and carbon nanosheet (CNS), were synthesized, respectively.

A nanosphere lithography method was developed and used to prepare catalyst patterns for CNT growth. Using capacitively coupled C_2H_2/NH_3 plasma, randomly oriented CNT were synthesized on Ni dot patterned Si substrates. Aligned CNT arrays were grown on SiO_2 coated Si substrates, using both C_2H_2/NH_3 and CH_4/H_2 capacitive plasmas.

When operated in inductive coupling mode, CNS were successfully deposited on a variety of substrates without any catalyst. Carbon nanosheets are a novel two-dimensional structure, have smooth surface morphologies and atomically thin edges, and are free-standing roughly vertical to substrate surfaces. CNS have a defective graphitic crystalline structure, and contain only C and H elements. Typical CNS growth parameters are 680 °C substrate temperature, 40% CH_4 in H_2, 900 W RF power, and 100 mTorr total gas pressure. Morphology, growth rate, and structure of CNS change with the variations in the growth parameters. Increasing substrate temperature yields a less smooth morphology, a faster growth rate, and more defects in CNS; increasing CH_4 concentration causes a faster growth rate and more defects in CNS, but only slightly changes the morphology; increasing RF power results in a more smooth morphology, a faster growth rate, and less defects in CNS; and decreasing total gas pressure induces a less smooth morphology, a faster growth rate, and more defects in CNS.

In CNS growth mechanism, a base layer forms underneath the vertical sheets; the growth of CNS is through growth species surface diffusion; the electric field near substrate surfaces promotes and keeps the vertical orientation of the CNS, and the atomic hydrogen etching keeps the CNS atomically thin.

Carbon nanosheets have large surface areas, and can stabilize metal thin films into particles 3-5 nm in diameters. For field emission testing, typical CNS have turn-on fields of 5-10 V/μm, a maximum emission current of 28 mA, an emission current density of 2 mA/mm^2, and a life-time of 200 hours.

Reproduced with permission of the copyright owner. Further reproduction prohibited without permission.

CARBON NANOSHEETS AND CARBON NANOTUBES BY RF PECVD

Reproduced with permission of the copyright owner. Further reproduction prohibited without permission.

Chapter 1

Introduction

1.1 Introduction to carbon nanostructures and PECVD

In recent years, many advancements have been made in the downsizing of microstructures to nanostructures. A nanostructure is defined as a structure in which at least one of its three dimensions lies between 1 and 100 nm.[1] If all three dimensions of a nanostructure are of nanometer scale, it is a zero-dimensional (0-D) nanostructure, also known as a quantum dot. Similarly, if two of the three dimensions are of nanometer scale, the nanostructure is one-dimensional (1-D); and if one of the three dimensions is of nanometer scale, it is two-dimensional (2-D). A bulk material is then considered as a three-dimensional (3-D) structure.

Just as its name implies, a carbon nanostructure is a nanostructure composed of carbon atoms. Carbon nanostructures have more than one form; so far, carbon is the only element in the periodic table that has allotropes from 0-D to 3-D. Well-known carbon nanostructures include 0-D fullerenes, 1-D carbon nanotubes (CNT), and 1-D carbon

Reproduced with permission of the copyright owner. Further reproduction prohibited without permission.

nanofibers (CNF). Graphite and diamond are known as 3-D carbon structures. Recently reported carbon nanosheets (CNS)[2] and carbon nanowalls (CNW)[3] are 2-D carbon nanostructures and their syntheses completed the carbon nanostructure family.

In 1985, fullerenes were first synthesized and discovered in laser irradiation vaporized graphite.[4] Fullerenes are hollow spherical or ellipsoidal molecules composed of carbon atoms. Buckminsterfullerene (C_{60}), named after an architect Richard Buckminster Fuller, is a spherical molecule made up of pentagons and hexagons, as presented in Figure 1.1 (a). C_{60} is the smallest feature in which no two pentagons are adjacent; each of the 12 pentagons is surrounded by 5 hexagons. Imaging a C_{60} molecule being split in the middle and 10 carbon atoms being added along the circumference, an ellipsoidal C_{70} molecule is formed, as shown in Figure 1.1 (b). Similarly, the C_{80} molecule (Figure 1.1 (c)) and the molecules in the C_{60+10j} (j=1, 2, ...) family are formed. When j is large enough, a fullerene molecule becomes a single-walled carbon nanotube (SWNT).

Although CNT and CNF had been synthesized earlier,[5,6] Iijima is generally given credit for discovering 1-D carbon nanostructures in 1991 when he adequately characterized and described their atomic structure via transmission electron microscopic observations.[7] Since then, numerous studies have focused on the unique structure and properties of CNT.[6]

A SWNT can be conceptualized by wrapping a planar graphitic network (a graphene sheet) into a seamless cylindrical tube around an axis parallel to the graphene sheet with caps at each end; the two caps then form a fullerene molecule. A SWNT is specified in terms of the diameter d_t and chiral angle θ, which are shown in Figure 1.2,

Reproduced with permission of the copyright owner. Further reproduction prohibited without permission.

where $\boldsymbol{a_1}$ and $\boldsymbol{a_2}$ are the unit vectors of the 2-D crystal lattice of a graphene layer. When forming a cylindrical tube, atom O and A are overlapped, then the chiral vector OA or $\boldsymbol{C_h}$ is defined in term of two integers, (n, m), and θ is the angle between the $\boldsymbol{C_h}$ direction and the zigzag direction of the graphene network. The definitions and values of the parameters describing carbon nanotubes are listed in Table 1.1.

If m=0, the nanotubes are called "zigzag"; if n=m, the nanotubes are called "armchair"; all other nanotubes are called "chiral". A SWNT can be either a semiconductor or a metal, depending on the chiral vector. For a nanotube with a given chiral vector (n, m), if $(2n+m)=3q$, where q is an integer, the nanotube is metallic; otherwise, the nanotube is a semiconductor. All "armchair" nanotubes are metallic.

Multi-walled carbon nanotubes (MWNT) are structures similar to SWNT but are formed from concentric cylinders wrapped from multi-layered graphene sheets. As in the case for graphite, the adjacent layers of the cylinder are connected by *van der Walls* forces, and the distance is close to the in-plane distance in bulk graphite.

Conceptually, 2-D CNS are just individual graphene layers of graphite. For many years, the ideal 2-D model has been widely used in theoretical calculations for graphite related materials. However, the experimental synthesis of the 2-D material was not achieved until recently. Sheet-like graphitic material was first observed in SWNT production, and then synthesized as by-products in CNT deposition. Our group was one of the first to report the synthesis of pure 2-D carbon nanostructures.[2]

Chemical vapor deposition (CVD) is a chemical process used for the deposition of thin films of various materials. In typical CVD, one or more gas phase reactants decompose and react at a substrate surface to produce the desired deposit. CVD is widely

Reproduced with permission of the copyright owner. Further reproduction prohibited without permission.

used in the semiconductor industry as part of the device fabrication process to deposit various thin film materials.

Various types of CVD are widely used; plasma enhanced CVD (PECVD) is one of the most commonly used. PECVD utilizes plasma to increse the chemical reaction rates of the reactants; therefore PECVD processing allows deposition at lower temperatures, which is often critical in the manufacture of semiconductors.

CNT were initially synthesized by arc-discharge and laser ablation methods, usually at high temperatures of 3000-4000 °C. Later, the PECVD system was adopted and used in CNT syntheses due to its substantially lower temperature and its capability to grow aligned and ordered nanotubes with control. Now, both MWNT and SWNT can be deposited via PECVD methods.

Carbon nanosheets have been obtained by other researchers via various methods, including arc discharge,[8] microwave CVD,[3,9] hot filament CVD,[10,11] RF PECVD,[12] mechanical exfoliation,[13,14] and some chemical routes.[15] We designed and built a planar antenna radio frequency (RF) PECVD system, and successfully synthesized two carbon nanostructures — CNS and CNT — in one system when operated in inductive and capacitive discharge modes.

The 2-D CNS synthesized in our RF PECVD system have the thinnest edges among all reported structures. Carbon nanosheets with only two atomic layers at the edges were commonly observed under a high resolution transmission electron microscope. The CNS are free-standing off substrate surfaces. Furthormore, CNS growth needs no catalyst, therefore no metallic contaminations were detected from CNS, the CNS growth is not self-limited, and mass production of CNS can be easily achieved.

Reproduced with permission of the copyright owner. Further reproduction prohibited without permission.

The systhesis of the noval 2-D nanosheets fills in the gap between low dimensioal (0-D and 1-D) and bulk (3-D) carbon structures and can provide not only an ideal 2-D model for fundamental studies but also unique opportunities in industrial and technological applications.

This work also includes detailed studies of the effects of growth parameter variations on the structure and properties of CNS deposited, exploration of potential applications of CNS, and a semi-quantitative model for CNS growth mechanism.

1.2 Organization of dissertation

This thesis reports the synthesis and characterization of two carbon nanostructures in a planar antenna RF PECVD system. When operated in the inductively coupled mode, CNS were synthesized, whereas in the capacitively coupled mode, CNT were deposited. To investigate the structure and property of these two nanostructures, various characterization techniques were applied. Chapter 2 will briefly introduce the purposes, principles, and experimental setup of these techniques.

Chapter 3 focuses on the characteristics of the planar RF PECVD system used for nanostructure syntheses. It presents the theory and practices of a matching network of the RF system, the differences between the inductive and capacitive coupling modes of the plasma, and the procedure for switching between these two discharging modes.

Chapter 4 introduces a simple and low-cost nanosphere lithography (NSL) technique for CNT catalyst patterning. Chapter 4 also discuss the synthesis and characterization of MWNT deposited on various substrates in the capacitively coupled plasma.

Reproduced with permission of the copyright owner. Further reproduction prohibited without permission.

Chapter 5 presents experimental results of the deposition and characterization of the 2-D CNS synthesized in inductively coupled plasma, and the effects of the growth parameters on the morphology and structure of the CNS. Deposition of CNS arrays aligned parallel to a substrate surface will also be presented. Chapter 5 ends with a discussion of potential applications of CNS as field electron emission arrays and catalyst supporting material.

Chapter 6 proposes an interpretive model of growth mechanism of CNS synthesized in our RF PECVD system, based on optical emission spectrometric observations, the analysis of the electric field in the plasma, and some thermodynamic calculations. This theoretical model is also viable to account for the experimental results presented in Chapter 5.

In conclusion, Chapter 7 summarizes and reviews the overall work, while suggesting possible research for the future. CNS are novel carbon nanostructures, and there are many possibilities to be explored regarding both their synthesis and applications.

For Chapter 2 to 6, each chapter also includes its own background review and introduction to previous work, as well as a summary of that chapter.

Reproduced with permission of the copyright owner. Further reproduction prohibited without permission.

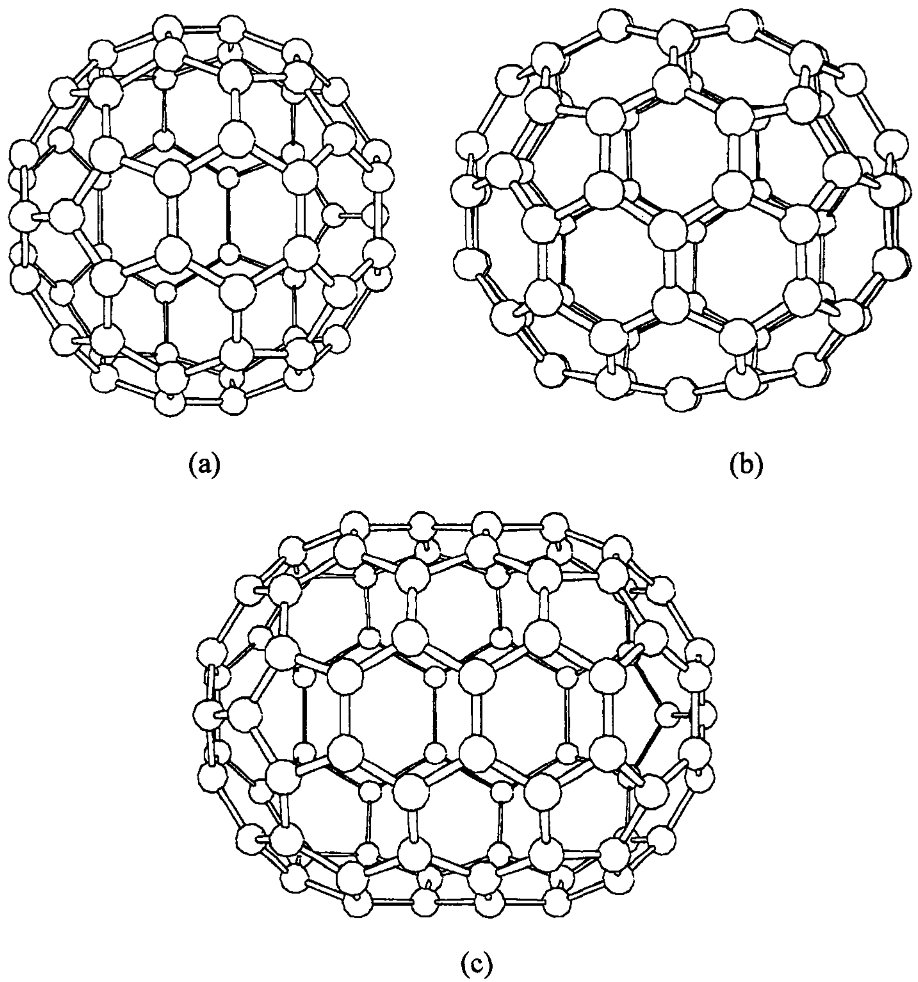

Figure 1.1: Structures of fullerene molecules: (a) C_{60}; (b) C_{70}; and (c) C_{80}. (From Dresselhaus, M. S., Dresselhaus, P. C., Saito, R, Endo, M, in *Carbon Nanotubes: Preparation and Properties*, 1997. Reprinted with permission of CRC Press, Inc.)

Reproduced with permission of the copyright owner. Further reproduction prohibited without permission.

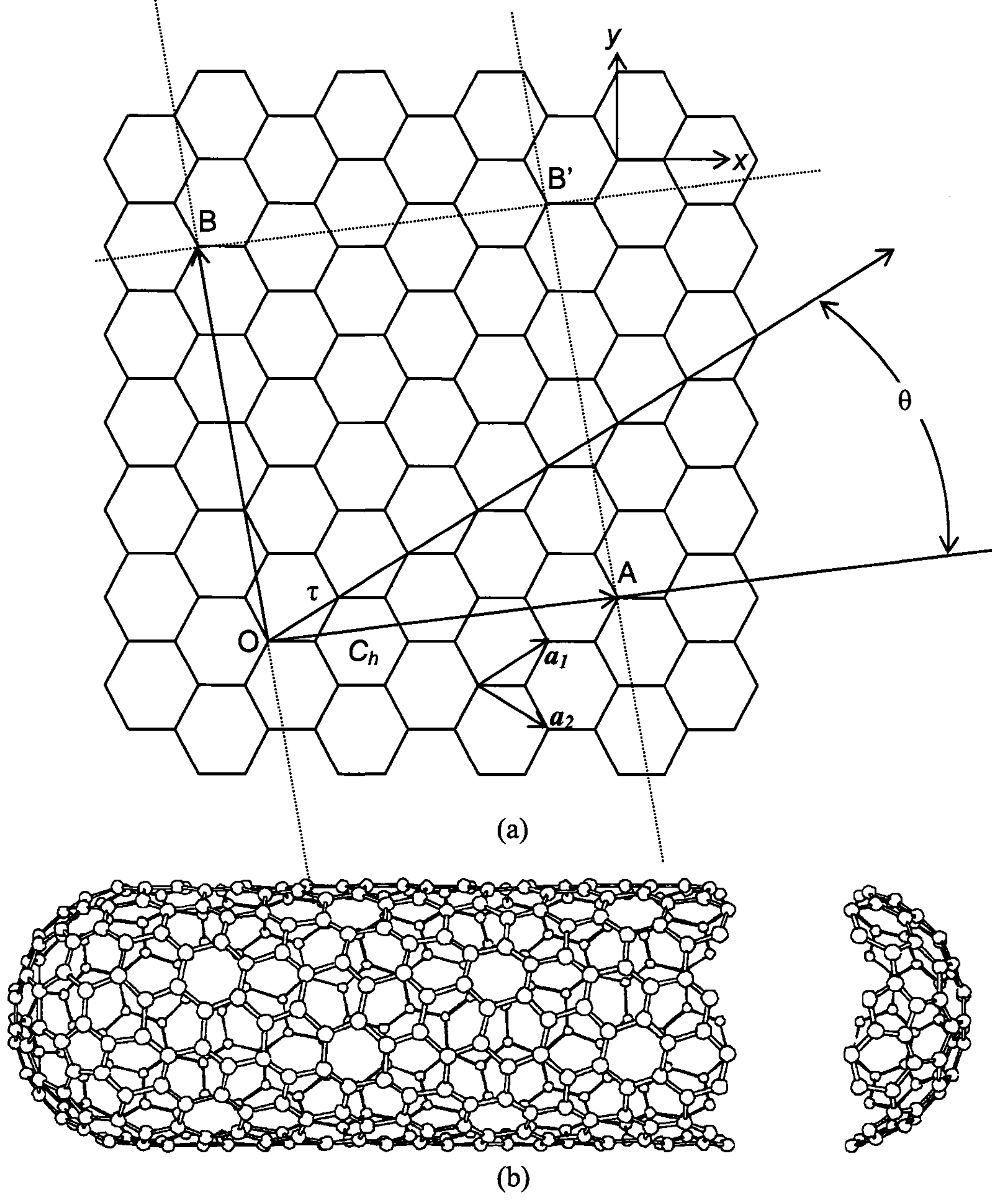

Figure 1.2: (a) A 2-D graphene sheets presenting the parameters specify a nanotube. (b) Structure of a single-walled carbon nanotube with one end detached (From Dresselhaus, M. S., Dresselhaus, P. C., Saito, R, Endo, M, in *Carbon Nanotubes: Preparation and Properties*, 1997. Reprinted with permission of CRC Press, Inc.).

Reproduced with permission of the copyright owner. Further reproduction prohibited without permission.

Table 1.1: Definition and values of carbon nanotube parameters.

Symbol	Name	Formula	Note
a_{C-C}	intersite distance		1.421Å (in graphite)
a	length of unit vector	$\sqrt{3}a_{C-C}$	2.46 Å
$\boldsymbol{a_1}, \boldsymbol{a_2}$	unit vectors	$(\frac{\sqrt{3}}{2},\frac{1}{2})a,(\frac{\sqrt{3}}{2},-\frac{1}{2})a$	in (x,y) coordinates
$\boldsymbol{C_h}$	chiral vector	$C_h = na_1 + ma_2 \equiv (n,m)$	n,m: integers
L	circumference of nanotube	$L = \lvert C_h \rvert = a\sqrt{n^2+m^2+nm}$	$0 \le \lvert m \rvert \le n$
d_t	diameter of nanotube	$d_t = \frac{L}{\pi} = \frac{\sqrt{n^2+m^2+nm}}{\pi}a$	
θ	chiral angle	$\sin\theta = \frac{\sqrt{3}m}{2\sqrt{n^2+m^2+nm}}$ $\cos\theta = \frac{2n+m}{2\sqrt{n^2+m^2+nm}}$ $\tan\theta = \frac{\sqrt{3}m}{2n+m}$	$0 \le \theta \le 30^\circ$

Reproduced with permission of the copyright owner. Further reproduction prohibited without permission.

Chapter 2

Characterization Tools for Carbon Nanostructure Material Analysis

2.1 Introduction

To investigate the morphology, structure, composition, and properties of synthesized carbon nanostructures, various techniques were applied, including scanning electron microscopy (SEM), energy dispersive X-ray spectroscopy (EDS), high-resolution transmission electron microscopy (HRTEM), selected area electron diffraction (SAD), atomic force microscopy (AFM), Raman spectroscopy, Fourier transform infra-red spectroscopy (FTIR), X-ray diffraction (XRD), Auger electron spectroscopy (AES), X-ray photoelectron spectroscopy (XPS), particle induced X-ray emission (PIXE), elastic recoil detection analysis (ERDA), field emission (FE) testing, 4-point resistivity measurement, thermal desorption spectroscopy (TDS), and Brunauer-Emmett-Teller (BET) surface area measurement. A brief description of the operating principles and

Reproduced with permission of the copyright owner. Further reproduction prohibited without permission.

instrument setup for each of the analytical techniques mentioned above will be presented in this chapter.

2.2 Scanning electron microscopy (SEM) and Energy dispersive X-ray spectroscopy (EDS)

A scanning electron microscope uses electrons rather than visible light as "light source" to form images. Scanning electron microscopy (SEM) is one of the most basic and widely used techniques in surface, thin film, and material analysis, due to its combination of high magnification, great resolution, and easy sample preparation.

The resolution of an optical microscope is limited by the wavelength of visible light sources, ranging from 380 to 780 nm. An electron microscope, however, uses high energy electrons to enhance resolution. The de Broglie wavelength of electrons (under the non-relativistic condition) is:

$$\lambda = \frac{h}{p} = \frac{h}{m_0 v} \quad \text{(Eq. 2.1)}$$

and $$E = eU = \frac{1}{2} m_0 v^2 \quad \text{(Eq. 2.2)}$$

so: $$\lambda = \frac{h}{m_0 \sqrt{2E/m_0}} = \frac{h}{\sqrt{2m_0 E}} \quad \text{(Eq. 2.3)}$$

where h is Planck's constant (6.6256×10^{-34} N·m·s), p is the momentum, m_0 is the rest mass, v is the velocity, E is the energy of the electrons, and U is the acceleration voltage. For U of 1 kV, λ equals 0.388×10^{-10} m. Visible light has a wavelength of ~500 nm, which is larger than that of electrons by a factor of 10^3-10^4. However, the resolution of an

Reproduced with permission of the copyright owner. Further reproduction prohibited without permission.

electron microscope is not yet close to the electron wavelength, due to the size and aberration of the focused electron beam, as well as other instrumental limitations.

Figure 2.1 is a schematic drawing illustrating the principle of a scanning electron microscope,[16] whereby electron beams are emitted from an electron source (thermionic, Schottky, or field emission), accelerated with high voltage (usually up to 30 kV), and focused on a specimen's surface through a series of electromagnetic lenses. When electrons interact with a specimen's surface, secondary electrons (SE), backscattered electrons (BSE), Auger electrons (AE), and X-rays can be generated (Figure 2.2). While all these signals are present, not all of them are detected or applied for imaging and information. In general, secondary electron signals are used for surface topology imaging, backscattered electron signals are used to show different elements present in a sample, and X-ray signals are used to investigate the composition of a sample. Auger electron signals are usually not detected in scanning electron microscope.

A Hitachi S-4700 field emission scanning electron microscope, shown in Figure 2.3, was used for most sample imaging in this study. At a 12 mm working distance, the S-4700 has a nominal resolution as high as 2.1 nm at 1 kV accelerating voltage, and 1.5 nm at 15 kV. The S-4700 is equipped with detectors for secondary electrons, backscattered electrons, X-ray emissions, and transmission electrons, enabling several capabilities for one instrument. It should be noted that high resolution scanning TEM (STEM) is not possible in the Hitachi S-4700 since the maximum acceleration voltage of the SEM electron gun is only 30 kV.

Another technique that is often used with electron microscopes for measuring composition information and /or imaging is energy dispersive X-ray spectroscopy (EDS).

Reproduced with permission of the copyright owner. Further reproduction prohibited without permission.

When an electron from the inner shell of an atom is ejected into a vacuum by energetic electron bombardment, the generated hole can be filled by an outer shell electron. This process can lead to the excitation of characteristic X-rays. Because different atoms have different energies of emitted X-rays, composition information can be obtained by determining the X-ray energies. However, not all transitions of electrons from an atom's outer shell to its inner shell are allowed. Instead, these transitions are determined by the quantum mechanical selection rule outlined below:

(1) $\Delta n > 0$, i. e. $L \rightarrow K$, $M \rightarrow K$, but not $L_3 \rightarrow L_2$

(2) $\Delta l = \pm 1$ and $\Delta j = -1, 0, +1$,

where n is the principal quantum number, l is the angular momentum quantum number, and $j = l \pm s$ is the total angular momentum—the combination of the orbital momentum and spin.

The S-4700 SEM has an X-ray detector (EDAX, PV7746/61 ME) of a resolution of 133 eV and is capable of analyzing light elements down to Beryllium (Be). EDS is usually operated at the maximum accelerating voltage (30 kV for S-4700), and thus it detects not only surface layers, but a certain depth through the surface, as well.

2.3 Transmission electron microscopy (TEM) and selected area electron diffraction (SAD)

Two other common electron microscopy and related techniques used in material science include transmission electron microscopy (TEM) and selected area electron diffraction (SAD). TEM utilizes a longer electron beam column than SEM, which enables a much higher acceleration voltage (up to 200 keV), and therefore a greater resolution. For

Reproduced with permission of the copyright owner. Further reproduction prohibited without permission.

example, high resolution transmission electron microscopy (HRTEM) can achieve resolution on an atomic scale.

Unlike SEM, however, in a transmission electron microscope, electrons with high energy travel through a sample and form an image on a screen or detector, as shown in Figure 2.4.[17] Because of this, the sample thickness is usually limited to 5 nm to 5μm for 100 keV electrons, depending on the density and elemental composition of the object, and the resolution desired. Special techniques, such as electropolishing, ultramicrotomy, and focused ion beam milling, are required for bulk or biological sample preparation. Fortunately, no special preparation is needed for nanostructure materials, such as carbon nanotubes and nanosheets, since they are already in nanometer scale.

Electron diffraction, or selected area electron diffraction (SAD), is another mode for TEM operation, used to characterize the crystal structure of materials. The principle of SAD is similar to that of X-ray diffraction, which will be discussed in section 2.6; the advantage of SAD is that electrons can be focused easier than x-rays, so small area detection is possible. Analytical TEM also uses two types of spectroscopy, EDS and electron energy-loss spectrometry (EELS), to obtain chemical information from electronic excitations; however the details are not presented here since they were not used in this work.

The HRTEM micrographs and SAD of carbon nanostructures in this work were produced at the University of Florida's Major Analytical Instrumentation Center (MAIC, http://maic.mse.ufl.edu/). Figure 2.5 is a picture of the instrument (Jeol JEM 2010F).

2.4 Atomic force microscopy (AFM)

Reproduced with permission of the copyright owner. Further reproduction prohibited without permission.

Atomic force microscopy (AFM) is another widely used technique for investigating surface morphology. Invented by Binnig, Quate, and Gerber[18] in 1986, AFM is one technique of scanning probe microscopy (SPM), which is based on the measurement of different forces between a sharp tip and a specimen surface. When a probe tip is raster-scanning the specimen surface, the interaction force is measured by the deflection of a soft cantilever and used for imaging. It is the short range repulsive interatomic force that enables high resolution imaging of surface. The advantages of AFM include ambient condition operation (*i.e.* no vacuum required), easy sample preparation, atomic resolution over a large area (100 μm^2), direct depth information availability, and the capability of in-situ measurement in liquid or air. However, one shortcoming is that AFM cannot directly provide chemical information or material specific properties.

AFM instruments usually including the following parts: a sharp tip mounted on a soft cantilever, a detection system for measuring the deflection of the cantilever, a piezoelectric translator to move the probe, a feedback system to keep the deflection constant and an imaging system to convert the signal into image. Figure 2.6 is a schematic view of AFM operation principle.

There are two different modes for AFM operation. If the tip is physically in contact with the sample, it is called the contacting mode. If there is no physical contact between the tip and the sample, it is called tapping mode. In tapping mode AFM, the cantilever with the tip is driven close to its resonance frequency and the topographic information is obtained from the amplitude signal of the oscillating cantilever. Since there is only intermittent contact with the sample, one can avoid scratching the sample's surface or removing loosely bounded features.

Reproduced with permission of the copyright owner. Further reproduction prohibited without permission.

The AFM used in this work is Veeco Dimension 3100 (Digital Instrument, Nanoscope IV), and is operated in air. The tip is made from SiC and has a tip apex radius as small as 5-10 nm. Figure 2.7 is a picture of the instrument.

2.5 Raman and FT-IR spectroscopy

In 1928, C. V. Raman discovered that when a beam of light traverses a transparent material, some light is scattered. Most of the scattered light maintains its original wavelength; however, a small proportion has wavelength different from that of the incident light. This phenomenon is now called Raman scattering, its presence is a result of the Raman effect, and the technique used to detect the Raman effect is called Raman spectroscopy.

Due to dramatic advances in lasers, detectors, and spectroscopic instrumentation, Raman spectroscopy has become a routinely used method for molecule and crystal structure investigation, both for industrial and research purposes. Transmission Raman spectroscopy is used mainly for chemicals in solvent, and scattering Raman spectroscopy is used for solid state materials and thin films.

According to the scattered light wavelength detection method, Raman spectroscopy is divided into Fourier Transform (FT) Raman and dispersive Raman. FT-Raman is suitable for near infra-red (IR) range to achieve better signal-to-noise ratio.

Infra-red (IR) spectroscopy is another technique used to obtain information about chemical structures by measuring the energy absorption in molecular vibrations. Both Raman and IR spectroscopy are capable of detecting the vibrations of atoms in molecules or lattices in crystal, but the origin of the vibrations is different. A vibration is IR-active if

Reproduced with permission of the copyright owner. Further reproduction prohibited without permission.

the dipole moment is changed during the vibration, and it is Raman-active if the polarizability is changed during the vibration.[19] Thus, some vibrations are Raman-active while others are IR-active. In general, vibrations are strong in Raman spectra if the bond is covalent, and strong in IR if the bond is ionic (O-H, N-H). The advantage of Raman over IR spectra is that water is a weak Raman scatter; therefore Raman spectra of samples in aqueous solutions can be obtained without strong background interference, as suffered in IR spectra. On the other hand, IR has the advantage of low sample heating, sample fluorescing, and instrumental cost. Furthermore, some rotational and rotation-vibration spectra have higher resolution in IR than in Raman. In this work, Raman is used to investigate the structural properties of carbon nanostructures.

For solid state materials, Raman scattering is inelastic light scattering by optical phonons in solids, which is a two-photon event that involves the annihilation of an incident photon and the creation of a scattered photon.[20] If the frequency of the scattered photon, ω_S, is smaller than the incident photon, ω_I, the scattering is a *Stokes* process. If ω_S is larger than ω_I, it is then an *anti-Stokes* process. Usually, only the *Stokes* Raman scattering spectra are detected in Raman spectroscopy. The frequency change of the scattered lights is determined by the phonon energy in a solid material, and different lattice structures in a solid have their characteristic phonon energies. Therefore, the position of the peaks in Raman spectra can reflect energy of the phonons, and consequently the lattice structure of the solid.

The Raman spectroscope used in this study is an inVia dispersive Raman (Renishaw, Inc.) comprised of three laser sources with four different wavelengths (488 nm and 514 nm Ar^+ ion laser, 633 nm He-Ne laser, and 785 nm diode laser), and a

Reproduced with permission of the copyright owner. Further reproduction prohibited without permission.

charge-coupled device (CCD) detector. Figure 2.8 is a picture of the spectroscope. The FTIR used in this study is Nicolet Nexus 670 spectrometer.

2.6 X-rays diffraction (XRD)

X-rays, also called Roentgen rays, were discovered in 1895 by Wilhelm Conrad Roentgen, who called them X-rays because their nature was unknown at that time. Just months after their discovery, X-rays were applied for medical detections. X-ray diffraction (XRD) was discovered by Max von Laue in 1912; and now XRD is a classical method to determine the crystalline structure of solid materials.

The X-rays used for XRD usually fall in the range of 2.5-0.5 Å. The relationship between the frequency (ν), wavelength (λ), photon energy (ε), and momentum (p) is:

$$\varepsilon = h\nu = \frac{hc}{\lambda} \qquad \text{(Eq. 2.4)}$$

and $$p = \frac{h}{\lambda} \qquad \text{(Eq. 2.5)}$$

where h is Planck's constant and c is the speed of light.

The principle of crystal diffraction is schematically indicated in Figure 2.9 (a). The diffracted X-rays have maximum intensities in the directions that satisfy Bragg's law: $2d\sin\theta = n\lambda$; where d is the lattice constant of the crystalline plane investigated, θ is the diffraction angle, λ is the X-ray wavelength, and n is an integer (1, 2, …). The phase difference of the X-rays diffracted by different lattices is $(2\pi)2d\sin\theta$. When n is an integer, the diffracted X-rays are at the same phase and consequently intensified.

Figure 2.9 (b) illustrates the classical θ-2θ geometry of XRD, where the incident angle on the sample surface is equal to that of the detector, so the crystalline planes

Reproduced with permission of the copyright owner. Further reproduction prohibited without permission.

detected are parallel to the surface of the sample. Because the sample's orientation relative to the incident beam is an important variable for single-crystal studies, the θ-2θ geometry is ideal for single-crystal surface investigation (*e.g.* epitaxial films).

In contrast to the classical θ-2θ geometry, Figure 2.9 (c) and (d) present two forms of Glancing Angle X-ray Diffraction (GAXRD). The grazing incidence angle asymmetric Bragg (GIAB, also called asymmetric) geometry is shown in Figure 2.9(c), and grazing incidence X-ray scattering (GIXS, also called symmetric) geometry is shown in Figure 2.9 (d). Both geometries are ideal for polycrystalline surface studies. The asymmetric geometry (GIAB) produces a diffraction pattern very similar to that of the identical material in bulk form detected by θ-2θ geometry, but is more surface sensitive than the θ-2θ diffraction method by about two orders of magnitude. The symmetric geometry (GIXS) is ideal for studying crystalline planes perpendicular to a sample's surface, though with greatly reduced beam intensity at the detector.

Both symmetric and asymmetric GAXRD were studied to obtain information about vertically-oriented nanosheets and their parallel base layers. The diffractometer used to evaluate our carbon nanosheets is a Philips X'ert Pro MRD system with Cu $K\alpha$ X-rays (λ=1.542 Å).

2.7 Auger electron spectroscopy (AES) and X-ray photoelectron spectroscopy (XPS)

Auger electron spectroscopy (AES) and X-ray photoelectron spectroscopy (XPS) are two of the most widely used surface analysis techniques, due to their ease of operation, the

Reproduced with permission of the copyright owner. Further reproduction prohibited without permission.

availability of commercial equipment, and their capability of providing compositional and chemical information about surface materials.

Figure 2.10 illustrates electron emissions in both AES and XPS processes. In the Auger process, the sample surface is irradiated with an electron beam, typically 2-10 keV, with sufficient energy to ionize an electron in level *X*, after which the *X* level hole is filled by an electron from level *Y* and an electron from level *Z* is ionized. This Auger transition is labeled *XYZ* (*X*, *Y*, *Z*= *K*, *L*, *M*, etc.), and the atom is double ionized. In contrast, in the XPS process, the surface is irradiated with X-rays and the entire energy is transferred to an emitted electron from level *X*. For Auger transition, the X-ray notation, such as *KLL* and *LMM*, is used, while for XPS the spectroscopy notation, such as 1*s* and $2p_{1/2}$ is used,

Both AES and XPS detect the kinetic energies of the emitted electrons due to the irradiation of electron beams and X-ray photons. The kinetic energies of Auger electrons and photoelectrons are determined by the incident beam energy and the electronic binding energies of the element according to the following equations:

$$E_{kin}(KL_1L_{23}) = E_K - E_{L_1} - E_{L_{23}} - E_{inter}(L_1L_{23}) + E_R - \Phi_S \text{ (for AES)} \quad \text{(Eq. 2.6)}$$

$$E_{kin}(h\nu) = h\nu - E_B - \Phi_S \text{ (for XPS)} \quad \text{(Eq. 2.7)}$$

where E_{kin} is the kinetic energy of the emitted electrons, E_X (*X*=*K*, *L*, *M*, etc.) is the binding energy of the electrons in the *X* level, $E_{inter}(L_1L_{23})$ is the interaction energy between the holes in level L_1 and L_{23}, E_R is the intra-atomic and extra-atomic relaxation energy, Φ_S is a small, almost constant, work function term, and E_B is the binding energy of the emitted electron.[21] Since no two elements have the same set of electronic binding energies, measurement of the emitted electron kinetic energies provides unique

Reproduced with permission of the copyright owner. Further reproduction prohibited without permission.

compositional information for each element examined. In addition, for XPS, any changes in E_B are reflected in E_{kin}, which means by monitoring changes in the kinetic energy of the photoelectrons, the changes in the chemical environment of an atom can be derived and chemical information provided.

Both AES and XPS are surface specific techniques, since emitted electrons with kinetic energy E lose part or all of their energy when they move through a solid material, as a result of inelastic collision. The average distance traveled before such a collision — the inelastic mean free path — is only 4-8 monolayers for XPS and 2-6 monolayers for AES. Consequently, only the Auger electrons and photoelectrons that originate at, or very close to the surface of solid can escape into a vacuum and be detected.

The Auger spectrometer (Perkin-Elmer PHI660, 3 keV) used in this work for elemental analyses of carbon nanosheets is part of the multifunctional surface analysis system[22] at the College of William and Mary. The X-ray photoelectron spectrometer used in this work is VG Escalab II, Mg $K\alpha$ X-rays.

2.8 Particle induced X-ray emission (PIXE) and elastic recoiled detective analysis (ERDA)

Particle induced X-ray emission (PIXE) and elastic recoiled detective analysis (ERDA) are two recently developed techniques used to analyze the elemental composition of trace metals (*e.g.* Fe, Ni) and light elements (*e.g.* H and He) respectively. Both techniques use charged particles accelerated with MeV voltage as their ion sources.

The principle of PIXE is similar to that of EDS, except that the incident beam is composed of high-energy particles, instead of electrons. In PIXE, the sample surface is

Reproduced with permission of the copyright owner. Further reproduction prohibited without permission.

irradiated with accelerated, charged particles, usually protons, and the X-rays emitted by the deexcitation (*i.e.* electrons from outer shells fall into inner shells) of the atoms in the sample are analyzed with an appropriate spectrometer. Figure 2.11 (a) is a schematic diagram of a typical PIXE instrument setup.[23] A charged particle beam is generated in an accelerator and aligned through collimators, and collide with the sample. Emitted X-rays are collected by a detector and the signal is transferred into a computer. The incident beam current is measured by a Faraday cup and current integrator.

PIXE is an ideal technique for trace metal detection, because of its high (ppm level) sensitivity. The highest sensitivity is obtained for atomic numbers $20<Z<40$ and $Z>75$, which are the most interesting regions in many analytical applications. In this work, PIXE is used to detect metal impurities in carbon nanosheet samples.

In ERDA, incident particles with energies in the MeV range irradiate the sample surface, then the recoiled atoms from the sample are analyzed to obtain both the concentration and the depth profiling information of the elements examined (as indicated in Figure 2.11 (b)). Because ERDA has approximately the same sensitivities for all target elements, it is mainly used for light element profiling, which is hardly possible by other techniques, such as AES and XPS.

Since both the scattered source particles and the recoiled atoms from the sample are simultaneously detected in ERDA experiments, the measured spectrum is usually very complicated and a computational fitting is necessary for data analysis. In this work, ERDA was used to detect the hydrogen concentration in carbon nanosheet samples, and the data fitting was carried out using SIMNRA[24] software.

Reproduced with permission of the copyright owner. Further reproduction prohibited without permission.

Both PIXE and ERDA experiments were conducted using the +30° beam line in the Microbeam End Station of Ion Beam Materials Analysis Laboratory at WR Wiley Environmental Molecular Sciences Laboratory in Richland, WA.

2.9 Four-point resistivity measurement

A four-point resistivity measurement is a quick, simple, and convenient way to measure the resistivity, conductivity, or sheet resistance of uniform thin film materials.

The 4-point probe is based on van der Pauw's theorem for measuring the resistivity of arbitrary shapes.[25] It is based on four assumptions. First, it is assumed that the probe tips are located along the circumference of the film. Second, the points of contact between the tips and the film are small in comparison to the size of the film. Third, the film is homogeneous in thickness, and fourth, no isolated holes exist in the film.

During a 4-point probe measurement, four sharp metal tips (labeled 1-4) are mechanically and electronically placed in contact with the circumference of a thin film. A current (I_{12}) is delivered through tip 1 to tip 2, and the voltage (V_{43}) between tip 4 and tip 3 is measured, as seen in Figure 2.12 (a). The van der Pauw resistance is defined as:

$$R_{12/43} = \frac{V_{43}}{I_{12}} \qquad \text{(Eq. 2.8)}$$

and similarly, if the current is delivered through tip 2 to tip 3 and the voltage between tip 1 and 4 is measured, the van der Pauw resistance is:

$$R_{23/14} = \frac{V_{14}}{I_{23}} \qquad \text{(Eq. 2.9)}$$

The resistivity (ρ) of the measured film is determined by the equation:

Reproduced with permission of the copyright owner. Further reproduction prohibited without permission.

$$\exp(\pi R_{12/43} d / \rho) + \exp(-\pi R_{23/14} d / \rho) = 1 \quad \text{(Eq. 2.10)}$$

where $R_{12/43}$ and $R_{23/14}$ are the measured van der Pauw resistances, and d is the film thickness. The solution of equation (2.10) is:

$$\rho = \frac{\pi d}{\ln 2}[(R_{12/43} + R_{23/14})/2] \cdot f(R_{12/43} / R_{23/14}) \quad \text{(Eq. 2.11)}$$

where $f(R_{12/43} / R_{23/14}) = \dfrac{-2\ln 2}{\ln a + \ln(1-a)}$ (Eq. 2.12)

and a is the solution of the following equation:

$$a^z = 1 - a \quad \text{(Eq. 2.13)}$$

in which $z = \begin{cases} x & x \le 1 \\ \dfrac{1}{x} & x > 1 \end{cases}$ (Eq. 2.14)

and $x = \left| \dfrac{R_{12/43}}{R_{23/14}} \right|$ (Eq. 2.15)

If the film thickness (d) is unknown, the sheet resistance is

$$R_{square} = \frac{\rho}{d} = \frac{\pi}{\ln 2}[(R_{12/43} + R_{23/14})/2] \cdot f(R_{12/43} / R_{23/14}) \quad \text{(Eq. 2.16)}$$

The above discussion is suitable for any arbitrary shaped films or configurations. However, for symmetric films and configurations (Figure 2.12 (b)), the calculation can be greatly simplified since

$$R_{12/43} = R_{23/14} \equiv R \quad \text{(Eq. 2.17)}$$

then $x = 1,\ z = 1,\ a = 1/2,\ f = 1$

and the resistivity is:

$$\rho = \frac{\pi d R}{\ln 2} \quad \text{(Eq. 2.18)}$$

Reproduced with permission of the copyright owner. Further reproduction prohibited without permission.

If the film thickness is unknown, the sheet resistance is

$$R_{square} = \frac{\rho}{d} = \frac{\pi R}{\ln 2} \qquad \text{(Eq. 2.19)}$$

for symmetric film shape and configurations.

In this work, the resistivity of the base layer of carbon nanosheet samples were measured using a 4-point probe (LTMP-4, MMR) as shown in Figure 2.13 (a). A standard resistance series, shown in Figure 2.13 (b), was used to calibrate the system before each measurement.

2.10 Other characterization methods for applied properties

In addition to the previously described techniques, several other characterization methods were used to study the field emission, hydrogen desorption, and specific surface area properties of carbon nanosheets. These techniques will be briefly described in the following sections.

2.10.1 Field emission (FE) measurement

Field emission (FE) is a quantum mechanical tunneling phenomena whereby the electrons in a cathode material are extracted into a vacuum by applying an external electric field. For FE testing of raw materials such as carbon nanosheets, a diode setup is typically used. For a gated device, however, a triode setup is necessary. The schematic diagrams of these two testing modes are presented in Figure 2.14.

The FE properties of different materials are judged by several parameters, including the turn-on field, maximum emission current, and emission current density. As

Reproduced with permission of the copyright owner. Further reproduction prohibited without permission.

indicated in Figure 2.14 (a), the turn-on field is defined by $E_{turn-on}=V_{turn-on}/d$, where d is the distance between the anode and the cathode, and $V_{turn-on}$ is the applied voltage when a threshold current ($I_{threshold}$) is achieved, usually at 10 nA. A sample's maximum emission current and emission current density are the highest values measured before any failure of the material occurs.

For traditional front-gated device testing, FE properties were measured using the triode setup (as shown in Figure 2.14 (b)). A cathode field ($E_{cathode}=V_C/d$) is applied to the cathode, and the voltage between the gate and the cathode is the gate voltage (V_G). The triode FE property is examined by the turn-on gate voltage V_G at a fixed cathode electric field $E_{cathode}$ when a threshold current ($I_{threshold}$) is collected at the anode. Similar to the diode measurement, the maximum current and current density are also used to determine the FE properties of carbon nanosheet devices.

2.10.2 Thermal desorption spectroscopy (TDS)

TDS was used to detect the concentration of hydrogen that was adsorbed and incorporated during the growth of carbon nanosheets. When a pristine carbon nanosheet sample was heated to an elevated temperature, the desorbed gases were analyzed by a Residue Gas Analyzer (RGA), and the mass, total amounts, and concentrations of the desorbed gases were calculated.

The results of hydrogen concentration in carbon nanosheet samples will be presented in section 5.2.4. The details of the experimental setup and calculation were reported by Zhao, X. *et al.*,[26] and therefore, are not described here.

Reproduced with permission of the copyright owner. Further reproduction prohibited without permission.

2.10.3 Brunauer-Emmett-Teller (BET) surface area measurement

The BET theory was first reported by Stephen Brunauer, Paul Hugh Emmett, and Edward Teller in 1938.[27] The BET method is widely used in surface science to calculate the surface area of solids by measuring the physical adsorption of gas molecules.

In this work, BET surface area measurements of carbon nanosheets were taken at Clear Science, Inc. The results are given in section 5.2.8.

2.11 Summary

In this work, many analysis techniques were used to investigate the morphological, structural, compositional, and applied properties of carbon nanostructures. Table 2.1 provides a brief overview of all the techniques discussed in this chapter.

This dissertation focuses on the synthesis of carbon nanostructure materials. Therefore, SEM is the most frequently used technique in the course of this work. In addition, TEM and SAD were used to study the atomic structure of the carbon nanostructures, and Raman and XRD were often applied to detect the crystalline structures and the defects in them. The remaining techniques were used to fully characterize the composition, chemical environment, surface absorption, field emission properties, and surface area of carbon nanosheets.

Reproduced with permission of the copyright owner. Further reproduction prohibited without permission.

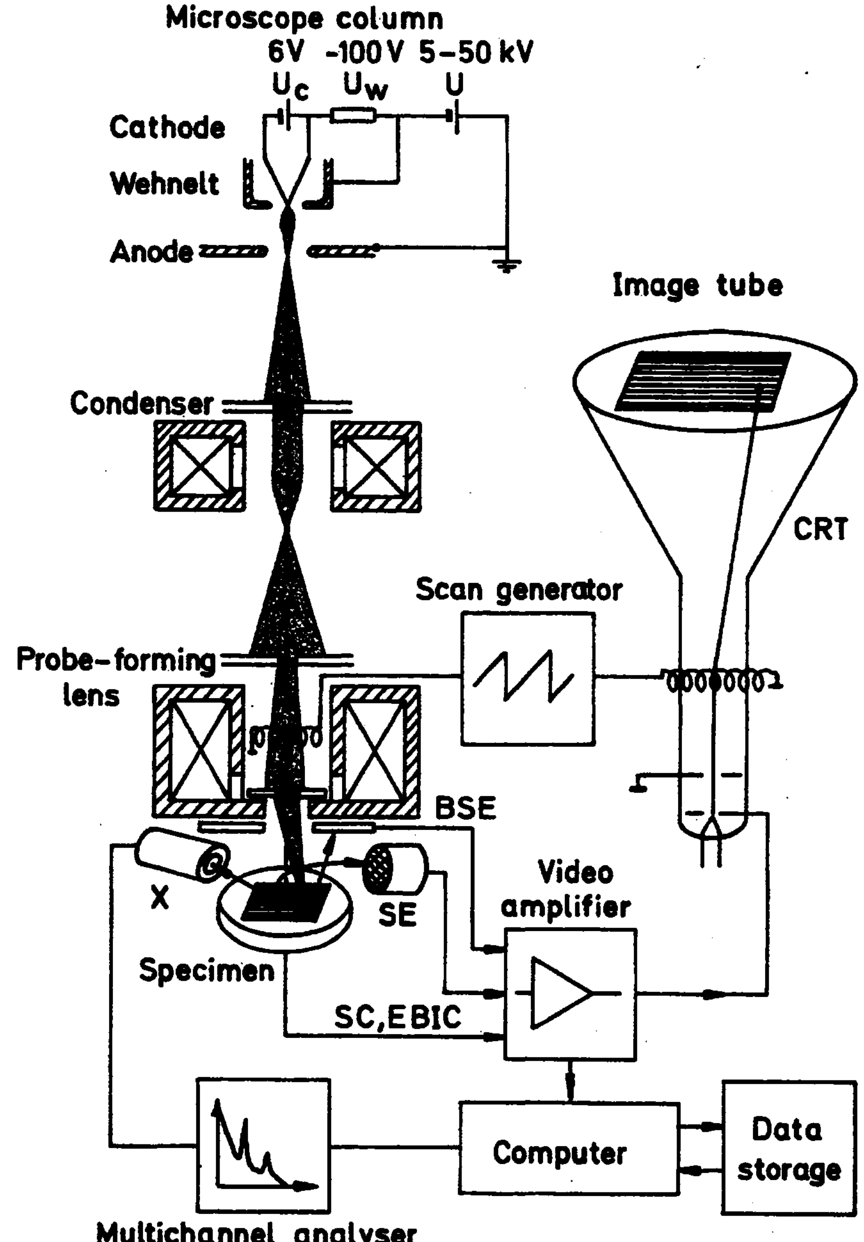

Figure 2.1: Schematic of a scanning electron microscope, illustrating the work principle. (From Reimer, L., in *Scanning Electron Microscopy: Physics of Image Formation and Microanalysis*, 1998. Reprinted with permission of Springer-Verlag.)

Reproduced with permission of the copyright owner. Further reproduction prohibited without permission.

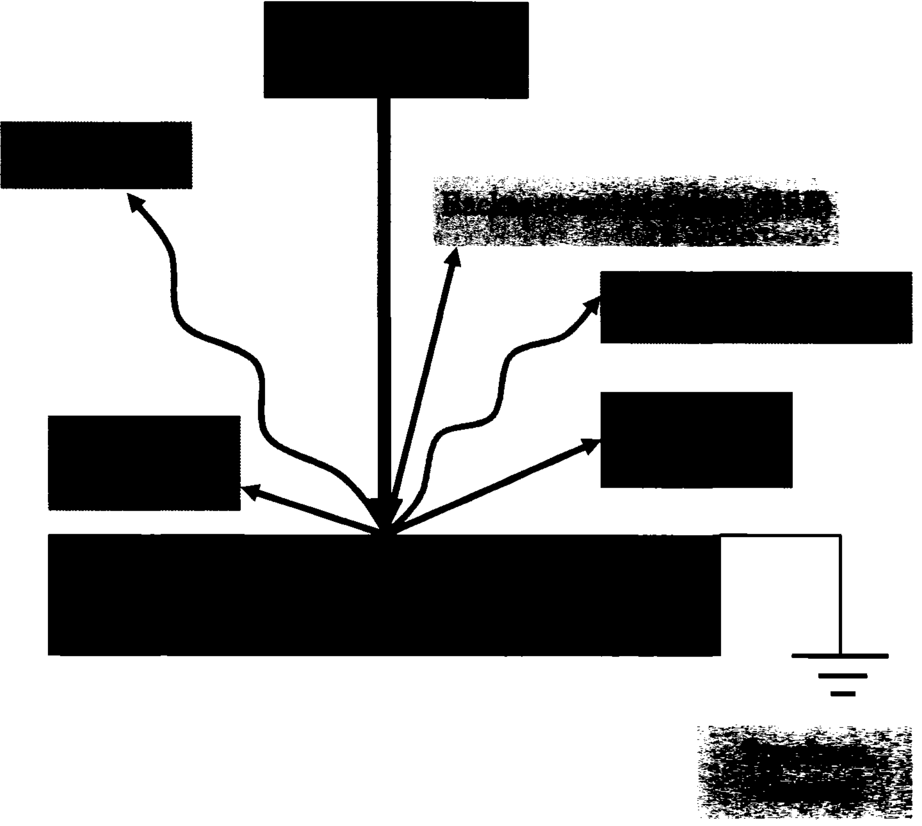

Figure 2.2: Secondary electrons (SE), backscattered electrons (BSE), Auger electrons (AE), and X-rays (X) are generated when incident electrons (IE) strike a specimen surface.

Reproduced with permission of the copyright owner. Further reproduction prohibited without permission.

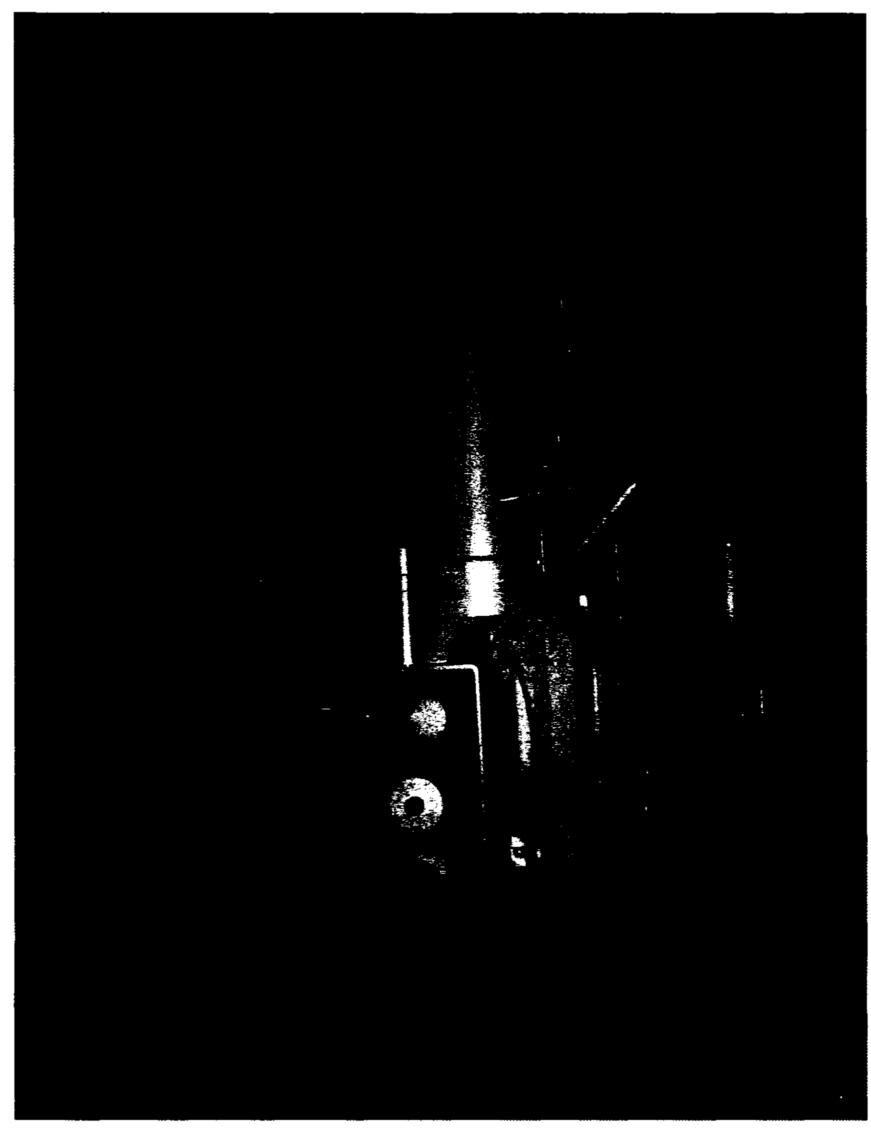

Figure 2.3: A picture of the Hitachi S-4700 FE-SEM at the College of William and Mary.

Reproduced with permission of the copyright owner. Further reproduction prohibited without permission.

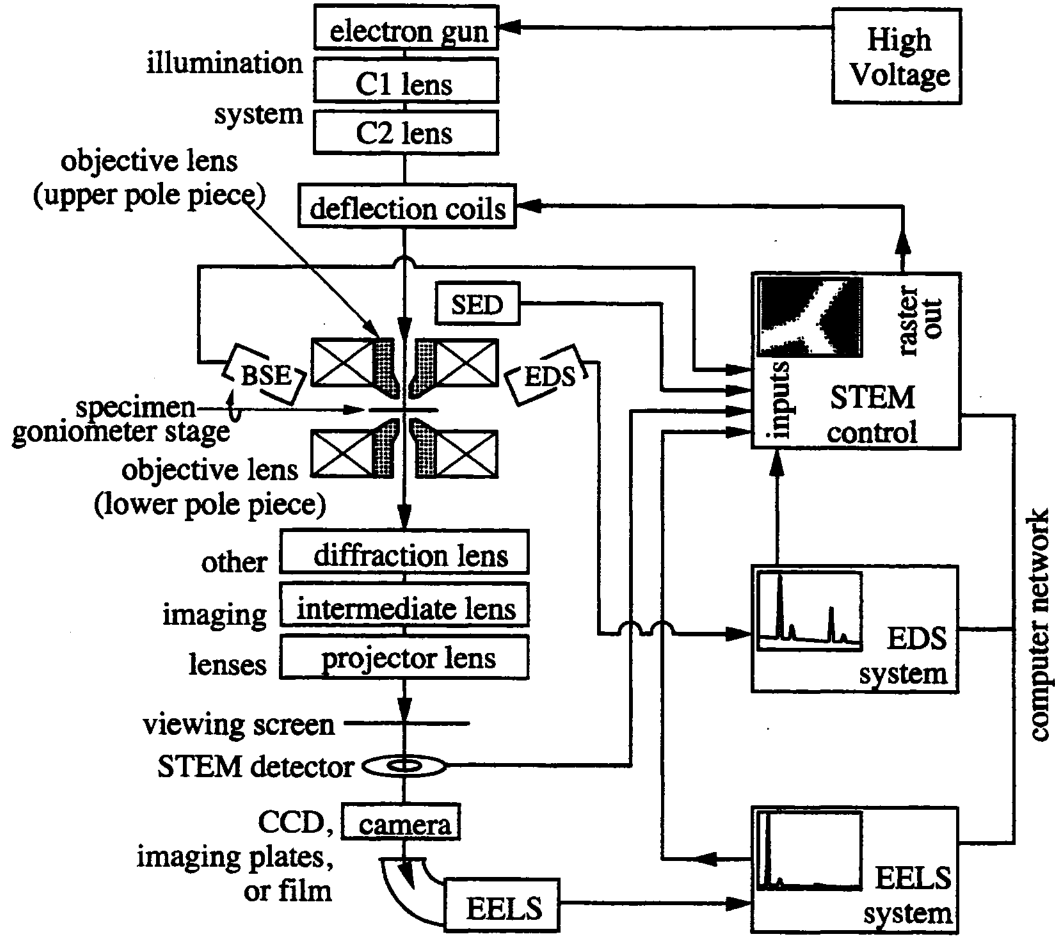

Figure 2.4: Schematic diagram of typical TEM with EDS, STEM, and EELS capability. (From Fultz, B. Howe, J. M., in *Transmission Electron Microscopy and Diffractometry of Materials*, 2002. Reprinted with permission of Springer-Verlag.)

Reproduced with permission of the copyright owner. Further reproduction prohibited without permission.

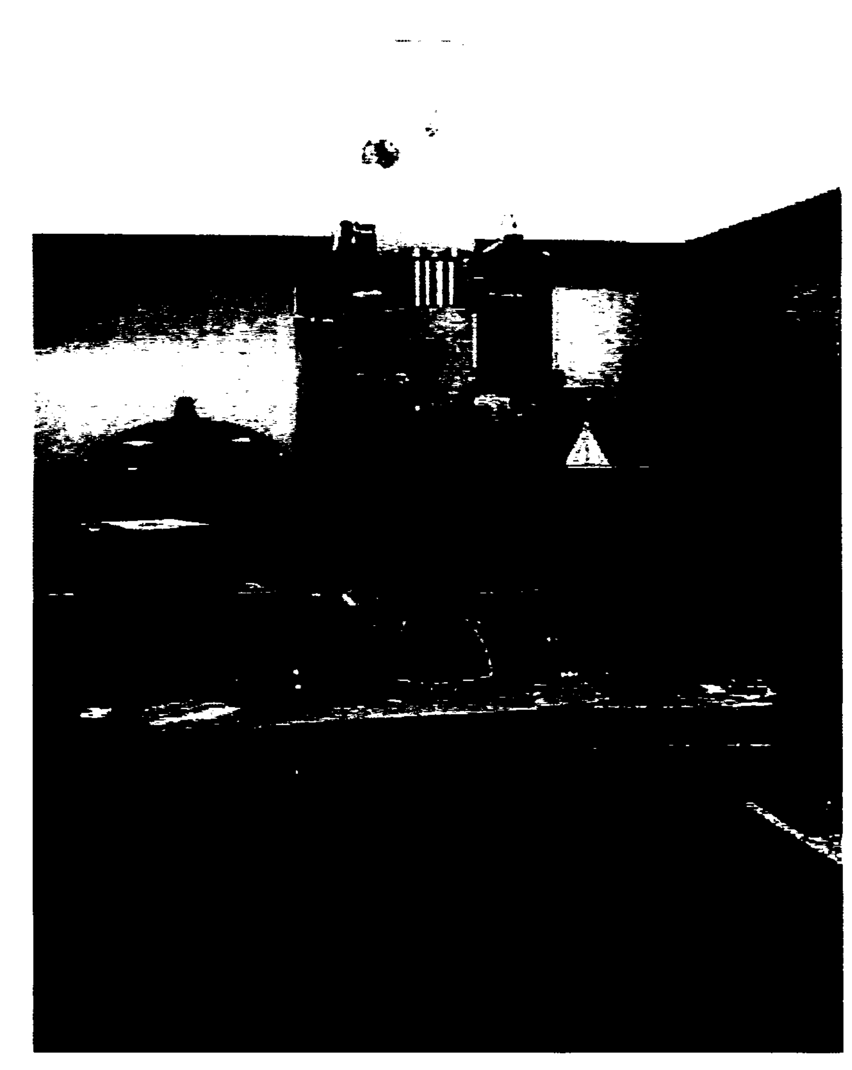

Figure 2.5: The Joel JEM HR-TEM at the University of Florida's Major Analytical Instrumentation Center (MAIC).

Reproduced with permission of the copyright owner. Further reproduction prohibited without permission.

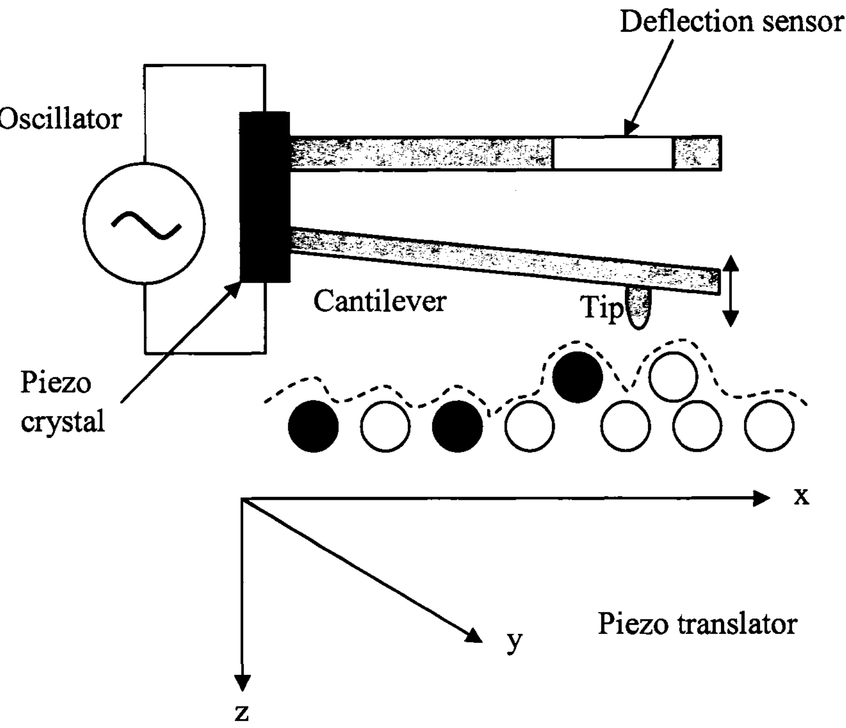

Figure 2.6: Schematic view of the principle of tapping mode AFM. The sample symbolized by the circles is scanned by means of a piezoelectric translator.

Reproduced with permission of the copyright owner. Further reproduction prohibited without permission.

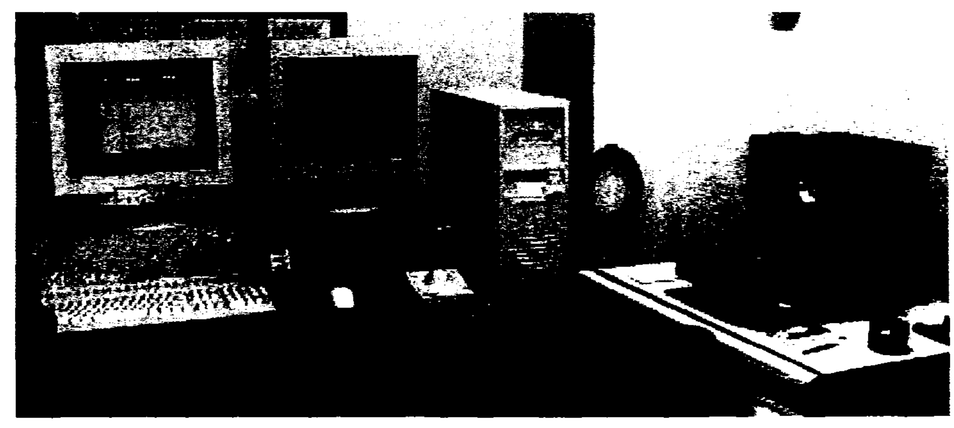

Figure 2.7: The Veeco Dimension 3100, located at the Applied Research Center, Newport News, VA.

Reproduced with permission of the copyright owner. Further reproduction prohibited without permission.

Figure 2.8: The inVia dispersive Raman spectroscope at the College of William and Mary.

Reproduced with permission of the copyright owner. Further reproduction prohibited without permission.

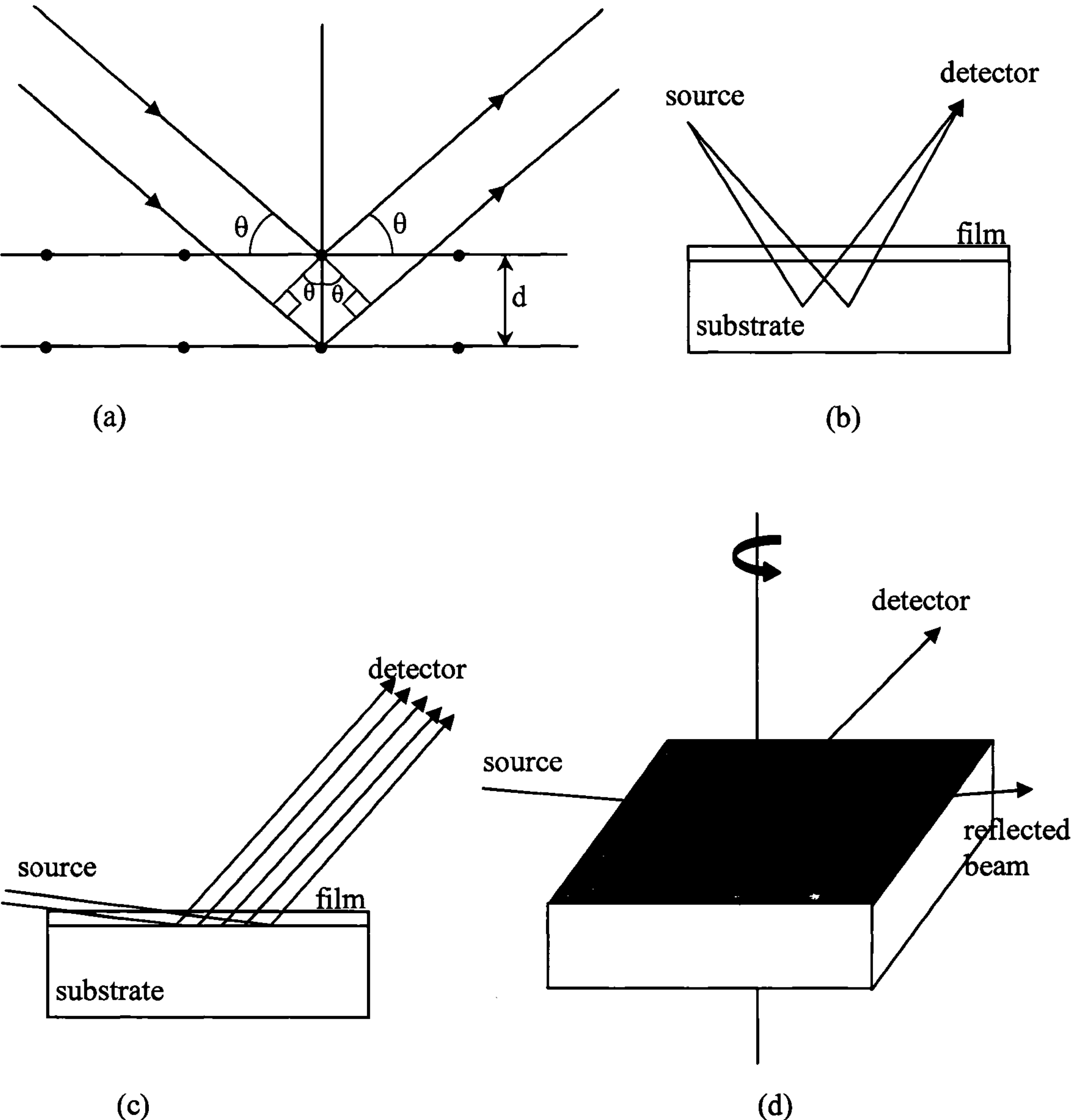

Figure 2.9: Schematics of the diffraction principle (a) and different diffraction geometries (b-d) used in crystalline structure detection. (a): The Bragg relation for the lattice constant, diffraction angle, and the X-ray wavelength. (b): θ-2θ geometry. (c): grazing incidence angle asymmetric Bragg (GIAB) geometry. (d): grazing incidence X-ray scattering (GIXS) geometry.

Reproduced with permission of the copyright owner. Further reproduction prohibited without permission.

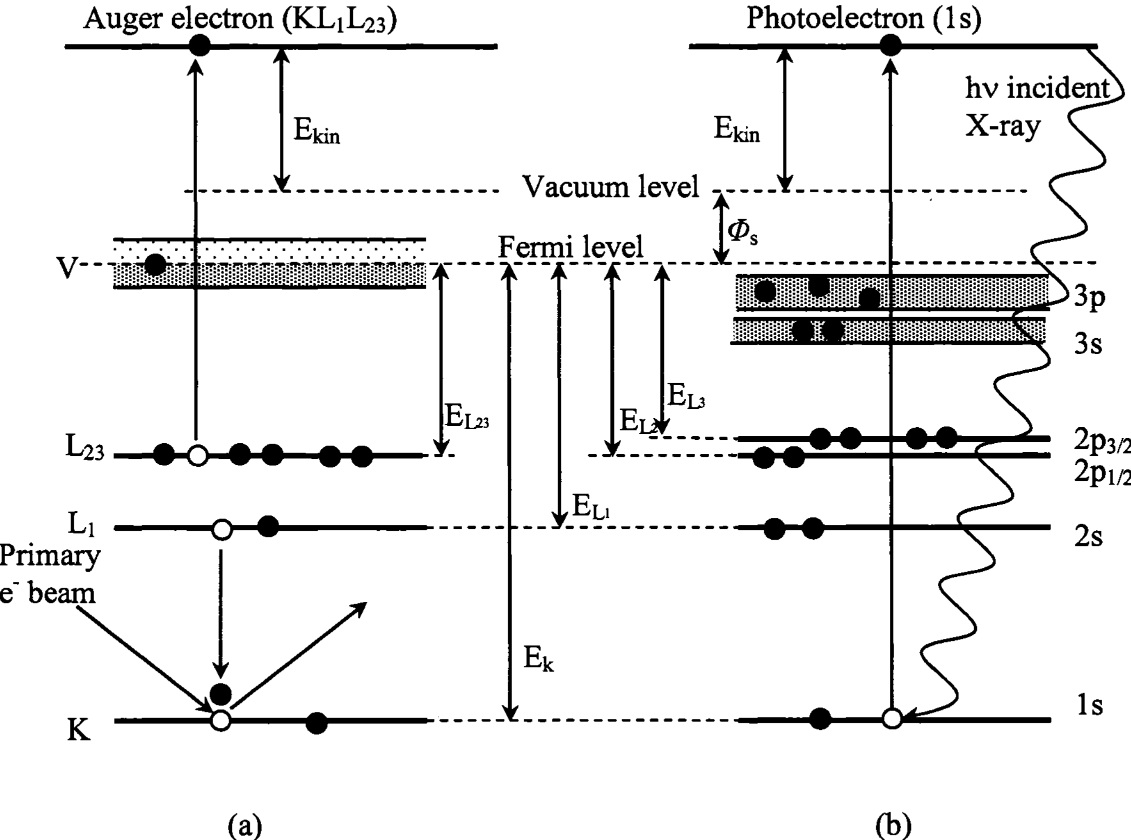

Figure 2.10: Schematic diagram of electron emission in Auger (a) and photoelectron (b) processes. Open circles indicate electrons involved in the processes.

Reproduced with permission of the copyright owner. Further reproduction prohibited without permission.

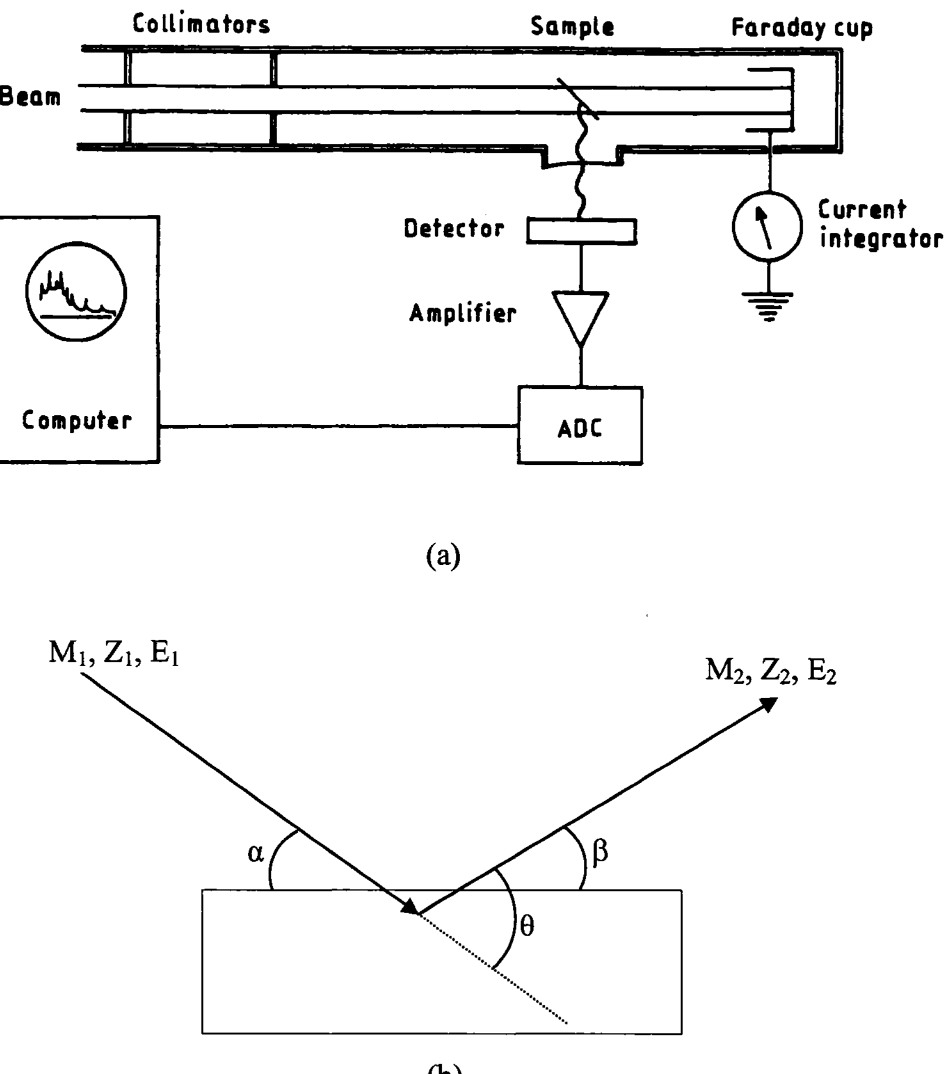

Figure 2.11: (a): Schematic diagram of PIXE setup. (From Johansson, S. A. E., in *Particle-Induced X-Ray Emission Spectrometry*, 1995. Reprinted with permission of John Wiley & Sons, Inc.) (b): ERDA geometry, M, Z, E are the mass, atomic number, and energy of a particle, subscription 1 and 2 represent incident and recoiled particles, α, β, and θ are the incident, recoil, and scattering angles, respectively.

Reproduced with permission of the copyright owner. Further reproduction prohibited without permission.

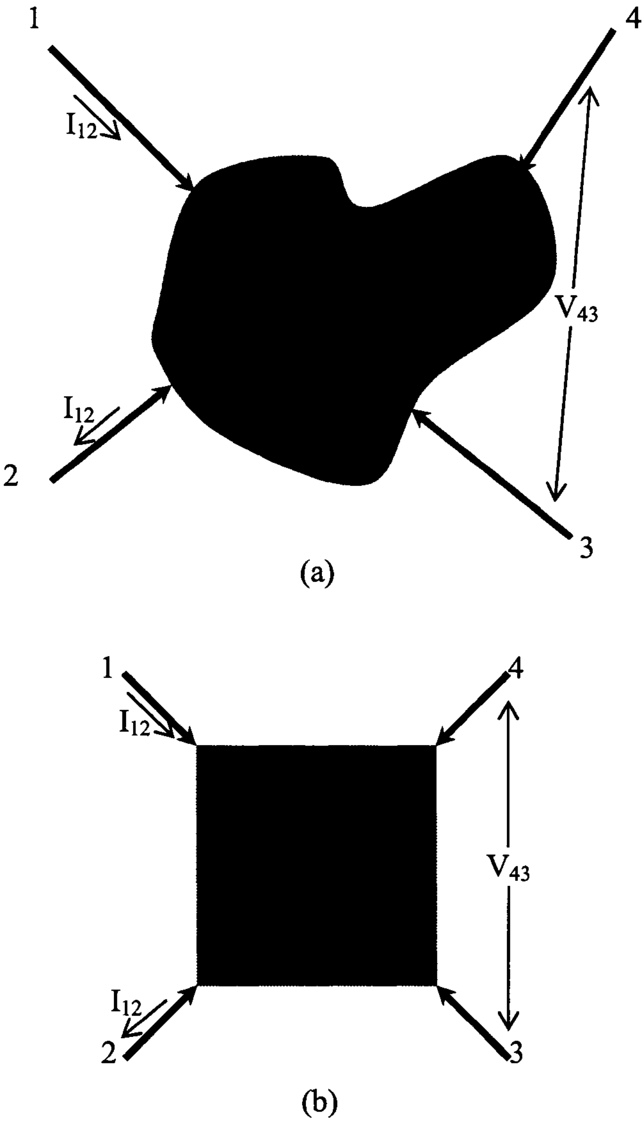

Figure 2.12: (a) Schematic diagram of a 4-point probe resistivity measurement configuration for an asymmetric film. Metal tips are placed along the sample's circumference. When a current is delivered from tip 1 to tip 2, and the voltage between tips 4 and 3 is measured. (b) An example of contact configurations for a symmetric film shape.

Reproduced with permission of the copyright owner. Further reproduction prohibited without permission.

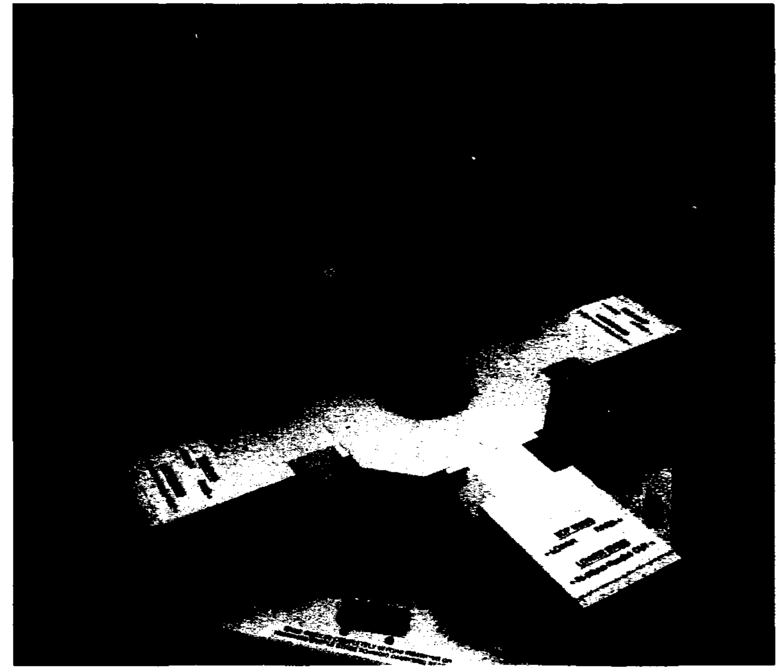

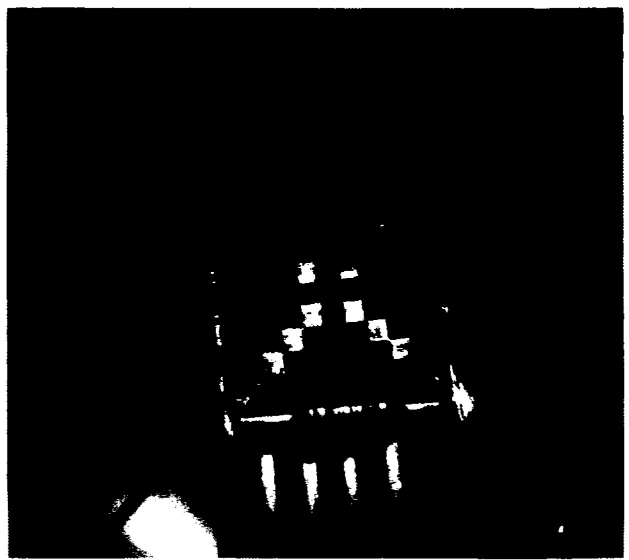

Figure 2.13: (a) Picture of the 4-point probe at ARC. (b) An enlarged photo of the 4 tips and a standard resistance for calibration.

Reproduced with permission of the copyright owner. Further reproduction prohibited without permission.

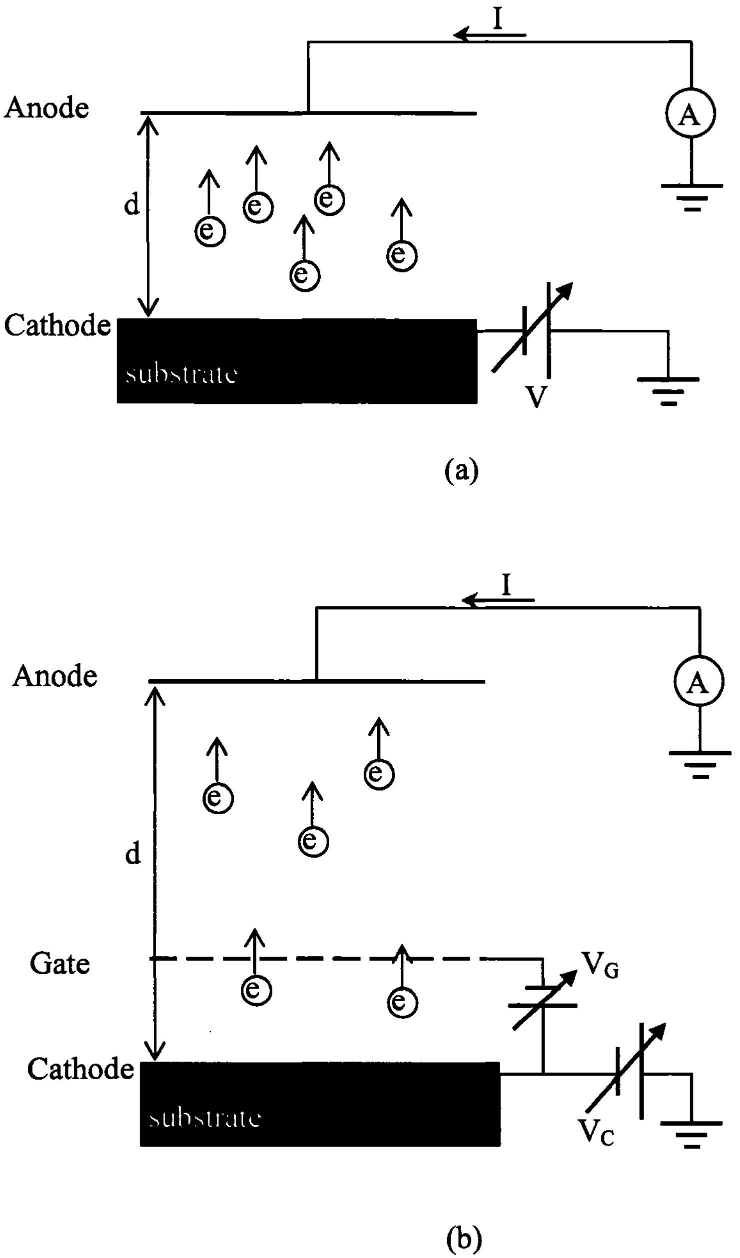

Figure 2.14: Schematic diagram of a typical (a) diode and (b) triode field emission measurement setup.

Reproduced with permission of the copyright owner. Further reproduction prohibited without permission.

Table 2.1: List of the techniques used for carbon nanostructure characterization in this work.

Instrument	Purpose	Model	Location
SEM	Surface morphology	S-4700, Hitachi	WM
EDS	Composition	PV7746, EDAX	WM
TEM	Atomic structure	JEM 2010F, Jeol	UF
SAD	Crystalline structure	JEM 2010F, Jeol	UF
AFM	Surface topology	Dimension 3100, Veeco	ARC
Raman	Lattice bonding structure	inVia, Renishaw	WM
FTIR	Chemical environment	Nicolet Nexus 670	ARC
XRD	Crystalline structure	X'ert Pro MRD, Philips	ARC
AES	Composition	PHI660, Perkin-Elmer	WM
XPS	Composition and chemical environment	VG Escalab II, Mg Kα	WM
PIXE	Trace metal composition	Ion beam lab of EMSL	PNL
ERDA	H concentration	Ion beam lab of EMSL	PNL
FE	Electron emission	Customized system	WM, ITC
4-point	Resistivity	LTMP, MMR	ARC
TDS	Absorbed gas concentration	Customized system	WM
BET	Surface area of solid	Clear Science, Inc.	Clear Science, Inc.

ARC: Applied Research Center, Newport News, Virginia
ITC: International Technology Center, Raleigh, North Carolina
PNL: Pacific Northwest National Laboratory, Richland, Washington
UF: University of Florida, Gainesville, Florida
WM: College of William and Mary, Williamsburg, Virginia

Reproduced with permission of the copyright owner. Further reproduction prohibited without permission.

Chapter 3

RF PECVD System Design and Operation Modes

3.1 Introduction

In the course of this work, we designed and constructed a radio frequency (RF) plasma enhanced chemical vapor deposition (PECVD) apparatus to synthesize carbon nanostructures. The unique planar coil antenna configuration of this RF PECVD apparatus enables two different plasma coupling modes, inductively and capacitively coupled plasma. The resulting plasma parameters, including the electron density, electron temperature, and the electric fields associated with the sheaths at the boundaries of the plasma where it contacts solid material surfaces, are strikingly different. This leads to the possibility of exploiting these different characteristics for the purpose of controlling the morphology of the deposited material. In our work, we have exploited this difference to create two different carbon nanostructures, carbon nanosheets (CNS) and carbon nanotubes (CNT). In most situations physical modification of the interior bounding

Reproduced with permission of the copyright owner. Further reproduction prohibited without permission.

surfaces are required, specifically the introduction of a Faraday shield at the coupling window to eliminate the electric fields that contribute to the maintenance of the capacitively coupled plasma.[28] In our apparatus we have been able to achieve facile switching between modes without such physical modifications, using only changes in pressure and RF input power to determine the mode of operation. This chapter will provide a brief overview of how the plasma contributes to the chemical vapor deposition (CVD) in a PECVD apparatus. We will give a description of the apparatus, emphasizing the impedance matching requirements that are needed to control the mode of operation, by control of pressure and power. The final discussion in this chapter will lay the groundwork for Chapter 4 and 5 in which we will discuss in detail the resulting film morphologies and growth modes and provide evidence that in depositing CNS we are indeed operating entirely in the inductive mode.

Chemical vapor deposition is a synthesis process in which vapor phase chemicals react near or on a heated substrate to form a solid state deposition.[29] CVD is a process suitable for the manufacture of most metals, many non-metallic elements, such as carbon and silicon, and various compounds including carbides, nitrides, and oxides. However, conventional CVD (also called thermal CVD) relies solely on thermal energy to activate the chemical reactions, and usually requires a high deposition temperature. In the 1960s, plasma enhanced CVD was developed for semiconductor applications. In PECVD, the chemical reactions are activated by plasma, thus the deposition temperature is substantially lowered.

Plasma is a collection of free charged particles that are electrically neutral on average over space. Types of plasma commonly used in CVD include direct current (DC),

Reproduced with permission of the copyright owner. Further reproduction prohibited without permission.

microwave (MW) driving electron cyclotron resonance (ECR), arc, and radio frequency (RF). Since RF PECVD is used in this work, we will limit our discussion to RF plasma. For now it is enough to note that the resulting bombardment energies and fluxes of particles that hit the solid surface at the boundaries of the plasma are different for different modes of operation; we will come back to the critical importance of these differences in later sections of this chapter.

A typical setup of RF PECVD, parallel plate capacitor configuration (also called RF diodes), is schematically shown in Figure 3.1. Two conductive plates placed in a vacuum chamber are used as electrodes, most often one is grounded and the other is powered by a radio frequency power source. The time-vary electromagnetic field between the two conductive plates generates plasma and causes the electrons and charged ions to move. Because the power is coupled to the plasma via a direct connection to an electrode in the plasma, the ion-bombarding flux and the bombarding energy cannot be controlled separately, and the voltage at the driving electrode is high. These features of RF diodes lead to a relatively narrow process window for many applications.

To overcome such limitations, low-pressure, high-density plasma sources were developed. The power source of these high density PECVD systems include microwave (MW) electron cyclotron resonance (ECR), Helicon, cylindrical and planar inductively coupled plasma (ICP),[30] as schematically shown in Figure 3.2 (a) through (d). Microwave plasma sources typically use a frequency of 2.54 GHz, while the helicon and ICP use a radio frequency of 13.56 MHz.

The power source of high density plasma discharge is usually coupled to the plasma across a dielectric window, instead of direct connection to an electrode. Thus, the

Reproduced with permission of the copyright owner. Further reproduction prohibited without permission.

substrate can be driven separately by another capacitively coupled RF or DC power, making it possible to independently control the ion flux and bombarding energy.

Carbon nanosheets and other sheet-like carbon nanostructures have been synthesized using several different CVD methods, including DC,[8] hot filament,[10] MW,[3] and capacitive RF PECVD.[31] In this study, the two-dimensional carbon nanosheets were deposited in an inductively coupled PECVD system described in the following section of this chapter.

In contrast to carbon nanosheets, one-dimensional carbon nanotubes have been synthesized by various chemical vapor deposition methods.[6] Thermal CVD, DC, microwave, hot-filament, and RF PECVD are commonly used for multi-walled CNT growth, while arc discharge and laser deposition are suitable for single-walled CNT growth. In this work, multi-walled CNT were synthesized in a capacitively coupled mode of the RF PECVD.

3.2 RF PECVD system setup

3.2.1 RF PECVD system setup

The RF PECVD apparatus for carbon nanostructure synthesis in this work is an inductively coupled discharge system shown schematically in Figure 3.3. A picture of the system is presented in Figure 3.4.

The 13.56 MHz RF power is coupled into the vacuum chamber across a dielectric quartz window 1.27 cm thick, using a 3-turn planar coil antenna, which sits on top of the quartz window inside an aluminum top-hat for radiation shielding. A matching network, consisting of two variable vacuum capacitors, is connected between the power supply and

Reproduced with permission of the copyright owner. Further reproduction prohibited without permission.

the antenna to tune the circuit. The two capacitors are located inside of an enclosed metal container—matching box. Details and principle of how the matching network works will be discussed in section 3.2.2. The shell of the matching box, the top-hat, and the vacuum chamber wall are grounded to prevent RF radiation leakage, and an RF meter is used to monitor ambient RF radiation strength whenever the RF power is turned on.

A resistive heater/sample stage is mounted in the vacuum chamber and the distance between the heater and the quartz window is adjustable (3-10 cm). The heater can reach a substrate temperature up to 1000 °C, and a K-type (Chromel-Alumel) thermocouple is placed on the upper surface of the substrate to measure the substrate temperature. The sample stage can be grounded or biased up to ± 300 V DC. To protect the rubber O-ring seal between the quartz window and the chamber when the substrate is heated, a water cooled copper adapter is added. The antenna is made from copper tubing and is also water cooled to prevent over heating.

Gases, including Ar, He, N_2, NH_3, H_2, CH_4, and C_2H_2, are introduced into the chamber through a side port, and all the gas flows are controlled and monitored by mass flow controllers and readouts. The pumping system includes a mechanical pump and a turbo molecular pump. The pressure inside the chamber is measured by a convectron gauge and baratron gauge. A background pressure of lower 10^{-6} Torr can be achieved before the gases are introduced into the chamber.

An optical emission spectrometer is connected through the cover of the top-hat through an optical fiber to collect the light emitted from the plasma discharge. A computer controls the spectrometer to collect and record the data.

Reproduced with permission of the copyright owner. Further reproduction prohibited without permission.

3.2.2 Matching network for RF PECVD

In a PECVD, the power transfer efficiency from the power source to the plasma is an important issue. In an RF PECVD system, the RF power is not efficiently transferred to the discharge if it is directly driven by the power source. The impedance of the plasma usually consists of a resistance, a capacitance, and an inductance that are determined by the boundary sheaths and by the electron density and temperature,[32] whereas the power supplies are ordinarily designed to have a coaxial line output impedance that is purely 50 Ω resistive. Thus in general the plasma impedance will be badly mismatched to the supply causing some or all of the power to be dissipated as heat within the power supply itself. Therefore, a matching network, usually consisting of capacitors and inductors, is placed between the power source and the discharge to increase the power transform efficiency.[30]

The analysis of RF matching in an inductively coupled plasma has been given before.[30] We follow that treatment closely in the next section. A capacitive plasma discharge can be considered as an impedance $Z_D = R_D + jX_D$, where R_D is the discharge resistance, and X_D is the discharge reactance. The Thevenin-equivalent circuit of the direct driven discharge is shown in Figure 3.5(a), where the power source consists of a voltage source with complex amplitude $\tilde{V}_T$ and a source resistance R_T. Then the time-average power flow into the discharge is

$$\overline{P} = \frac{1}{2}\mathrm{Re}(\tilde{V}_{rf}\tilde{I}_{rf}^{*}) \qquad \text{(Eq. 3.1)}$$

where $\tilde{V}_{rf}$ is the complex voltage across Z_D, and $\tilde{I}_{rf}$ is the complex current flow through Z_D. Solving for $\tilde{V}_{rf}$ and $\tilde{I}_{rf}$, we obtain

Reproduced with permission of the copyright owner. Further reproduction prohibited without permission.

$$\tilde{I}_{rf} = \frac{\tilde{V}_T}{R_T + R_D + jX_D} \qquad \text{(Eq. 3.2)}$$

$$\tilde{V}_{rf} = \tilde{I}_{rf}(R_D + jX_D) \qquad \text{(Eq. 3.3)}$$

Substituting (Eq. 3.2) and (Eq. 3.3) into (Eq. 3.1), we obtain

$$\overline{P} = \frac{1}{2}\left|\tilde{V}_T\right|^2 \frac{R_D}{(R_T + R_D)^2 + X_D^2} \qquad \text{(Eq. 3.4)}$$

The source voltage $\tilde{V}_T$ and resistance R_T are fixed, so the maximum power transferred to the discharge is obtained when $\partial\overline{P}/\partial X_D = 0$ and $\partial\overline{P}/\partial R_D = 0$, which gives $X_D = 0$ and $R_D = R_T$, yielding a maximum power transferred to the discharge of

$$\overline{P}_{\max} = \frac{1}{4}\frac{\left|\tilde{V}_T\right|^2}{R_T} \qquad \text{(Eq. 3.5)}$$

However, $X_D \neq 0$, and typically, $R_D << R_T$, consequently the power transferred to the discharge $\overline{P}$ is generally much less than $\overline{P}_{\max}$. To increase $\overline{P}$ to $\overline{P}_{\max}$, a matching network is placed between the source and the load. When $Z_{Load} = Z^*_{Source}$, where Z_{Load} is the load impedance and Z_{Source} is the source impedance, $\overline{P} = \overline{P}_{\max}$, and lossless matching is achieved. The role of the matching network is to equalize the total load impedance to the internal source impedance of the RF power supply.

For inductive coupling, the matching network commonly consists of two capacitors, one in series and one in parallel with the antenna,[30] as shown in Figure 3.5 (b). Based on the analysis given above, lossless matching is achieved when $Z_B = Z^*_{Source}$, where Z_B is the impedance looking to the right at the dashed line B. Similarly, the

Reproduced with permission of the copyright owner. Further reproduction prohibited without permission.

impedance looking to the right at the dashed lane A is Z_A, then the admittance Y_A, which is the inverse of Z_A, can be written as

$$\frac{1}{Z_A} \equiv Y_A \equiv G_A + jB_A = \frac{1}{R_S + j(X_1 + X_S)} \qquad \text{(Eq. 3.6)}$$

where $X_1 = -\frac{1}{\omega C_1}$. By separating the real and imaginary parts and solving for G_A and B_A, we obtain

$$G_A = \frac{R_S}{R_S^2 + (X_1 + X_S)^2} \qquad \text{(Eq. 3.7)}$$

$$B_A = -\frac{X_1 + X_S}{R_S^2 + (X_1 + X_S)^2} \qquad \text{(Eq. 3.8)}$$

The admittance Y_B, as the inverse of Z_B, is then written as

$$\frac{1}{Z_B} \equiv Y_B = Y_A + \frac{1}{jX_2} = G_A + j(B_A + \omega C_2) \qquad \text{(Eq. 3.9)}$$

where $X_2 = -\frac{1}{\omega C_2}$. For maximum power transfer, we must choose G_A to be equal to $\frac{1}{R_T}$ and C_2 to satisfy $\omega C_2 = -B_A$, so that $Z_B = R_T$ is achieved.

The RF power supply in the RF PECVD system has a source resistance of $R_T = 50\ \Omega$, and is equipped with a power meter to measure both the source RF power output and the RF power reflected by the load. The reflected power is zero when the maximum transform efficiency is achieved. In the matching network, the capacitor in series C_1 has an adjustable range of 37-320 pF, and the capacitor in parallel C_2 has an adjustable range of 50-340 pF. During a plasma discharge, these two capacitors are

Reproduced with permission of the copyright owner. Further reproduction prohibited without permission.

adjusted to achieve minimum reflected power, thus increasing the power transform efficiency and protecting the RF power supply.

3.3 Plasma coupling modes and deposition conditions

Even though the RF PECVD system in this work uses a planar coil antenna designed for inductively coupled discharge, a capacitive discharge always exists since the RF voltage underneath the antenna is often as high as 1000 V. Furthermore, if the circuit is not well-matched, or if the inductive discharge is not generated, only a capacitive discharge can be ignited. We discovered that two different carbon nanostructures, carbon nanosheets and carbon nanotubes, were synthesized in inductively and capacitively coupled plasma, respectively. This section addresses the differences between the two plasma coupling modes, as well as their relationship to each other.

3.3.1 Inductive coupling mode

Inductively coupled plasma (ICP) is one of the high-density, low-pressure plasma sources mentioned in section 3.1. Compared to a capacitive coupling mode, an inductive coupling mode usually requires a high RF power and a low pressure; however, higher plasma density is achieved due to the higher coupling efficiency of inductively coupled plasma.

During an inductively coupled plasma discharge, the planar coil antenna acts as the primary inductance and the discharging gas in the vacuum chamber acts as the secondary inductance, so that the coupling occurs through the changing RF magnetic field. In the plasma, the coupled magnetic field has mainly $\vec{z}$ and $\vec{r}$ components, so the induced electric field has mainly a $\vec{\varphi}$ component (as illustrated in Figure 3.6). This

Reproduced with permission of the copyright owner. Further reproduction prohibited without permission.

induced electric field is non-conservative, *i.e.* $\nabla \times E \neq 0$, therefore charged particles can gain time-average energy from the field without collisions. This property fundamentally distinguishes an inductively coupled plasma from a capacitively coupled plasma which has conservative, irrotational electric fields.[33]

Inductively coupled plasma was used for carbon nanosheet deposition in this work. The plasma parameters for our standard inductive discharges are 900 W RF power and 100 mTorr total gas pressure. For the parametric study of carbon nanosheet synthesis, inductive plasmas were generated using RF powers ranging from 400 W to 1200 W at a fixed 100 mTorr pressure, and with a fixed RF power of 900 W using pressures ranging from 20 mTorr to 400 mTorr.

3.3.2 Capacitive coupling mode

Recall that inductive plasma usually requires a low pressure and a high RF power. In our work, when an inductively coupled plasma could not be generated due to insufficient RF power or a non-optimized matching network, we found that a capacitively coupled plasma could be generated. Because the system's chamber wall is grounded and the RF voltage of the antenna usually exceeds 1000 V, a capacitive discharge similar to that obtained in an RF diode configuration (introduced in section 3.1) is generated. During CNT deposition in a capacitively coupled plasma, the sample stage is grounded in order to confine the plasma between the dielectric window and the sample stage.

In addition to RF power, total gas pressure is another parameter that can directly control the discharge mode. In this work, the typical pressure of capacitively coupled plasmas is ~1 Torr, while that of inductively coupled plasmas is ~100 mTorr. However,

Reproduced with permission of the copyright owner. Further reproduction prohibited without permission.

the plasma density of inductively coupled plasma is ~10 times higher than that of capacitively coupled plasma, because the ionization rate of inductively coupled plasma is ~100 times higher than capacitively coupled plasma. As a result of the high plasma density, inductively coupled plasma is much brighter than capacitively coupled plasma. Therefore, brightness is a useful indicator of the plasma discharge mode. While increasing the RF input power with all others parameters fixed, there is a sudden increasing in plasma emission associated with an abrupt transition from capacitively coupled plasma to inductively coupled plasma. Table 3.1 compares the differences of these two plasma modes.

In this chapter, we introduced the experimental setup of the RF PECVD apparatus used for carbon nanostructure synthesis, the principle of the RF matching network, and the difference of the two plasma discharge modes, inductively and capacitively coupled plasma, that create two different carbon nanostructures, carbon nanosheets and carbon nanotubes. The detailed discussion and results will be present in the following chapters.

Reproduced with permission of the copyright owner. Further reproduction prohibited without permission.

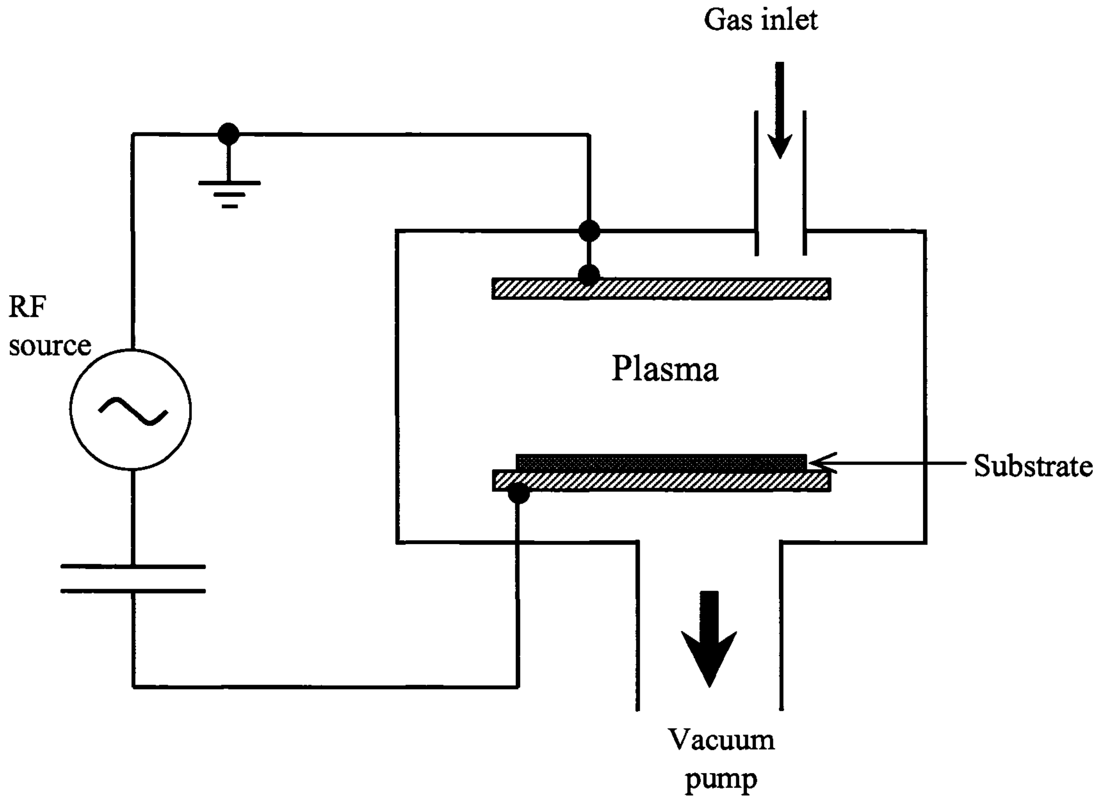

Figure 3.1: Schematic of typical parallel plate capacitor RF discharge (RF diodes) system configuration.

Reproduced with permission of the copyright owner. Further reproduction prohibited without permission.

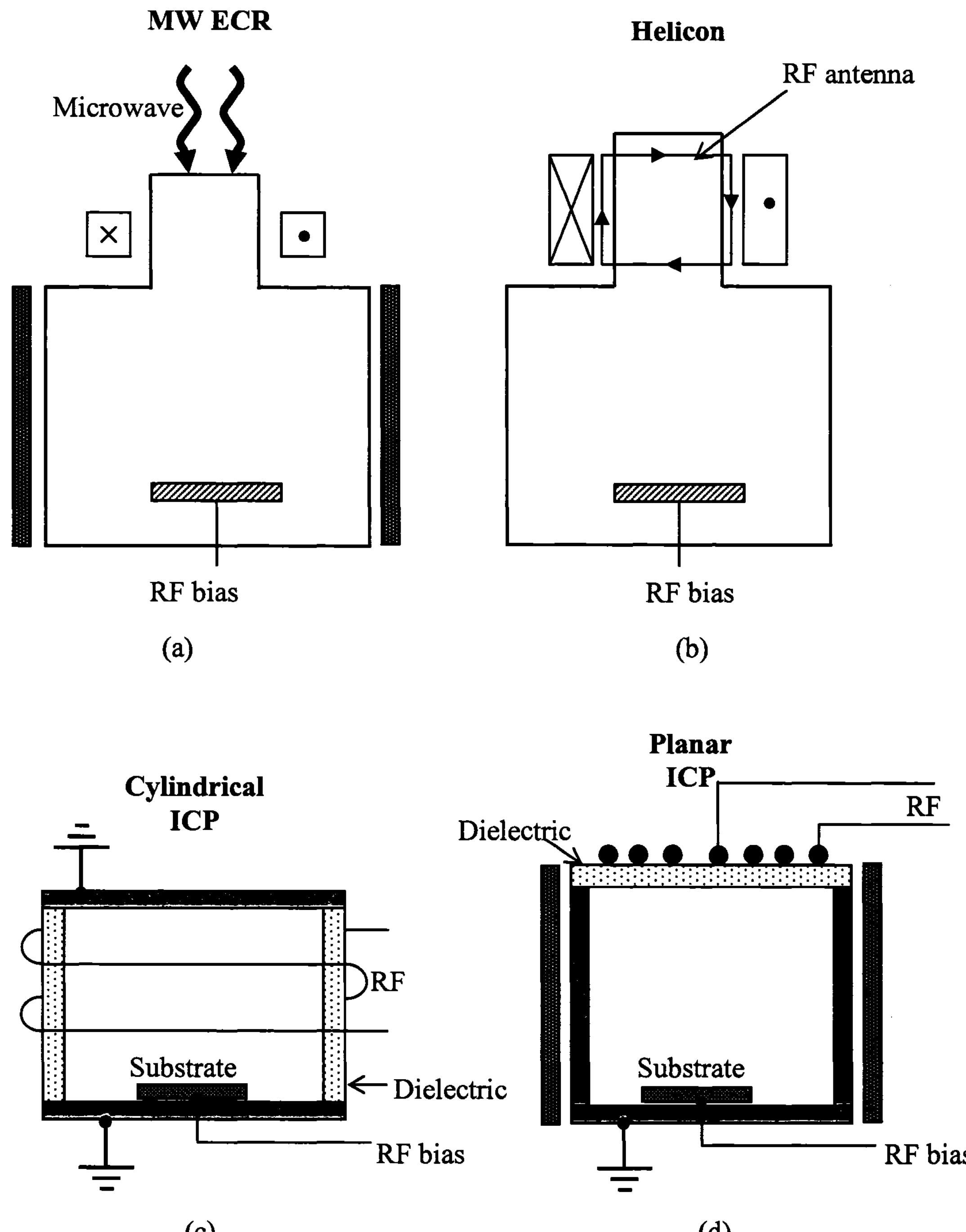

Figure 3.2 Schematics of high-density (a) Microwave driving ECR, (b) Helicon, (c) Cylindrical inductive RF, and (d) planar inductive RF plasma discharges.

Reproduced with permission of the copyright owner. Further reproduction prohibited without permission.

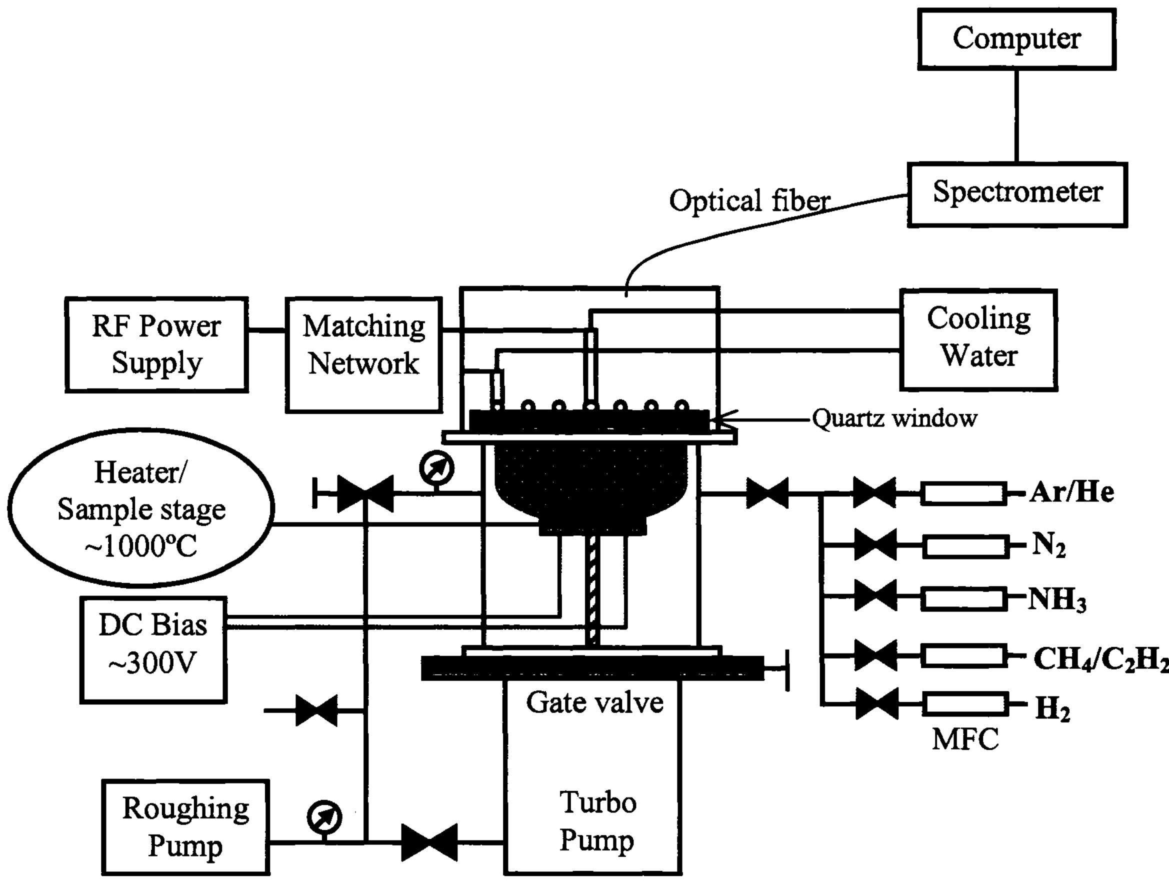

Figure 3.3 Schematic of the planar inductively coupled RF PECVD apparatus for carbon nanostructure synthesis.

Reproduced with permission of the copyright owner. Further reproduction prohibited without permission.

RF power supply
Match-box
Top-hat with antenna
Gas tanks
Mass flow controllers

Mass flow readouts
Vacuum gauge readouts
Turbo pump controller
DC bias power supply
Turbo pump
Vacuum chamber

Figure 3.4: A picture of the RF PECVD system. Some parts are labeled, others are either blocked or inside of the chamber, therefore, not visible in this picture.

Reproduced with permission of the copyright owner. Further reproduction prohibited without permission.

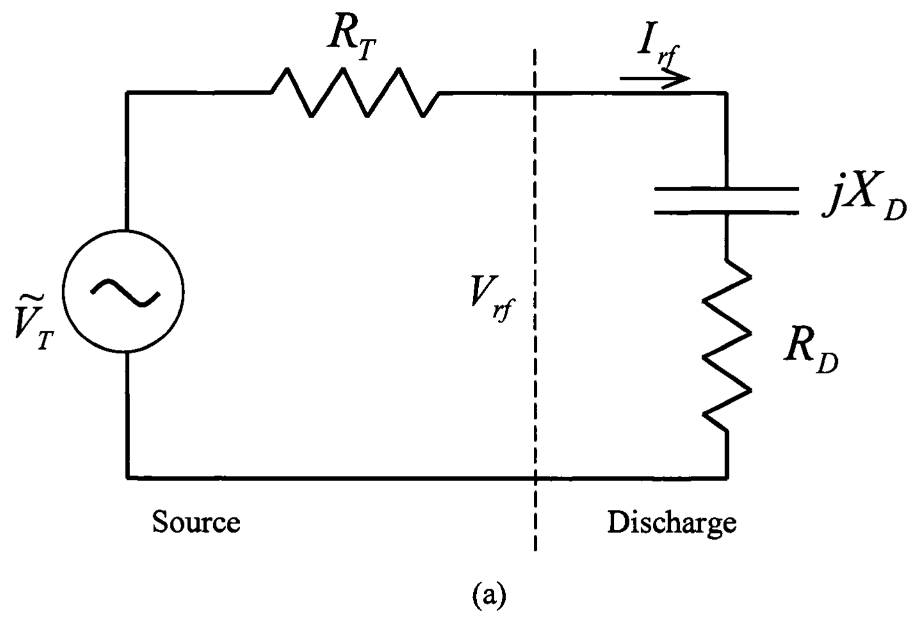

(a)

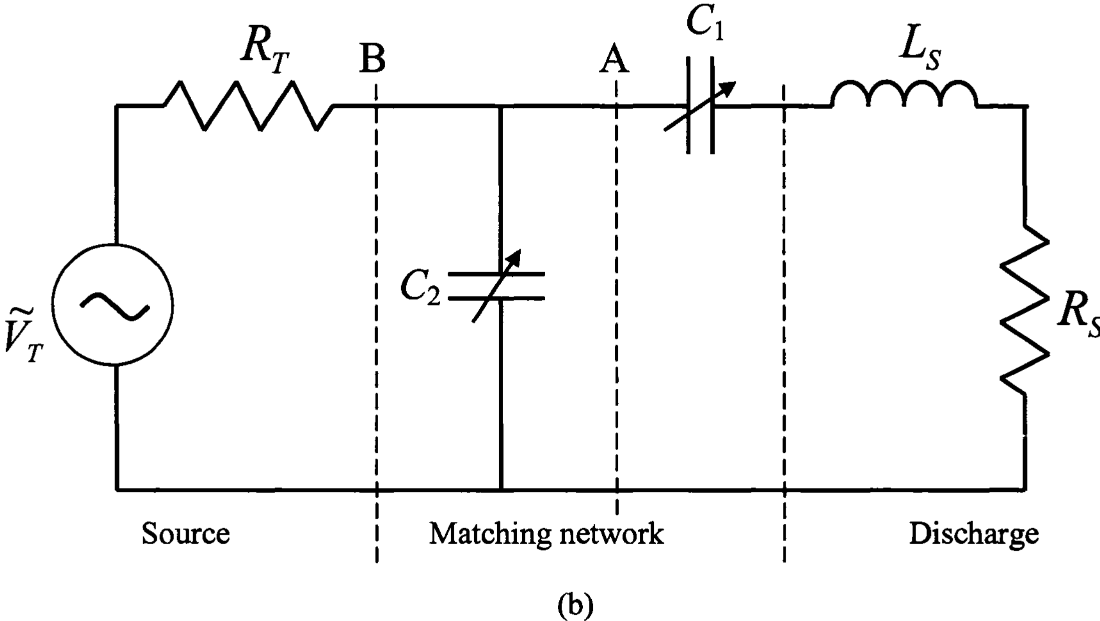

(b)

Figure 3.5: (a) Equivalent circuit of the direct connection of RF power source and the plasma discharge. (b) Equivalent circuit of a matching network placed between the RF source and the discharge.

Reproduced with permission of the copyright owner. Further reproduction prohibited without permission.

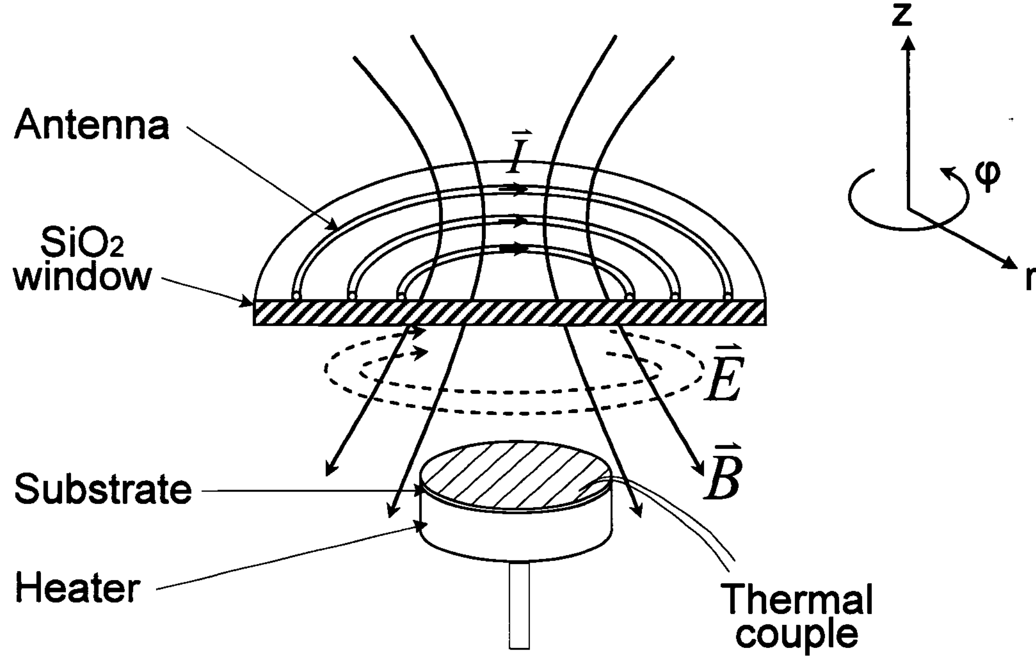

Figure 3.6: Schematic diagram of the distribution of the induced electromagnetic field in planar inductively coupled plasma in cylindrical coordinates, as shown on right.

Reproduced with permission of the copyright owner. Further reproduction prohibited without permission.

Table 3.1: Comparison of the inductively and capacitively coupled plasma used to synthesize carbon nanosheets and carbon nanotubes in this work.

Parameters	**Inductively coupled plasma**	**Capacitively coupled plasma**
Coupling force	Magnetic field	Electric field
Plasma density	High	Low
Optical emission	Bright	Dim
Typical pressure	100 mTorr	1 Torr
Power	400-1200 W	700 W
Deposition	Carbon **nanosheets**	Carbon **nanotubes**

Reproduced with permission of the copyright owner. Further reproduction prohibited without permission.

Chapter 4

CNT Deposition and Properties

4.1 Introduction of CNT synthesis

In the course of this work, two carbon nanostructures, carbon nanotubes (CNT) and carbon nanosheets (CNS), were synthesized and characterized. This chapter presents the deposition and properties of the CNT deposited by the radio frequency (RF) plasma enhanced chemical vapor deposition (PECVD) system introduced in Chapter 3, as well as a catalyst patterning technique, nanosphere lithography (NSL), used in preparing the substrates for CNT growth.

The synthesis of carbon nanotubes can be traced back to the 1970's and 1980's when carbon filaments less than 10 nm in diameter were prepared by hydrocarbon decomposition at high temperatures in the presence of transition metal particles less than 10 nm in diameter.[6] However, the carbon nanotube field was not seriously launched until the observation of the atomic structure of carbon nanotubes in 1991 by Iijima using high resolution transmission electron microscopy (HRTEM).[7]

Reproduced with permission of the copyright owner. Further reproduction prohibited without permission.

Various synthesis routes of both single-walled and multi-walled CNT have been developed, including arc discharge, laser ablation, and chemical vapor deposition (CVD) methods.[6] Single-walled CNT (SWNT), as well as ropes consisting of tens of individual SWNT close-packed via *van der Walls* interaction, have been prepared by arc discharge and laser ablation using a carbon target containing a small amount of transition metal catalyst. The temperatures involved in these two methods were high, 3000-4000 °C, close to the melting point of graphite. Typical by-products of SWNT production using arc discharge and laser ablation include fullerenes, amorphous carbon, and graphitic polyhedrons with enclosed metal particles. Therefore, a purification process involving refluxing as-grown SWNT in a nitric acid solution has been developed and is widely used to purify CNT.[34]

Multi-walled CNT (MWNT) have also been obtained by arc discharge when growth conditions such as gas pressure and the arcing current were controlled.[6] MWNT prepared by arc discharge are straight and have a high crystallinity. However, the temperature required for arc discharge is high; and a purification process is needed to remove the by-products.

Another method for preparing MWNT, chemical vapor deposition (CVD), has been successful in synthesizing carbon nanotubes, fibers, and filament materials for 15-25 years. The temperature involved in CVD is 550-750 °C, much lower than that for arc discharge. The crystallinity of CNT prepared by CVD, however, is low compared to CNT prepared by arc discharge and laser ablation, because of the low temperatures involved in CVD. On the other hand, the advantage of the CVD method is that controlled growth of aligned and ordered nanotube structures can be achieved.

Reproduced with permission of the copyright owner. Further reproduction prohibited without permission.

The CVD nanotube growth process involves the dissociation of hydrocarbon molecules, and the dissolution and saturation of carbon atoms in metal nanoparticles. Tubular carbon in sp^2 structure forms when carbon atoms precipitate from the metal nanoparticles. Therefore, transition metal nanoparticles are generally required as active catalysts for CVD nanotube growth.

In this chapter, we will present the results of MWNT produced in an RF PECVD system on substrates patterned with catalyst nanoparticles using a nanosphere lithography (NSL) technique.

4.2 Nanosphere lithography for catalyst patterning

4.2.1 Introduction

As mentioned in the previous section, a catalyst is necessary for carbon nanotube growth using the CVD method. The size and distribution of the catalyst is an important factor in determining the structure of the CNT. Typical catalysts for CNT growth are transition metals, such as Fe, Co, and Ni. Instead of continuous films, isolated islands of catalyst materials are used for CNT growth. The diameter of the CNT is determined by the size of the catalyst particles; therefore controlling the size and uniformity of catalyst particles is the key to creating CNT with desired diameters.

Different methods are used for catalyst patterning, including plasma etching, photolithography, electron-beam (e-beam) lithography, and ion-beam lithography. Each method has its limitations. While the plasma etching method cannot produce ordered arrays with uniform particle size, photolithography cannot pattern a sufficiently small catalyst, and the e-beam and ion-beam lithography methods are too slow and expensive,

Reproduced with permission of the copyright owner. Further reproduction prohibited without permission.

especially for a large scale process. In response to these issues, we used a simple, low cost, and large scale catalyst patterning method—nanosphere lithography (NSL)—in this work.

The nanosphere lithography technique was first developed by Deckman in the 1980's.[35-37] In 2003, Huang *et al.*,[38] used NSL to prepare catalyst patterns for carbon nanotube growth. Our group reported the use of NSL for catalyst patterning in carbon nanostructure synthesis in 2004.[39] The following sections will introduce the principles of NSL, and the catalyst patterns developed by NSL.

4.2.2 Single-layer and double-layer NSL

The process of NSL is illustrated in Figure 4.1. The NSL starts with spin-coating nanospheres (in a solution) on a substrate, followed by the evaporation of a catalyst metal thin film and the removal of the nanospheres in a solvent with the aid of ultrasonication.[39] The areas covered by nanospheres have no metal deposition after the removal of nanospheres; only the holes between the nanospheres that are exposed during metal evaporation have metal depositions on the substrate.

The spin-coated nanospheres may form single-, double-, or more-layered structures, depending on the spin-coating parameters and the surface activities of the nanospheres. If a single-layer nanosphere is formed, the patterned catalyst islands are triangular-shaped and form a hexagonal array, as illustrated in Figure 4.2. If the diameter of the nanospheres equals D, the distance between the adjacent holes is

$$d_{SL} = \frac{D}{\sqrt{3}} = 0.577D \qquad \text{(Eq. 4.1)}$$

Reproduced with permission of the copyright owner. Further reproduction prohibited without permission.

and the area of the holes between the nanospheres is

$$A_{SL} = \frac{1}{2} \cdot D \cdot \frac{\sqrt{3}}{2} D - 3 \cdot \frac{1}{6} \cdot \frac{1}{4} \pi D^2 \approx 0.04 D^2 \qquad \text{(Eq. 4.2)}$$

When the substrate temperature is increased, the triangular islands coalesce into round dots. Assuming the dots have the same area as the triangular islands, the equivalent diameter of the holes is approximately

$$\phi_{SL} = \sqrt{\frac{4}{\pi} A_{SL}} \approx 0.23D \qquad \text{(Eq. 4.3)}$$

This calculation indicates that the size of the patterned dots is only 23% the size of the nanosphere used as masks. Furthermore, the dots are well separated, with a distance between them about 2.5 times greater than the size of the dots.

If a double-layered nanosphere structure forms, the nanospheres in the second layer cover half the holes in the first layer and reduce the size of the other half holes. The patterned islands are hexagonal-shaped, and form a triangular array, as illustrated in Figure 4.3, where the nanospheres of the second layer are gray. The distance between the adjacent holes for double-layer NSL is

$$d_{DL} = D \qquad \text{(Eq. 4.4)}$$

and the area of the dots is approximately

$$A_{DL} \approx 6 \cdot \frac{1}{2} \cdot [(\frac{2}{\sqrt{3}} - 1)\frac{D}{2}] \cdot [\frac{2}{\sqrt{3}}(\frac{2}{\sqrt{3}} - 1)\frac{D}{2}] \approx 0.02 D^2 \qquad \text{(Eq. 4.5)}$$

Therefore, the equivalent diameter of the round dots is

$$\phi_{DL} = \sqrt{\frac{4}{\pi} A_{DL}} \approx 0.16D \qquad \text{(Eq. 4.6)}$$

Reproduced with permission of the copyright owner. Further reproduction prohibited without permission.

Equation 4.6 indicates that for a double-layered NSL, the size of patterned dots is ~16% the size of the nanospheres used as masks, and the distance between the dots is about 6 times the size of the dots.

Table 4.1 lists the theoretical values of the sizes and distances between the dots patterned by single-layer and double-layer nanosphere lithography, using nanospheres with various diameters. Since the geometry of the coalesced dots resembles a hemisphere rather than a column with a height the same as the thickness of metal thin films, the actual dot size should be less than the calculated values. It is possible that three or more layers of nanospheres are formed on a substrate surface during the spin coating. In this case, there is no metal deposition on the substrate, and no catalyst pattern can be found after removal of the nanospheres.

The number of layers of nanosphere coating depends on the concentration of the solution, the spinning speed, and the diameter and surface activity of the spheres used. For better surface coverage, the nanosphere coating is usually applied in two stages. The first low speed spinning stage improves the coverage of the substrate surface, and the second high speed spinning stage reduces the number of nanosphere layers formed.

4.2.3 NSL for carbon nanotube catalyst patterning

For the catalyst patterning of carbon nanotube deposition in this work, we used self-assembled polystyrene nanospheres (Interfacial Dynamics Corporation) with a diameter of 419 nm, and silica spheres with a diameter of 400 nm, as masks for nickel (Ni) catalyst patterning. The nanospheres arrived from the manufacture as a suspension in water. A

Reproduced with permission of the copyright owner. Further reproduction prohibited without permission.

mixture of surfactant Triton X-100/methanol (1:400 by volume) was used to further dilute the suspension by a factor of 1.5.

In our work, both uncoated silicon (Si) wafers, and Si wafers coated with 365 nm of silicon dioxide (SiO_2) were used as substrates. The nanosphere solution was coated on the substrates by a spin coater (Chemat Technology KW-4A) at ~500 rpm for the first stage and ~1000 rpm for the second stage. Figure 4.4 shows top-view (a) and side-view (b) AFM images of the spin-coated 419 nm nanospheres. The self-assembled nanospheres form a periodic array, with each sphere surrounded by 6 other spheres, as expected. The side-view image shows the topology of the nanosphere layers.

After the nanosphere coating, the substrates were coated with 10-30 nm Nickel films by electron-beam evaporation (Lebow, Co.). After the Ni deposition, the nanospheres, together with the Ni coated on top of them, were removed from the substrate by solving them in CH_2Cl_2 for 5 minutes with the aid of ultrasonication. Because AFM only detects surface morphologies, AFM observations could not determine the number of layers of nanospheres coated on the substrate. However, this number could be determined by observing the pattern of Ni islands on the substrates after removing the nanospheres. Figure 4.5 shows both single-layer (hexagonal) and double-layer (triangular) patterns of Ni islands. In the single-layer pattern (Figure 4.5(a)), the Ni islands are triangular, and the distance between adjacent islands is about 250 nm. This distance is consistent with the theoretical value calculated in Equation 4.1. In the double-layered pattern (Figure 4.5(b)), the Ni islands are not ideally hexagons, because the centers of the second layer spheres were not located at the exact center of the holes in the first layer.

Reproduced with permission of the copyright owner. Further reproduction prohibited without permission.

The distance between the adjacent islands, however, is about 420 nm, which matches the theoretical value of Equation 4.4.

After removing the nanospheres, the substrates with Ni catalyst patterns were rinsed in de-ionized water, blown dry, and prepared for CNT deposition. Usually, the substrates were heated and etched in an inductive plasma before beginning CNT growth, in order to optimize the catalyst size. Figure 4.6 shows the AFM image of heated and etched Ni catalyst patterns by single-layer (a) and double-layer (b) nanosphere lithography. As expected, these images revealed that the catalyst islands coalesced to round dots after the heating and etching procedure.

4.3 Deposition and characterization of CNT

In this work, all carbon nanotubes were synthesized on catalyst patterned substrates in an RF PECVD system using a capacitively coupled plasma. The substrates were pre-etched in an inductive plasma of NH_3 (8 sccm, ~12 Pa, 900 W RF power) for 5-15 minutes to optimize the catalyst size. The sample stage was grounded during the deposition to confine the capacitive plasma between the sample stage and the quartz window. These factors remained constant.

4.3.1 Structure and properties of typical CNT

We have deposited one-dimensional carbon nanotubes or nanofibers with various conditions.[33] Typical parameters for carbon nanotube deposition include a substrate temperature of ~700 °C, a total gas pressure of ~1 Torr, an input RF power of 700 W, a deposition duration of 20 minutes, and feedstock gases of 20% C_2H_2 (15 standard cubic

Reproduced with permission of the copyright owner. Further reproduction prohibited without permission.

centimeter per minute (sccm)) in NH_3 (60 sccm) atmosphere. This section will discuss the structure and properties of typical CNT.

SEM images of typical CNT are shown in Figure 4.7. Low magnification in Figure 4.7 (a) shows randomly oriented, "spaghetti-like" C_2H_2/NH_3 carbon nanotubes, typically 20-50 nm in diameter, and several microns in length. Figure 4.7 (b) shows the hexagonal Ni catalyst pattern at the root of each nanotube, indicating that typical nanotubes formed via a base growth mechanism. Figure 4.7 (c) is a higher magnification image of one Ni catalyst island. The hollow center of a nanotube can be seen in this image. The HRTEM image shown in Figure 4.8, in which parallel fringes were observed, indicates that typical carbon nanotubes consist of rolled graphene layers with a hollow center. The layers are parallel to the tube axis, and truly are multi-walled nanotubes, not bamboo-like carbon nanofibers.

Raman spectrum (514 nm excitation laser wavelength) from a typical nanotube sample is presented in Figure 4.9. First order peaks are labeled as *D* at 1360 cm^{-1}, and *G* at 1590 cm^{-1}, which originate from defective carbon and graphitic carbon, respectively. These defects may include vacancies and strained hexagonal/non-hexagonal (pentagon or heptagon) distortions in the carbon nanotubes. Second-order peaks, which are over-tones of the first-order peaks, are also labeled as *G'* at 2710 cm^{-1} and *D+G* at 2950 cm^{-1},.

4.3.2 CNT deposited under other conditions

In addition to randomly oriented CNT, we also synthesized vertically aligned CNT arrays on SiO_2 coated Si substrates and carbon nanofibers with CH_4/H_2 feedstock gases.

Reproduced with permission of the copyright owner. Further reproduction prohibited without permission.

We first present the vertically aligned carbon nanotube deposition. Figure 4.10 shows vertically aligned carbon nanotube arrays deposited with 20% C_2H_2 in NH_3 at a substrate temperature of 680 °C, an RF power of 700 W, a total gas pressure of 1 Torr, a DC bias of +50 V, and a deposition duration of 12 minutes. The substrates were Si wafers coated with a layer of SiO_2, 365 nm thick. The Ni catalyst was patterned by nanosphere lithography using 400 nm diameter silica nanospheres as masks. Since the silica nanospheres were not self-assembled, irregular patterns, rather than periodic ones, were formed. However, the catalyst size and therefore the nanotube diameter, was ~50 nm, similar to that patterned using 419 nm diameter self-assembled polystyrene nanospheres as masks. The higher magnification SEM image (Figure 4.10(b)) shows the Ni catalyst is located at the top of the nanotubes, indicating that the vertically aligned nanotubes formed via a tip-growth mechanism.

It is believed that the SiO_2 buffer layer between the catalyst and Si substrate is the key for tip-grown carbon nanotubes. Chhowlla *et al.*, synthesized vertically aligned carbon nanotubes on Si with a layer of SiO_2 as substrates using the DC PECVD method.[40] The SiO_2 thin film acted as a buffer layer to promote tip-growth. Titanium and Chromium are also commonly used as buffer layers for aligned nanotube growth. Another possible factor for vertically aligned CNT formation is the DC bias applied on the sample stage and substrate.

In addition to vertically aligned CNT, we also deposited CNT using CH_4 and H_2 as feedstock gases. The SEM image in Figure 4.11 reveals nanotubes deposited with 20% CH_4 in H_2 at a substrate temperature of 680 °C, an RF power of 700 W, a total gas pressure of 1 Torr, and a deposition duration of 5 minutes. Very few nanotubes were

Reproduced with permission of the copyright owner. Further reproduction prohibited without permission.

observed, as shown in the image. When using CH_4/H_2 gases for CNT deposition, growth was slow, probably because the dissociation rate of CH_4 is low in the capacitively coupled plasma. However, it is clear that the one-dimensional carbon nanotubes began to grow using capacitive CH_4/H_2 plasma. This result is helpful when explaining the carbon nanosheet growth mechanism, which will be discussed in Chapter 6.

4.4 Field emission of CNT-based, back-gated devices

Due to their electric conductivity, robustness, and high aspect ratio, carbon nanotubes have shown promise as a field electron emission material. Researchers have investigated the field emission from CNT using traditional front-gated triode structures. We studied the field emission of CNT in a novel back-gated structure.[41] Theoretical modeling shows that back-gated structures provide ample electron field emission, while reducing electric shorting of the gate to the cathode, previously shown to be a key device failure mechanism in front-gated structures.[42] A CNT-based back-gated field emission device structure is shown schematically in Figure 4.12.

This back-gated device was fabricated on highly conductive (0.005 Ω·cm) n-type Si wafers. A 500 nm thermal oxide was grown on the wafers to provide the dielectric barrier for the gate electrode. A blanket layer of tungsten (W), typically 150 nm thick, was deposited via sputtering onto the front surface of the oxidized Si wafers as an underlying cathode contact layer. A blanket 10 nm Ni catalyst layer was sputter deposited on top of the W layer for CNT growth. The substrate was then patterned by photolithography and reactive ion etched in a sulfur hexafluoride plasma to remove the W contact layer together with Ni on top of it. The photoresist was removed using a resist

Reproduced with permission of the copyright owner. Further reproduction prohibited without permission.

stripper, Shipley 1165. After being pre-etched in an inductive NH_3 plasma to optimize the Ni catalyst size, the patterned substrates were used to deposit carbon nanotubes under the typical conditions described in section 4.3.

After CNT deposition, the back-gated device was dipped into a buffered hydrofluoric acid (HF) solution for 10 seconds to clean the amorphous carbon and co-depositions in the street areas between the cathode lines. Figure 4.13 shows the SEM images of a back-gated device after CNT deposition and HF cleaning. The street areas between the lines are clean, and CNT were only found on top of cathode lines. The CNT have a non-uniform diameter distribution; the nanotubes at the line edges have smaller diameters while these at the center have larger diameters. The non-uniform CNT diameter distribution is because the Ni catalyst islands, treated only in NH_3 plasma etching, have non-uniform sizes.

We have characterized the field emission of this back-gated device using a triode I-V curve measurement at a background pressure of $\sim 10^{-7}$ Torr. The turn on field was 0.5V/μm; the device yields a stable emission current of 30 μA at an electric field of 1.5V/μm. Though the results are promising, we replaced carbon nanotubes with carbon nanosheets as the cathode materials, due to the easier fabrication of a CNS device, and a longer electron emission lifetime of carbon nanosheets, as will be discussed in Chapter 5.

4.5 Summary

We developed a nanosphere lithography technique to obtain periodic arrays of nanometer sized catalyst islands. Carbon nanotubes were deposited in capacitive coupled RF

Reproduced with permission of the copyright owner. Further reproduction prohibited without permission.

PECVD on Ni catalyst patterned Si substrates, with and without a SiO_2 buffer layer in between.

We derived the single-layer and double-layer NSL patterns and calculated the size of the patterns for single-layer and double-layer NSL. Polystyrene nanospheres 419 nm in diameter were used as masks. AFM and SEM were used to observe the morphology and topology of the nanosphere masks, as well as the Ni catalyst particle patterns found after removal of the nanosphere masks. Silica nanospheres 400 nm in diameter were used as masks as well, but in this case the pattern was irregular.

The patterned Ni catalyst coalesced to round dots upon heating/etching in inductive NH_3 plasma before CNT growth. We grew carbon nanotubes in a capacitively coupled plasma of 20% C_2H_2/NH_3. Typical conditions for CNT growth are ~700 °C, 1 Torr, and 700 W for substrate temperature, total gas pressure, and input RF power, respectively. SEM observations indicate that typical CNT form via a base-growth mechanism, and are randomly oriented.

Vertically aligned CNT arrays were formed when using a Si substrate coated with a SiO_2 layer. The vertically aligned CNTs formed via a tip-growth mechanism. Carbon nanotubes were also deposited in a capacitively coupled plasma of 20% CH_4/H_2 with other conditions the same as for typical CNT deposition.

We fabricated a novel back-gated field emission device using CNTs as cathode electron emission materials; the field emission properties measured in a triode testing system are promising.

Our studies on CNT deposition in the RF PECVD system is a comparison to the carbon nanosheet deposition in the same system using an inductively coupled plasma.

Reproduced with permission of the copyright owner. Further reproduction prohibited without permission.

The results of CNT deposition are helpful in understanding the carbon nanosheet formation mechanism. A detailed analysis of the carbon nanosheet formation mechanism will be presented in Chapter 6.

Reproduced with permission of the copyright owner. Further reproduction prohibited without permission.

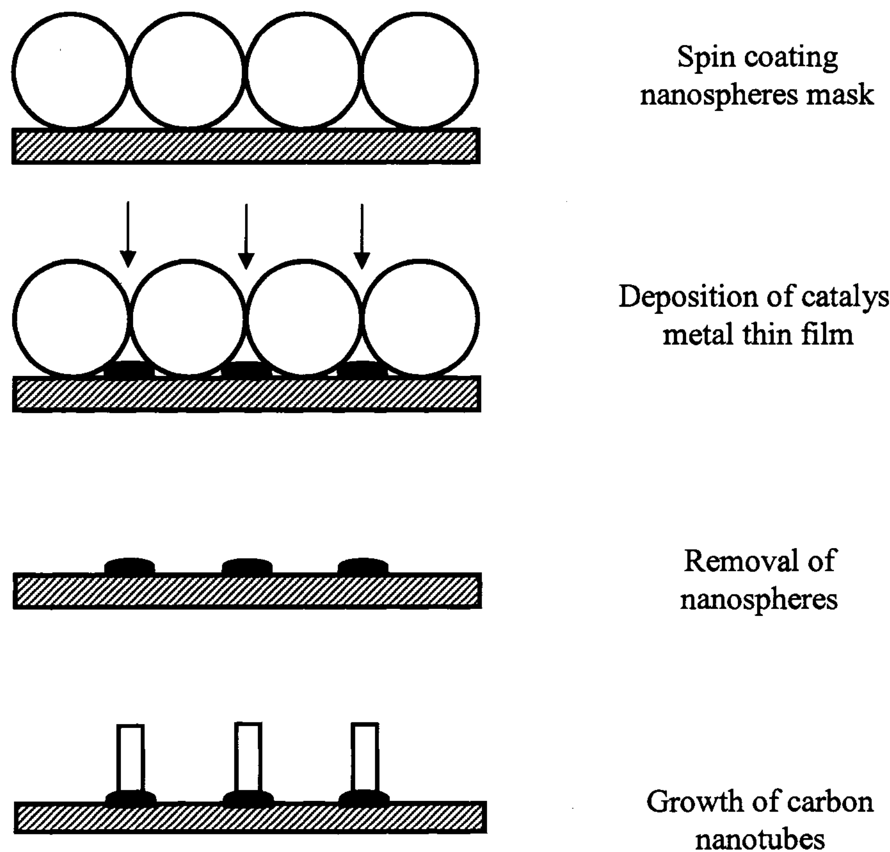

Figure 4.1: Schematics showing the nanosphere lithography (NSL) processes.

Reproduced with permission of the copyright owner. Further reproduction prohibited without permission.

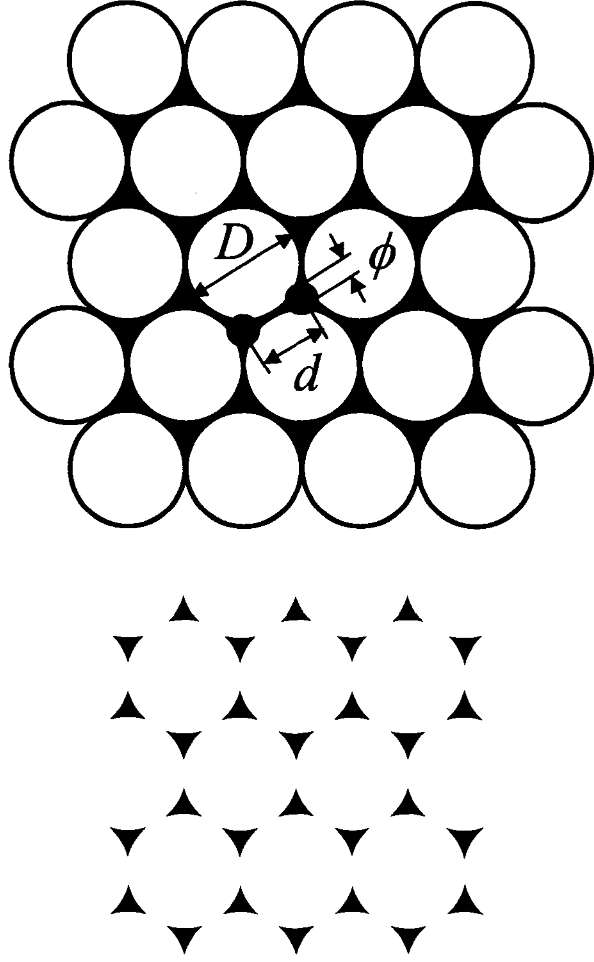

Figure 4.2: Schematics of single-layer nanosphere lithography (NSL). Holes between the adjacent spheres are triangular-shaped and form a hexagonal pattern.

Reproduced with permission of the copyright owner. Further reproduction prohibited without permission.

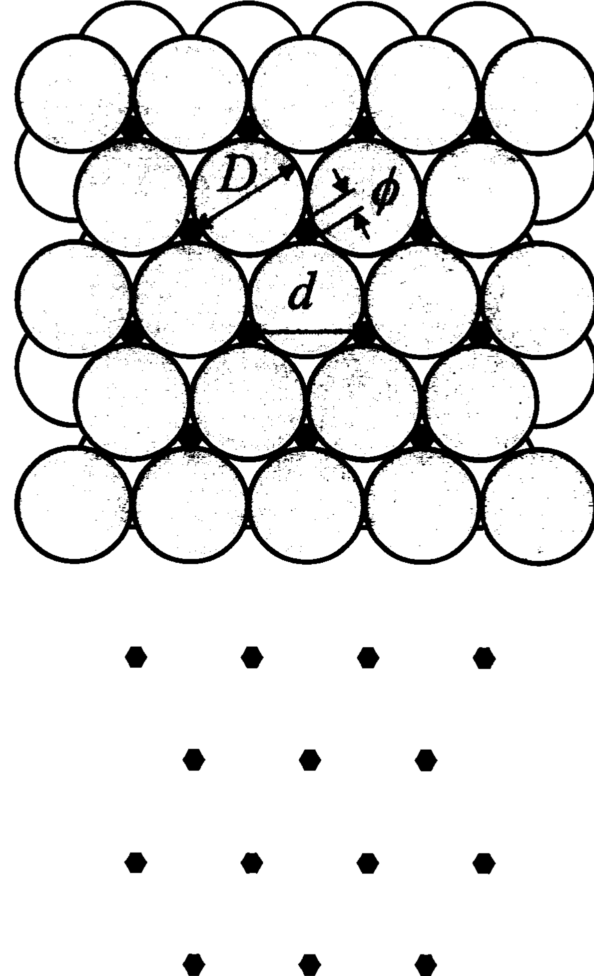

Figure 4.3: Schematics of double-layer nanosphere lithography (NSL). Holes are hexagonal-shaped and form a triangular pattern.

Reproduced with permission of the copyright owner. Further reproduction prohibited without permission.

Table 4.1: List of calculated values of size and distance of the catalyst dots patterned by single-layer and double-layer nanosphere lithography using spheres with diameters of 419 nm, 269 nm, 171 nm, and 100 nm, respectively.

D **(nm)**	**419**	**269**	**171**	**100**
d_{SL} (nm)	241	155	99	58
ϕ_{SL} (nm)	96	62	39	23
d_{DL} (nm)	419	269	171	100
ϕ_{DL} (nm)	66	43	27	16

Reproduced with permission of the copyright owner. Further reproduction prohibited without permission.

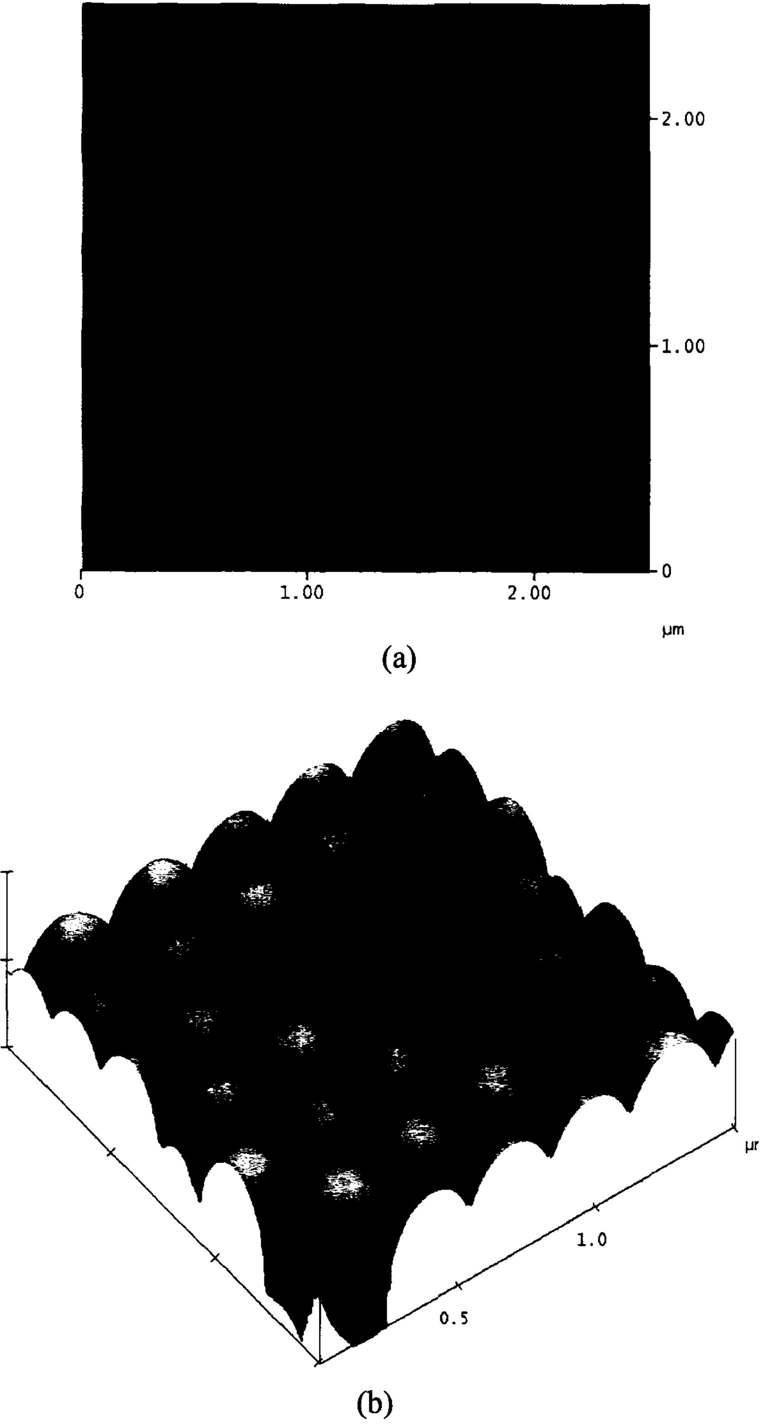

Figure 4.4: Top-view (a) and side view (b) AFM images of the 419 nm polystyrene nanospheres spin-coated on a Si substrate. The spheres self assembled to a periodic array.

Reproduced with permission of the copyright owner. Further reproduction prohibited without permission.

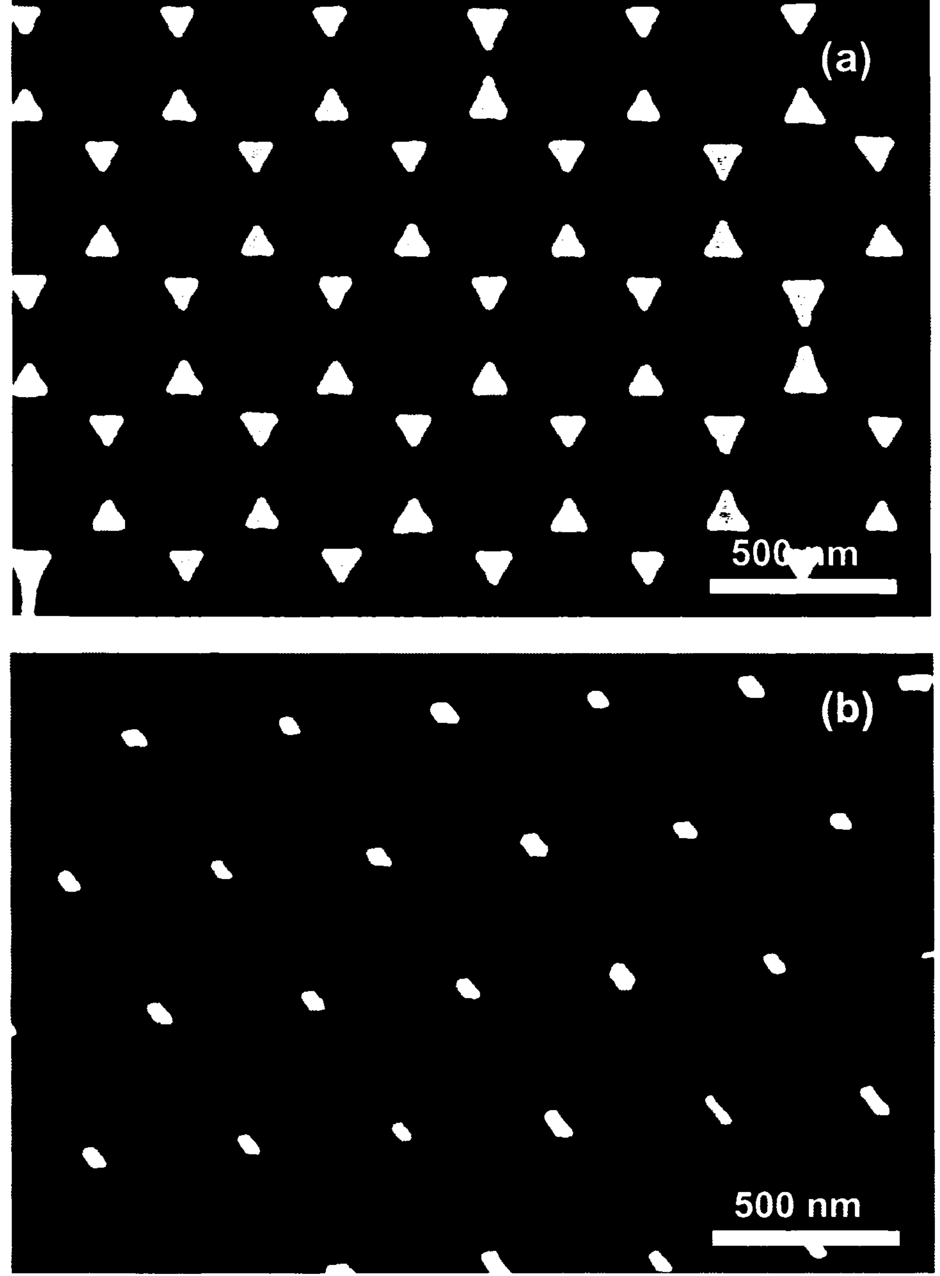

Figure 4.5: Single-layer (a) and double-layer (b) pattern of Ni islands coated on the substrate after removal of the self-assembled polystyrene nanosphere masks, 419 nm in diameter.

Reproduced with permission of the copyright owner. Further reproduction prohibited without permission.

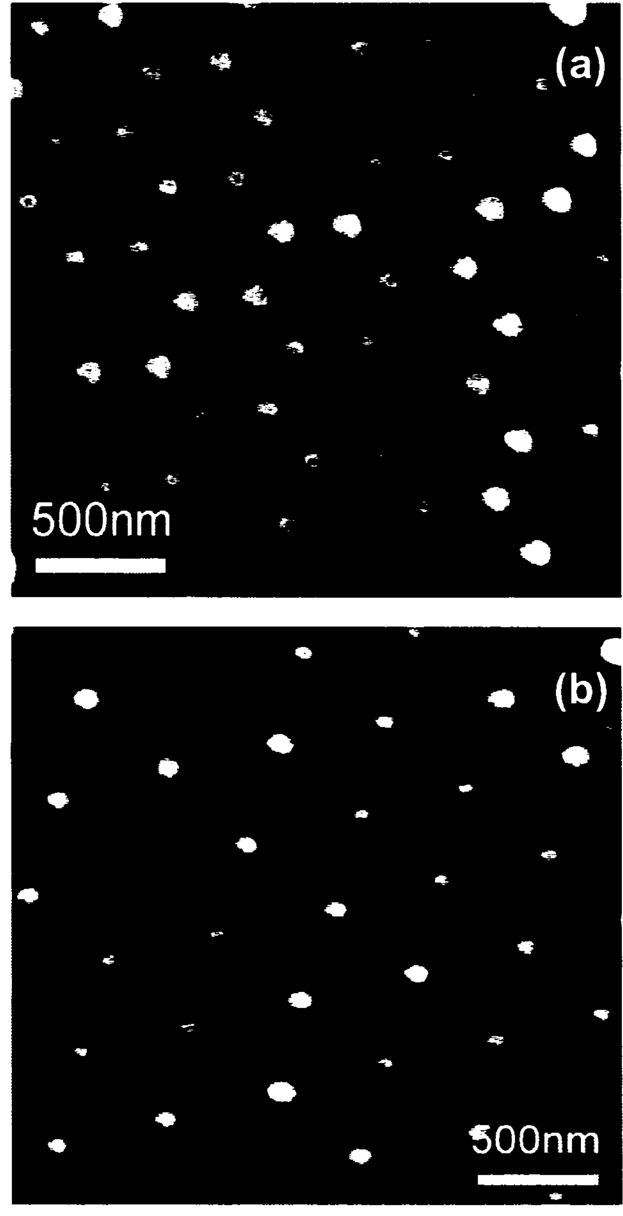

Figure 4.6: AFM images of single-layer (a) and double-layer (b) Ni islands coalesced to round dots after heating and etching in inductive plasma.

Reproduced with permission of the copyright owner. Further reproduction prohibited without permission.

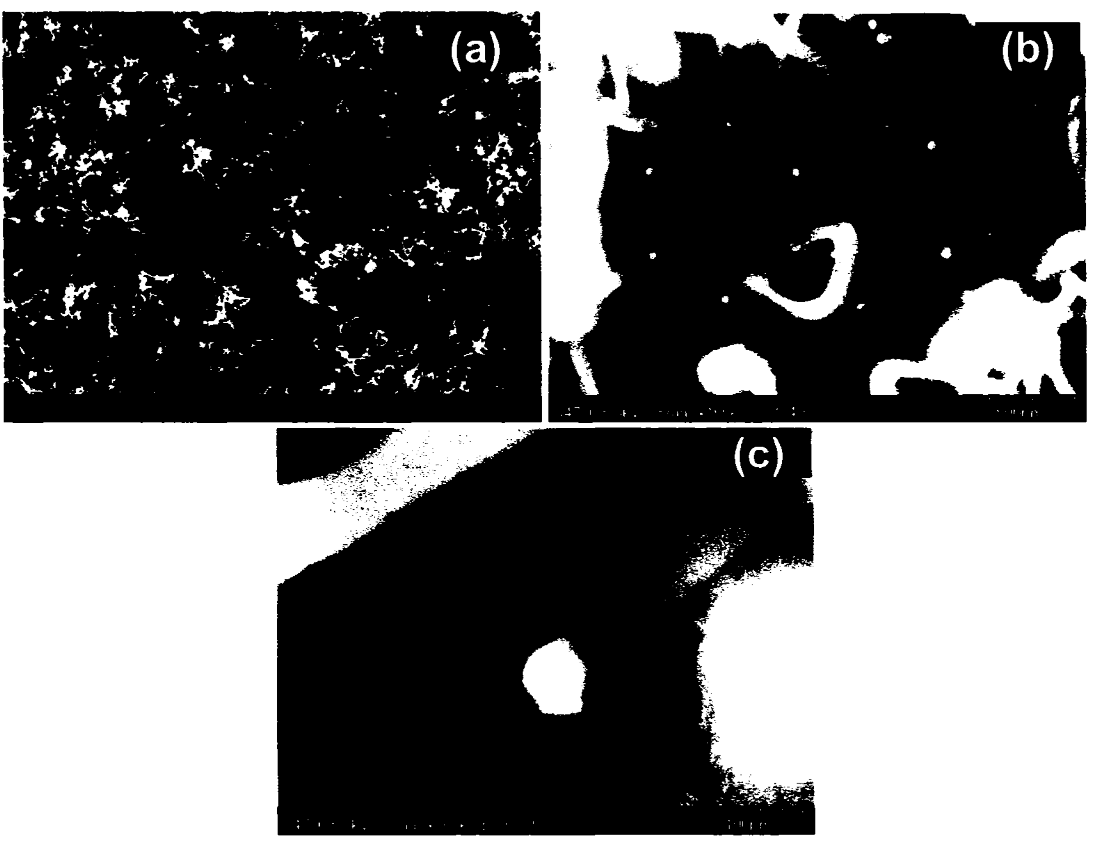

Figure 4.7: SEM images of randomly oriented CNT grown at typical conditions. (a) Low magnification image shows the overall morphology of the CNT. (b) The hexagonal pattern of the Ni catalyst at the root of each CNT. (c) High magnification image indicates a base-growth mechanism of typical CNT.

Reproduced with permission of the copyright owner. Further reproduction prohibited without permission.

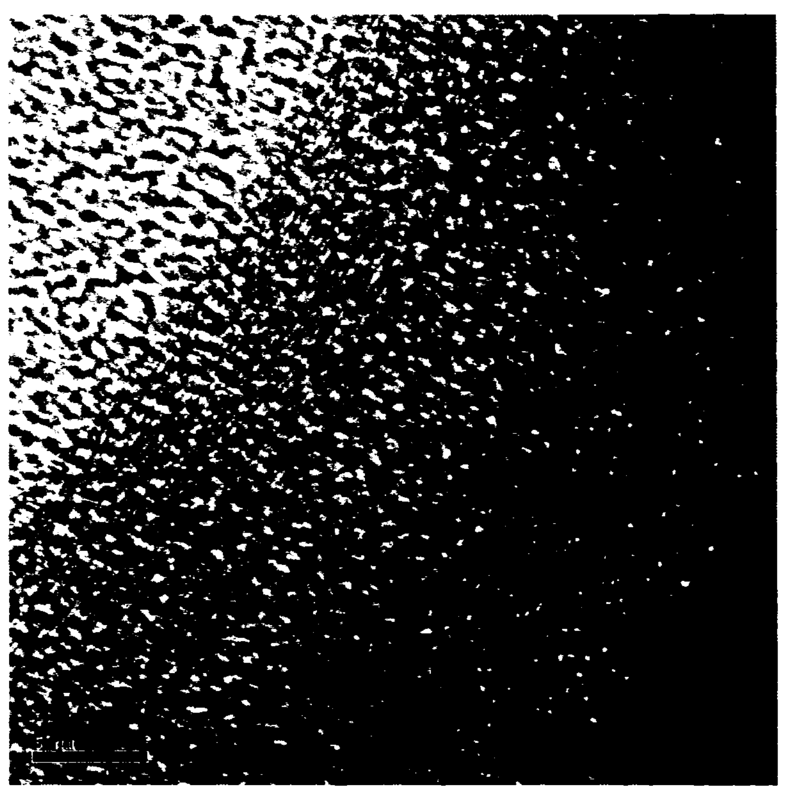

Figure 4.8: High resolution transmission electron micrographic of a typical CNT sample. A hollow center is observed between the parallel fringes, which are parallel to the tube axis.

Reproduced with permission of the copyright owner. Further reproduction prohibited without permission.

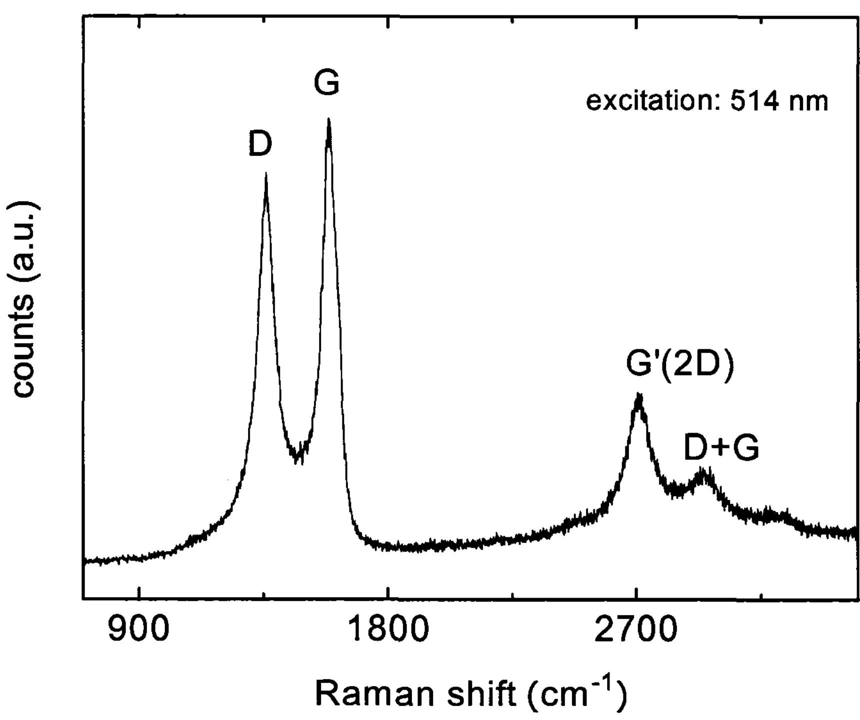

Figure 4.9: Raman spectrum of a typical CNT sample. The excitation laser wavelength is 514 nm.

Reproduced with permission of the copyright owner. Further reproduction prohibited without permission.

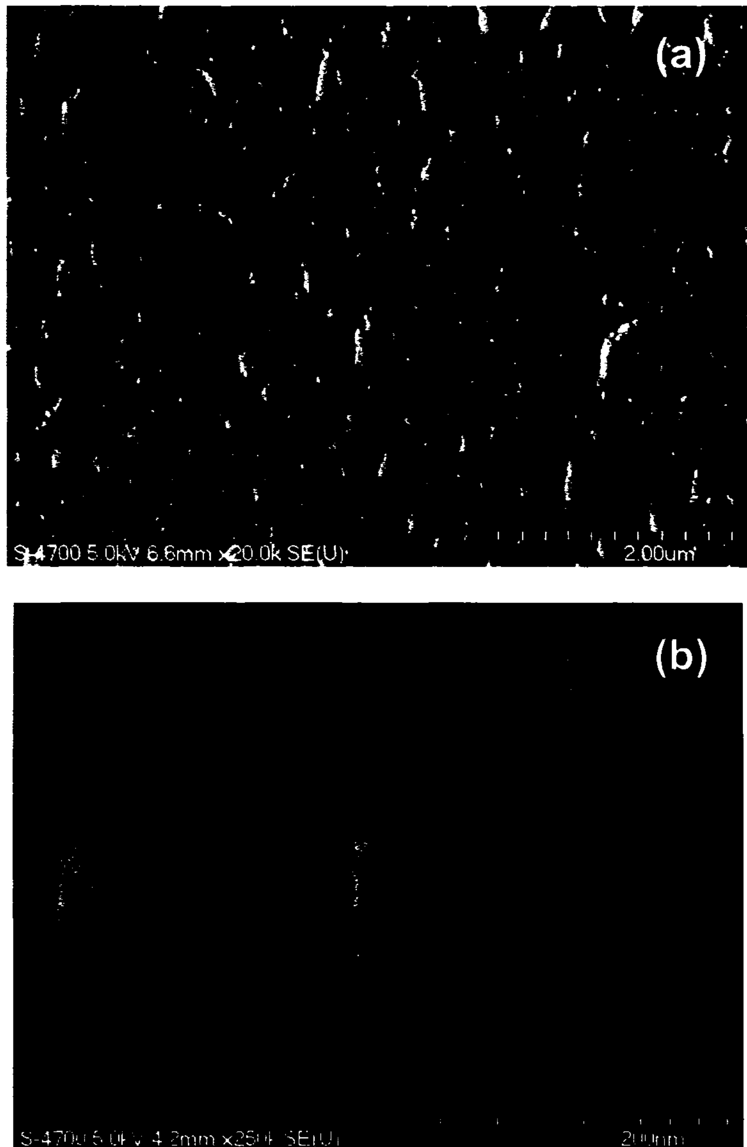

Figure 4.10: Low magnification (a) and high magnification (b) SEM images of aligned CNT arrays deposited on a SiO_2/Si substrate with +50 V DC bias applied during deposition.

Reproduced with permission of the copyright owner. Further reproduction prohibited without permission.

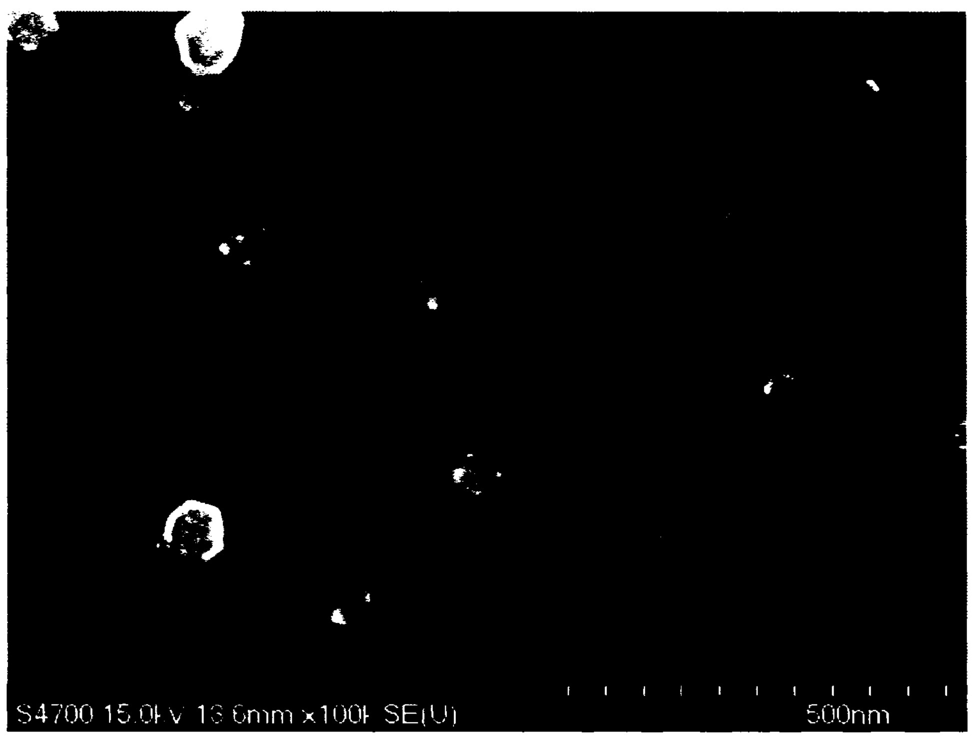

Figure 4.11: SEM image of a one-dimensional CNT structure deposition using capacitively coupled CH_4/H_2 plasma for 5 minutes. Other conditions are the same as typical CNT depositions.

Reproduced with permission of the copyright owner. Further reproduction prohibited without permission.

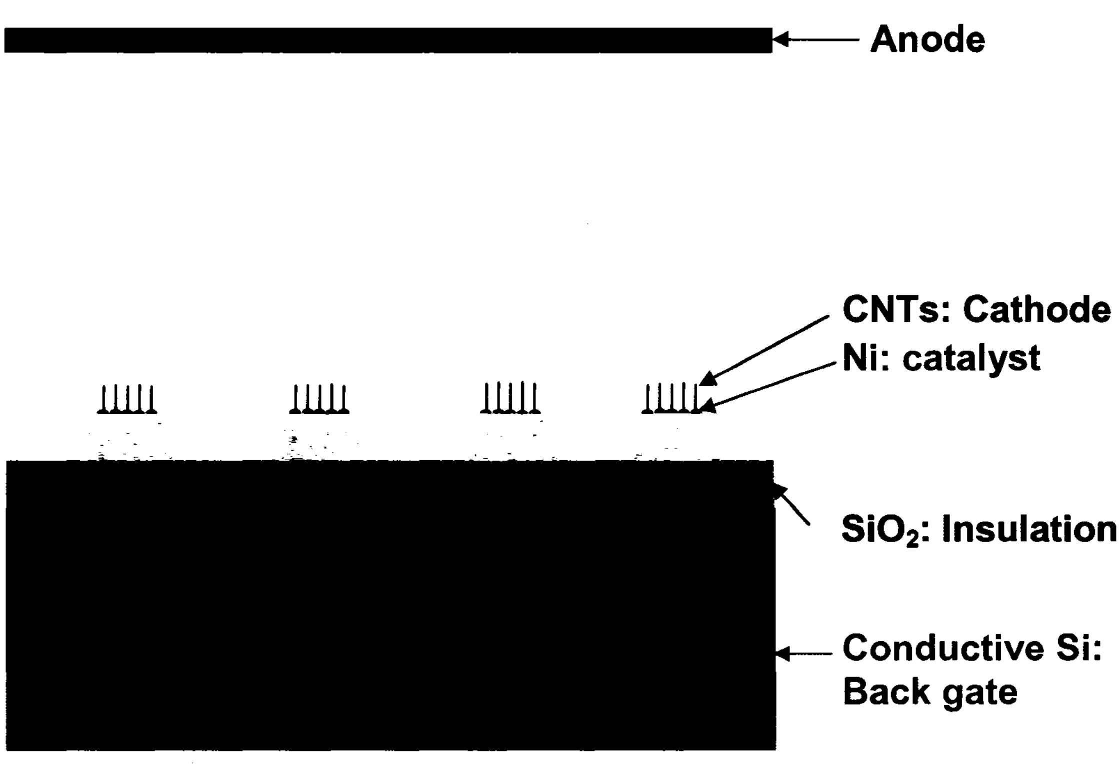

Figure 4.12: Schematics of a novel back-gated field emission device, using CNT as the cathode material.

Reproduced with permission of the copyright owner. Further reproduction prohibited without permission.

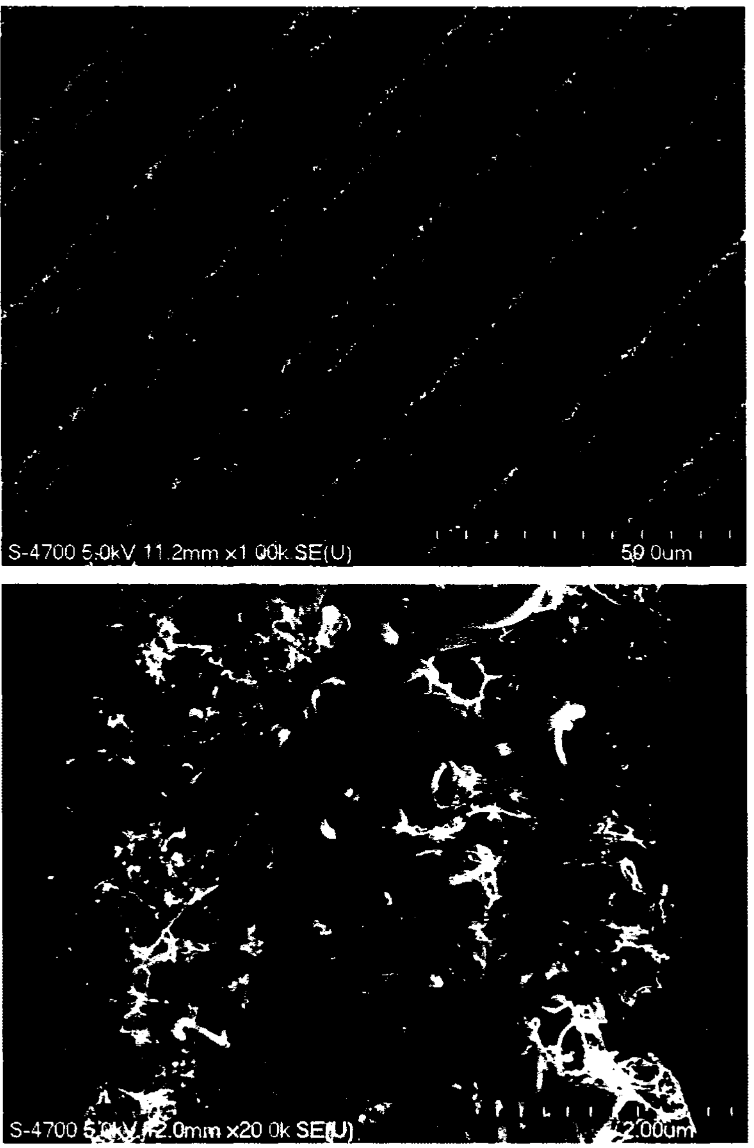

Figure 4.13: Low magnification (a) and high magnification (b) SEM images of the cathode lines in a CNT-based back-gated device. The street areas between the lines were cleaned by HF dipping.

Reproduced with permission of the copyright owner. Further reproduction prohibited without permission.

Chapter 5

Carbon Nanosheet: Experimental Deposition and Characterization

5.1 Introduction of CNS synthesis

This chapter outlines the deposition, structure, and properties of a two-dimensional (2-D) carbon nanostructure — carbon nanosheet (CNS) — prepared by inductively coupled radio frequency (RF) plasma enhanced chemical vapor deposition (PECVD). The results of a parametric study for CNS deposition, modification of CNS, and the application of CNS in field emission and other research areas, are presented. Part of the results presented in this chapter have been reported by our group in several other publications.[2,26,33,39,42-46]

Sheet-like carbon materials were first observed as co-depositions of carbon nanotubes prepared by arc-discharge and laser ablation methods.[47-49] However, the synthesis of 2-D carbon nanostructures was not studied until 1997, when Ando *et al.*,[8]

Reproduced with permission of the copyright owner. Further reproduction prohibited without permission.

reported the synthesis of petal-like graphitic sheets as a by-product of a carbon nanotube synthesis process, using hydrogen arc discharge.

After that, 2-D carbon nanostructures were synthesized using various methods. Shang *et al.*,[10] and Itoh *et al.*,[11] synthesized carbon nanoflakes and nanowalls by hot filament (HF) CVD methods; Wu *et al.*,[3] and Chuang *et al.*,[9] synthesized carbon nanowalls by microwave (MW) PECVD; and Hiramatsu *et al.*,[31] and Shiji *et al.*,[12] reported fabrication of carbon nanowalls by capacitively coupled radio frequency (RF) PECVD assisted by hydrogen radical injection. Usually, these materials are vertically-oriented relative to the substrate, and are about tens of nanometers in thickness. Catalysts are used in some of the syntheses mentioned above.

Sheet-like graphitic structures were also synthesized using a mechanical exfoliation method. Chen *et al.*,[13] obtained exfoliated graphite nanosheets via an acid intercalation procedure. Novoselov *et al.*,[14] fabricated atomically thin carbon films by mechanical exfoliation and characterized the electric field effect in such films. However, exfoliated carbon nanosheets lie flat on the substrate surface and therefore are not useful for certain device purposes that require vertical orientation.

Two-dimensional carbon nanosheets have also been synthesized by chemical routes. Viculis *et al.*,[15] observed the formation of graphitic nanosheets when stoichiometrically intercalated graphite reacted with an ethanol aqueous solvent, and the nanosheets curled to form nanoscrolls upon sonication. Kuang *et al.*,[50] synthesized carbon nanosheets using a low temperature solvothermal method. However, the complicated procedures and hazardous reagents involved in these chemical synthesis methods do not make them viable options for CNS deposition.

Reproduced with permission of the copyright owner. Further reproduction prohibited without permission.

Our group reported the synthesis of carbon nanosheets via an inductively coupled radio frequency (RF) plasma enhanced chemical vapor deposition (PECVD).[2,33,43,44] Compared to previous reports, our CNS are free-standing, atomically thin, and free of catalyst and other allotropes of carbon. The following sections will present CNS deposition methods, structures, and properties; the results of a parametric study, and potential applications of CNS in various fields.

5.2 Deposition and properties of typical CNS

We deposited carbon nanosheets on a variety of substrates in the inductively coupled plasma from CH_4 diluted at various concentrations (5-100%) in a H_2 atmosphere, at total gas pressures of 20-400 mTorr, substrate temperatures of 600-950 °C, and RF input powers of 400-1200 W. This section presents the deposition, morphology, composition, and structure of CNS, as well as certain properties of typical CNS, including field emission, resistivity, and specific surface area.

5.2.1 Typical CNS deposition

Typical CNS were deposited in an inductively coupled plasma with 40% CH_4 (4 sccm) diluted in a H_2 (6 sccm) atmosphere. Other parameters are 100 mTorr total gas pressure, 680 °C substrate temperature, and 900 W input RF power. The CNS discussed in the following sections were deposited on Si wafers for 20 minutes, unless otherwise noted.

5.2.2 SEM and TEM of typical CNS

Reproduced with permission of the copyright owner. Further reproduction prohibited without permission.

Figure 5.1 shows SEM (Hitachi S-4700) micrographics of typical CNS. Figure 5.1(a) is a top view image of a typical CNS. This image reveals CNS approximately 1 μm long, with a smooth surface topography and a corrugated nature with very sharp edges. The high magnification image in Figure 5.1 (b) reveals an individual CNS edge approximately 1 nm thick. The edge may be even thinner, but our measurements were limited by the SEM resolution. The overall translucent appearance of the CNS also suggests a thin, uniform thickness along the entire plane.

Figures 5.1(c) and (d) are low and high magnification SEM images of typical CNS directly deposited on a Ni TEM grid, in which both top-view and cross-section views are presented. At the curved edge of the grid wire, it is clear that the nanosheets are "free-standing" having a roughly vertical orientation, relative to the substrate. By "free-standing" we mean that the vertical sheets ascend from the base layer of the substrate without auxiliary lateral support.

The height of nanosheets is measured using cross-section SEM images of cleaved, as-deposited samples. Figure 5.1(e) shows one such image of typical CNS deposited on a SiO_2 coated Si wafer. It also indicates the vertical orientation of the CNS.

We used eighteen (18) different substrates for CNS deposition, including Si, Al_2O_3, SiO_2 (quartz), Ni, Ti, W, TiW, Mo, Cu, Au, Pt, Zr, Hf, Nb, Ta, Cr, 304 stainless steel, and graphite. We successfully grew CNS on all of these substrates. Figure 5.2 shows SEM images of CNS grown on six different substrates using typical experimental parameters. The basic morphologies of the nanosheets did not change with variations in substrate material. This non-selective growth trait of CNS is a great advantage for many technological applications, compared to the catalyst-dependent growth trait of CNT.

Reproduced with permission of the copyright owner. Further reproduction prohibited without permission.

Figure 5.3 shows TEM (JEOL JEM 2010F, 200 keV) images and electron diffraction patterns of the CNS grown directly on a TEM grid, similar to the sample shown in Figures 5.1(c) and (d). Figure 5.3 (a) is a low magnification image showing several nanosheets grown vertically to the grid surface. Figures 5.3 (b), (c), and (d) are high resolution TEM micrographs with arrows indicating two parallel fringes with a distance of 0.34 to 0.37 nm. These fringes indicate two atomic layers with approximately the (002) spacing of graphite (0.335 nm). We have observed many nanosheets having edges 1-2 layers thick.

Electron diffraction from nanosheets detected in TEM (Figure 5.3(e)) shows graphite patterns labeled (002), (004), (100), (101), (110), and (112). The (002) spacing was calculated to be 0.36 nm, falling within the range of the distance between the parallel fringes. This diffraction result indicates a graphitic structure for CNS, which is confirmed in the following sections by Raman and X-ray diffraction investigations.

5.2.3 AES and XPS of typical CNS

Carbon nanosheets grow without catalyst, and therefore have no catalyst impurities. We have analyzed typical CNS samples with Auger electron spectroscopy (AES) and X-ray photoelectron spectroscopy (XPS); no contamination was detected.[44]

Figure 5.4 (a) shows a typical AES (Perkin-Elmer PHI660, 3 keV) spectrum of carbon nanosheets. It can be seen that, besides the C feature, only a very small amount of oxygen (O 1s peak at 533 eV) was detected in the overall spectrum. A typical XPS (VG Escalab II, Mg K_α) spectrum, as shown in Figure 5.4(b), gives similar results; *i.e.* other than the C 1s peak, only a very small oxygen signal (O *KLL* peak at ~503 eV) is present.

Reproduced with permission of the copyright owner. Further reproduction prohibited without permission.

The oxygen was most likely introduced from ambient exposure rather than from the plasma sputtering of the quartz window, in which case both Si and O signals would be present in the spectra.

5.2.4 PIXE, ERDA, and TDS of typical CNS

Since the sensitivity of AES and XPS is relatively low, we used the PIXE (particle induced X-ray emission) technique to detect metal contamination at a higher sensitivity of "parts per million" (ppm) level. Because the nanosheets are grown in a hydrogen rich plasma, hydrogen is inevitably adsorbed and/or incorporated into CNS during their growth. In addition to PIXE testing, we also conducted ERDA (elastic recoil detection analysis) and TDS (thermal desorption spectrometry) experiments to detect the concentration of hydrogen in the nanosheets.

Figure 5.5 shows representative PIXE spectra of nanosheet samples deposited on Si and graphite substrates. The incident particles were protons (H^+, 2.5 MeV) with a beam spot 0.5 mm in diameter. The incident beam current was 0.5 nA and the total fluence of incident charge was 5×10^{-8} C. Only elements heavier than sodium (Na) can be detected, so the C signal is not present in these spectra. The fitted data, and the spectrum for CNS grown on a Si wafer, have only one peak identified as Si; while for CNS grown on graphite substrates, no element was detected. These results indicate that the concentration of metal elements in CNS is lower than the metal elements' detection limits, which are 71.4 ppm for Chromium (Cr) and 72.9 ppm for Nickel (Ni). Therefore, when using the inductively coupled RF PECVD process for CNS deposition, sputtering from the chamber wall or the sample stage is negligible.

Reproduced with permission of the copyright owner. Further reproduction prohibited without permission.

Figure 5.6 (a) shows the ERDA spectrum and the fitted curve of a typical CNS sample. The incident particles were Helium ions (He^+, 2.3 MeV) with an incident angle of 75°. The incident beam current was 60 nA and the total fluence of incident charge was 4×10^{-5} C. Recoiled particles were detected at an exit angle of 60°. The data was fitted using software SIMNRA version 5.02, and the results indicate that the hydrogen density in typical CNS samples is 7.5×10^{16} atoms/cm^2.

Thermal desorption from CNS samples was recently reported by our group.[26] Figure 5.6 (b) shows typical hydrogen thermal desorption spectrum of CNS deposited on a Ta substrate, at a 15 K/s temperature ramp rate. The six peaks were fitted via the Polanyi-Wigner equation.[26] The hydrogen density calculated from TDS results, however, was $\sim2.4\times10^{17}$ atoms/cm^2. The difference between the ERDA measurements and the TDS measurements may be a result of several factors. For example, the roughness of the CNS was not considered in the ERDA data fitting. In addition, the samples for the ERDA and TDS measurements had different heights which could also account for the difference in measurements. Finally, there might be other H sources in the TDS measurements, which were not present in ERDA. These factors may account for the fact that the two measurements differ by roughly a factor of three. However, both experiments indicate agree on the presence of large amounts of hydrogen in the CNS samples.

5.2.5 Raman and FTIR of typical CNS

Raman spectroscopy is widely used to investigate the structures and properties of carbon materials, such as highly ordered pyrolytic graphite (HOPG), diamond, carbon nanotubes,

Reproduced with permission of the copyright owner. Further reproduction prohibited without permission.

and graphite-like materials. We used Raman spectroscopy to study the structure of carbon nanosheets.

Figure 5.7 shows representative Raman spectra of typical carbon nanosheet samples. In Figure 5.7 (a), the spectrum was excited with a 514 nm wavelength laser; the first-order peaks are identified as *D* peak, *G* peak, and *D'* shoulder at 1350 cm^{-1}, 1580 cm^{-1}, and 1620 cm^{-1}, respectively. The overtones of the first order peaks are also labeled as 2*LO*, *G'*, *D*+*G*, and 2*D'*.

The sharp *G* peak indicates the crystalline nature of the nanosheets, and the sharp *D* peak indicates that nanosheets have a certain number of defects that may include vacancies and distortions of graphene sheets which lead to the non-uniformity, the corrugation and the twisting of nanosheets. The intensity ratio of the *D* peak and the *G* peak, I_D/I_G, is commonly used to characterize the defects present in carbon materials. An empirical equation, $L_a = \frac{44}{(I_D/I_G)}$ (Å), was previously derived[51] and is commonly used to estimate the in-plane crystallite length of graphitic materials. The I_D/I_G ratio for a typical nanosheet sample, for example, from Figure 5.7 (a), is ~0.44, which gives a crystallite length of ~10 nm. However, this does not mean that the size of the nanosheets is 10 nm. Rather, the crystalline length is the average size of the nanosheets within which the C atoms are periodically arranged.

Low energy peaks at 228 cm^{-1}, 355 cm^{-1} and 864 cm^{-1}, which have not been observed in bulk carbon materials or thick carbon materials, were observed from carbon nanosheets, as shown in Figure 5.7 (b), with a 633 nm excitation laser wavelength. Since the nanosheets are only a few atomic layers thick, the confinement in the stacking direction (*c*-axis) is weak; such weak confinement may activate some phonon vibrational

Reproduced with permission of the copyright owner. Further reproduction prohibited without permission.

modes. The 228 cm^{-1} and 355 cm^{-1} peaks are analogous to the radial breathing modes (RBM) of single-walled carbon nanotubes. The CNS are folded and corrugated with a small radius of curvature at their ridges, and have local structures similar to single walled carbon nanotubes. Consequently, these CNS may show similar behaviors to SWNT from the lattice dynamic point of view.

The weak peak at 864 cm^{-1} has two possible origins. One is similar to an in-plane vibrational mode in carbon nanotubes. The other more likely explanation, is an infrared-active out-of-plane mode in graphite. The shape of the 864 cm^{-1} peak is also similar to that in the infrared spectrum.[52] This infrared active mode may become Raman-active with the presence of large amounts of defects in the nanosheets.

The positions and/or intensities of some peaks in CNS Raman spectrum are dependent on the excitation laser wavelength (or energy), as revealed by Figure 5.8. When the excitation laser energy decreases (or the wavelength increases), the *D* peak and the two lowest energy peaks originating from the ridges, shift their positions towards the lower end of the spectrum, and their intensities increase. In Figure 5.8, the 864 cm^{-1} peak position does not change, but its intensity increases. Similarly, the *G* peak and *D'* shoulder positions do not move, although the intensity of the *G* peak decreases while the intensity of the *D'* shoulder increases. Another very weak peak around 1140 cm^{-1}, which is assigned to *trans*-polyacetylene in diamond films and possibly originated from the edges of nanosheets, also changes its position and intensity when the laser energy/wavelength changes.

We also analyzed FTIR absorption spectrum of typical CNS samples mixed with KBr powder and pressed into pellets. Since CH_4 and H_2 were used for typical CNS

Reproduced with permission of the copyright owner. Further reproduction prohibited without permission.

growth, hydrogen was incorporated into the nanosheets during deposition. An obvious absorption at ~2900 cm^{-1}, due to the C-H stretching vibration, was observed in representative spectrum, as shown in Figure 5.9. The results, indicative of the presence of large quantities of hydrogen, are consistent with previous ERDA and TDS results.

5.2.6 X-ray diffraction of typical CNS

Since the 1930's, X-ray diffraction has been used to investigate the crystalline structure of carbon materials. Our group reported the use of XRD to detect the structure of carbon nanosheets and how it changes as a function of substrate temperature.[45]

Symmetric and asymmetric geometries of glancing angle XRD, as schematically shown in Figure 2.9 (c) and (d), were used to detect the structural details of the horizontally and the vertically oriented nanosheets, respectively.

XRD spectrum of a typical carbon nanosheet sample, collected in the asymmetric geometry, is presented in Figure 5.10. The diffraction peaks are indexed as hexagonal graphite: (002), (10), (101), (004), (11), (006), and (20). The (10), (11), and (20) peaks have long high-angle tails, which are characteristic of turbostratic carbon and only labeled as (*hk*) indices. Reflections of (00*l*) type are expected in crystalline structure as well as turbostratic carbon. However, the (101) reflection can only originate from crystalline graphite structures. Therefore, the XRD spectrum proves that CNS are true crystalline graphitic structures containing some defects, which is consistent with the Raman spectroscopy results.

For typical CNS, the uncorrugated length (L_a) and thickness (L_c) calculated from asymmetric XRD are 10.7 nm and 2.7 nm, respectively.[45] The L_a, similar to the L_a

Reproduced with permission of the copyright owner. Further reproduction prohibited without permission.

derived from the I_D/I_G ratio in Raman spectrum, is not equivalent to the total length of the nanosheets, but the uncorrugated length of the area within the CNS. The L_c, ranging from 5 to 9 graphene layers, is a bit larger than our best estimation from the electron micrographs, as presented in section 5.2.2. However, since the XRD detected the average thickness over all the samples, it is possible that the nanosheets are thicker toward their roots, therefore making the average thickness of a CNS sample larger than the average thickness of CNS at their edges.

Symmetric geometry XRD results correspond to the graphitic layers found parallel to the substrate which form a base layer. The uncorrugated length of these base layers is 3.7 nm, which is smaller than that of the vertically oriented sheets. This indicates that the base layers have more defects than the vertically oriented nanosheets, probably as a result of nucleation process.

5.2.7 Field emission of typical CNS

Recently, carbon nanotubes have been studied as field electron emission materials due to their unique electric properties and high aspect ratio. Carbon nanosheets have the same sharp atomic edges as CNT, and are also believed to be a good candidate for field emission cathode material.

We studied the field electron emission of carbon nanosheets using a customized diode testing system[46] as previously described in section 2.10.1. For the material testing, we measured the turn-on field, the maximum emission current, and the lift-time for stable emissions. Our results indicate that pristine CNS have low turn-on fields, high emission currents, and long life times, all of which make them ideal for use in field emission.

Reproduced with permission of the copyright owner. Further reproduction prohibited without permission.

The turn-on field of typical CNS samples ranges from 1-10 V/μm. Figure 5.11 (a) is a typical series of twenty repeating ramps of the emission current (*I*) *vs.* electric field (*E*) curves from a typical CNS sample. The turn-on field is 7.8 V/μm for an emission current density of 10 μA/cm^2. The inset of Figure 5.11 (a) is the corresponding Fowler-Nordheim plot. A complete discussion of Fowler-Nordheim theory can be found in Dr. Xin Zhao's dissertation.[22] The $\ln(J/E^2)$ *vs.* $1/E$ curve is an excellent straight line, indicating the field emission of CNS is not saturated, and closely follows the Fowler-Nordheim relationship, $J = A(\beta E)^2 \exp(-B\phi_e^{3/2} / \beta E)$, where J is the emission current density, ϕ_e is the effective work function, β is the geometric enhancement factor, and A and B are the constants for carbon nanosheets.

When the anode is cooled by conduction through a copper braid whose end is immersed in ice water outside the vacuum feedthrough, the total emission current of typical carbon nanosheets has a maximum value of 28 mA from an area 8×8 mm^2 when an electric field of 20 V/μm is applied, as shown in Figure 5.11 (b). Again, the straight Fowler-Nordheim plot shown in the inset means that the maximum emission current is not yet reached. As of the date of this writing, our highest emission current has been limited by our testing instrument, not by the material itself. Therefore, emission current density, ~0.44 mA/mm^2, is not high in this case. However, when a small anode is used, an emission current of ~2 mA was achieved from an area of 1 mm^2, which means the current density is at least as high as ~2 mA/mm^2. Recent experiments have shown that the emission current density may be very much higher; the intrinsic limits on current density have not yet been determined. Regardless of future increases in these numbers, both the 28 mA total emission current, and the 2 mA/mm^2 emission current density, are

Reproduced with permission of the copyright owner. Further reproduction prohibited without permission.

considerably greater than the values previously reported for carbon nanotubes and metal tip field emission emitters.[46]

Furthermore, the field emission of CNS is quite stable over time. The field emission lifetime was tested by iteratively applying voltage ramps for a long time duration. Each ramp was 100 seconds long with a duty factor of 14.9%, meaning the emission current was greater than 100 μA for 14.9% of the 100 seconds. During each ramp, the CNS yielded a DC current for 3 seconds at the maximum current, ~1.3 mA, therefore the maximum emission duty factor is 3%. Figure 5.12 (a) shows how the maximum current at each ramp changes with time; and the results indicate a stable emission with maximum current at ~1.3 mA for 200 hours, after which the test was terminated due to limitations of facility's operation. No degradation was observed during 7216 ramps occurring over a period of 200 hours, and we believe the emission's stability could last for an even longer time duration. Figure 5.12 (b) shows another sample being tested for a total of 24000 ramps over 120 hours. Each ramp was only 18 seconds with a duty factor of 19% and a maximum emission duty factor of 9.4%. Again, the emission remained stable over the entire period.

Their good field emission properties make CNS a promising cathode material for field emission devices, such as microwave tubes, field emission displays, and electron sources for electron microscopes. Section 5.4.4 will discuss a novel device, a CNS-based back-gated triode field emitter that our group has fabricated.

5.2.8 Four-point resistivity of typical CNS

Reproduced with permission of the copyright owner. Further reproduction prohibited without permission.

Electric conductivity, or resistivity, is one of the basic properties of a material. The electric properties of the CNS were measured using a four-point probe, as described in section 2.9.

Silicon dioxide (1×1 cm^2) was chosen as substrates for CNS coatings used for resistivity measurements, since quartz is very good insulator and its conductance can be ignored. Two samples from the same CNS deposition experiment were measured. Because the four probes make contact at the four corners of the sample, as shown in Figure 2.12 (b), the current is mostly conducted through the base layer, not the vertically oriented nanosheets.

Since the thickness of the nanosheet base layer is unknown, the sheet resistance, rather than the resistivity, was measured, using probe currents ranging from 1×10^{-6} A to 1×10^{-2} A. Figure 5.13 shows the measured sheet resistance *vs.* the probe current for multiple runs of the two samples. At lower current levels, the reproducibility is not good, and the measured sheet resistance values are scattered, because of the relatively high level of noise at low probe currents. However, when the current is greater than 3×10^{-5} A, the curves flatten out and overlap with each other for both samples. Therefore, we calculated the sheet resistance by averaging the values for probe current from 1×10^{-4} A to 1×10^{-2} A.

The average sheet resistances for the two samples are 42.1 Ω/square and 40.0 Ω/square, respectively. The resistivity of graphite along the basal plane is 5×10^{-5} Ω·cm.[5] Using the relationship $\rho = R_{square} \cdot d$, where ρ, R_{square}, and d are the resistivity, sheet resistance, and thickness of the film, we determined the nominal thickness for the two nanosheet samples is 11.9 nm and 12.5 nm. The direct observation of the base-layer

Reproduced with permission of the copyright owner. Further reproduction prohibited without permission.

thickness for CNS on the quartz substrates was difficult since the quartz pieces were hard to cleave and were also non-conductive. However, the calculated base-layer thickness is consistent with the cross-section SEM observations of typical CNS on Si substrates, which will be discussed in next section. This indicates that the base-layer has a resistivity close to that of graphite.

5.2.9 BET surface area of typical CNS

The atomic scale thickness of CNS as observed under SEM and TEM indicates a high surface area, which is confirmed by Brunauer-Emmett-Teller (BET) surface area measurements.

In our study, we measured the net mass of CNS by weighing the substrates before and after CNS depositions using an electronic balance (Ohaus AP250D) with a 0.02 mg standard deviation. The values used for CNS specific area calculations are based on the average of multiple measurements of the samples deposited on 3×3 cm^2 Si substrates.

The net surface area of the CNS was obtained by subtracting the measured surface area of the blanket Si substrates from that of the CNS coated samples. Before measuring, CNS coated Si samples were first purged overnight with ultra-high purity nitrogen gas at 300 °C.

The specific area to be measured was defined as

$$A = \frac{a}{m} \qquad \text{(Eq. 5.1)}$$

where a and m are the measured values of the net area, and the mass of the CNS deposited on the Si substrates. The error of the specific area is then

Reproduced with permission of the copyright owner. Further reproduction prohibited without permission.

$$\Delta A = \left|\frac{\partial A}{\partial a}\right|\Delta a + \left|\frac{\partial a}{\partial m}\right|\Delta m = \frac{1}{m}\Delta a + \frac{a}{m^2}\Delta m \qquad \text{(Eq. 5.2)}$$

where Δa and Δm are the errors for a and m measurements. The specific surface area of CNS is then

$$A = \frac{a}{m} \pm \Delta A = \frac{a}{m} \pm \left(\frac{1}{m}\Delta a + \frac{a}{m^2}\Delta m\right) \qquad \text{(Eq. 5.3)}$$

The measured values for the surface area of CNS on Si substrates are 0.2753 ± 0.0114 m^2, and 0.0798 ± 0.0017 m^2 for blanket substrates, so the net surface area of CNS is $a = 0.1955 \pm 0.0131$ m^2. The net mass of CNS, m, measures 0.18 ± 0.02 mg. Putting these values into Eq. 5.3, we determined the specific surface area of typical CNS: $A = 1086 \pm 194$ (m^2/g).

Table 5.1 lists the surface area of typical carbon nanosheets, the surface area of commercially available activated charcoals, and the theoretical surface area of single-, double-, and triple-layered graphite sheets. Furthermore, the surface area of typical CNS lies between the values for double- and triple-layered graphite sheets, indicating an average CNS thickness of 2-3 atomic layers. This surface area is comparable to the best activated charcoals, and high enough to be useful for practical purposes, such as gas uptake and release, or the production of micro-electrodes.

5.3 Parametric study of carbon nanosheet growth

Previous sections presented the morphology, structure, and properties of CNS deposited under typical conditions. We also investigated how the variation of these parameters affects the growth of CNS. This section will discuss how variations in the substrate temperature, CH_4 concentration, input RF power, and total gas pressure yield different

Reproduced with permission of the copyright owner. Further reproduction prohibited without permission.

CNS. When varying a specific parameter, all other parameters were held constant at their typical values.

Before the discussion of the effects of the growth parameters, we present the results about a series of short duration CNS depositions, ranging from 30 seconds to 8 minutes, under typical CNS growth conditions, i.e. 680 °C substrate temperature, 40% CH_4 in H_2 concentration, 1000 W input RF power, and 100 mTorr total gas pressure. This is helpful to elucidate the nature of the early stages of CNS growth. SEM observations indicated that there is a 2-4 minute latency time before the onset of the vertical nanosheet growth. No features were observed for substrates deposited for 30 seconds and 60 seconds (not shown). For substrates deposited for 90 seconds and 2 minutes, as seen in Figure 5.14 (a) and (b), vertically oriented nanosheets started to appear, but the density was extremely low. However, the nanosheet density increased substantially after a deposition of 4 minutes (Figure 5.14 (c)), and full coverage was achieved after 8 minutes (Figure 5.14 (d)).

Figure 5.14 (e) shows nanosheets with the base layer peeled off from the same sample as shown in Figure 5.14 (d). An enlarged image of the area inside the frame in Figure 5.14 (e) is shown in Figure 5.14 (f), which clearly shows that there is a base layer underneath the vertically oriented nanosheets. Similar peeled-off base layers were also observed from substrates deposited for only 90 seconds (Figure 5.14 (a)); and detailed SEM observation analysis indicates that the base layer is usually 1-15 nm in thickness. This is consistent with the results derived from 4-point resistivity measurements, which was presented in Section 5.2.8.

Reproduced with permission of the copyright owner. Further reproduction prohibited without permission.

5.3.1 Substrate temperature

Typical substrate temperature for CNS growth is 680 °C. In our parametric study, we varied the substrate temperature from 600 °C to 950 °C by changing the voltage applied to the resistive heater filament, and therefore the current and total power. The highest temperature is limited by the capability of the heater.

Figure 5.15 shows SEM images of CNS deposited on Si wafers at various substrate temperatures (630-900 °C) for 20 minutes. It is clear that the substrate temperature has a strong effect on CNS growth, as previously reported.[43] At 630 °C (Figure 5.15 (a)), the nanosheet density is very low, indicating that nucleation and growth rates of CNS are slow at low substrate temperatures. In fact, in our parametric study, we found that nanosheets can not grow when the substrate temperature is lower than 600 °C. Furthermore, as the substrate temperature increases, the nanosheet density increases as well. At 655 °C (Figure 5.15 (b)), the nanosheets density is slightly lower than that of typical nanosheets at 680 °C, as seen in Figure 5.15 (c), but the surface morphologies are almost the same. When the substrate temperature was increased to 730 °C (Figure 5.15 (d)) and 780 °C (Figure 5.15 (e)), the morphologies of the nanosheets are similar to that at 680 °C, but the sheet size is smaller. Furthermore, the sheet surface is less smooth as the nanosheets begin to interweave and form larger structures. At 900 °C, as shown in Figure 5.15 (f), the nanosheets are more corrugated and agglomerated than those deposited at lower temperatures. However, the sheet-like feature remains, and the thickness of the nanosheets does not increase with increasing temperature.

CNS growth rate is derived by dividing the height (observed using cross-section SEM) of a CNS sample by its total growth time. Figure 5.16 (a) illustrates an increasing

Reproduced with permission of the copyright owner. Further reproduction prohibited without permission.

CNS growth rate with increasing substrate temperatures, with a slight drop at the substrate temperature of 900 °C. At higher substrate temperatures, more growth species are supplied, therefore, the growth is faster than at lower substrate temperatures.

Figure 5.16 (b) illustrates the intensity ratio of the D and G peaks, I_D/I_G, in Raman spectrum of CNS at various substrate temperatures. At low temperatures, the I_D/I_G value is lower, indicating a better crystallinity and fewer defects for CNS deposited at low temperatures. The I_D/I_G values increase with higher temperatures, indicating more defective structures. However, for substrate temperatures from 730 °C to 900 °C, the I_D/I_G values are very similar, even though CNS morphologies at these temperatures are quite different, as shown in Figures 5.15 (d), (e), and (f).

Our group also used X-ray diffraction to study the effects of different substrate temperatures on CNS structure.[45] In the asymmetric geometry, when the substrate temperature increased from 670 °C to 950 °C, we observed a decrease of nanosheet crystalline size from 10.7 nm to 5.0 nm. Meanwhile, in the same temperature range, the thickness calculated from X-ray scattering changed from 2.7 nm to 1.9 nm.

5.3.2 Methane concentration

For CNS growth, typical CH_4 concentration in H_2 gas is 40%. In our parametric study, we varied the CH_4 concentration from 10% to 100% (pure CH_4 without H_2) by varying the gas flow rate of CH_4 from 1 sccm to 10 sccm while keeping the total gas flow rate constant at 10 sccm.

Figure 5.17 shows SEM images of CNS deposited on Si substrates using various CH_4 concentrations ranging from 10% to 100%. After viewing these images, it is obvious

Reproduced with permission of the copyright owner. Further reproduction prohibited without permission.

that the CH_4 concentration has a weaker effect on CNS morphology than substrate temperature. All the samples shown in Figure 5.17 have similar corrugated sheet-like features, though the sheet size decreases with increasing CH_4 concentrations, indicating higher nucleation tendency at higher CH_4 concentrations.

Though the morphology change is slight, the growth rate of CNS does increase with an increase in CH_4 concentration, as shown in Figure 5.18 (a). The faster growth rate may occur because of higher growth species concentrations at higher CH_4 concentrations.

The I_D/I_G ratio from Raman spectrum also increases with increasing CH_4 concentrations, as seen in Figure 5.18 (b), indicating more defective structures at higher CH_4 concentrations. This finding is consistent with the morphology observations previously discussed.

5.3.3 Input RF power

Typical CNS were deposited using an input RF power of 900 W. We varied the RF power from 400 W to 1200 W to investigate the effect of RF power on CNS growth. We found that when input RF power changed, the match-network needed to be tuned in order to reach a minimum reflected power. When the RF power is lower than 400 W, inductively coupled plasma is almost impossible to generate, therefore 400 W was our lowest RF power. The highest power, 1200 W, is the maximum output power of our RF power supply. All other parameters were kept constant at their typical values.

Figure 5.19 shows CNS deposited at different RF powers on Si wafers. The morphology of the CNS clearly changed with the RF power, especially at the lower end. At the maximum RF power, 1200 W, (Figure 5.19 (e)), the nanosheets have large,

Reproduced with permission of the copyright owner. Further reproduction prohibited without permission.

smooth, and flat surfaces, and the sheet size is over 1 μm. At 800W (Figure 5.19 (c)), the nanosheets have a similar morphology as the CNS deposited at 1000 W (Figure 5.19 (d)). When the RF power was further decreased to 500 W (Figure 5.19 (b)) and 400 W (Figure 5.19 (a)), the CNS maintained their sheet-like structures, but, were crumpled and smaller in size. The CNS deposited at 400 W RF power were charged during the SEM observation, indicating a low electric conductivity of the CNS.

In Figure 5.20, the growth rate and Raman I_D/I_G ratio were plotted as functions of the input RF power. CNS grow faster at higher input RF powers, meanwhile the I_D/I_G ratio is lower, indicating larger crystalline size and fewer defects of CNS deposited at higher RF powers.

5.3.4 Total gas pressure

Total gas pressure is one of the parameters that determine the plasma discharging mode, as discussed in section 3.3.2. The typical total gas pressure for CNS deposition was 100 mTorr. Pressures higher than 100 mTorr were achieved by adjusting the pumping valve and thus, the vacuum conductance. Pressures lower than 100 mTorr were obtained by decreasing the total gas flow rate to 5 sccm. When the total gas pressure was higher than 400 mTorr, the inductive plasma either could not be generated, or it would shrink in size to a region close to the quartz window underneath the antenna.

Figure 5.21 shows SEM images of CNS deposited on Si substrates at different total gas pressures, ranging from 25 mTorr to 400 mTorr. At pressures of 25 mTorr (Figure 5.21 (a)), and 50 mTorr (Figure 5.21 (b)), the nanosheets are more crumpled and smaller in size than those deposited at 100 mTorr (Figure 5.21 (c)), However, the sheet

Reproduced with permission of the copyright owner. Further reproduction prohibited without permission.

thickness (as observed by higher magnification SEM) is the same. CNS deposited at 200 mTorr (Figure 5.21 (d)), are similar to those deposited at 100 mTorr. However, when the pressure was increased to 300 mTorr (Figure 5.21 (e)) and 400 mTorr (Figure 5.21 (f)), secondary sheets started to form and the thickness increased to 3-5 nm, considerably larger than that of typical CNS.

The growth rate declines with an increase in total gas pressure, as shown in Figure 5.22. The I_D/I_G ratio initially decreased when the pressure increased, indicating that CNS deposited at higher pressures have a better crystallinity and less defects than those deposited at lower pressures. However, as the pressure approaches 300 mTorr and 400 mTorr, the I_D/I_G ratio starts to rise. This might occur because plasma shrinks at higher pressures, therefore the substrates are no longer located in the central region of the plasma and thus there is a lower plasma density at the sample location. This may also lead to the slower growth of CNS at higher pressures.

5.4 Modification and application of carbon nanosheets

In addition to CNS deposited under typical conditions, we obtained parallel arrays of aligned CNS on conductive substrates, and synthesized CNS from C_2H_2 diluted in H_2 and NH_3 gases. This section will also explore potential applications of CNS as catalyst support materials, as well as CNS-based back-gated field emission devices.

5.4.1 Aligned CNS deposition

Our discussion begins with the deposition of parallel arrays of aligned CNS. Here "aligned" means that nanosheets are arranged in a direction parallel to the substrate

Reproduced with permission of the copyright owner. Further reproduction prohibited without permission.

surface, where the two-dimensional sheets form arrays similar to parallel plates. For typical CNS previously discussed, the vertical orientation already aligns the CNS perpendicular to the substrate surface, but top-view observation reveal the sheet distribution to be random.

A schematic of the experimental setup for aligned CNS deposition is shown in Figure 5.23 (a). A tantalum wire ~1 mm in diameter is connected to the chamber wall and grounded at one end. The other end of the Ta wire is placed in contact with a substrate and vertical to the substrate surface. Figure 5.23 (b) is an enlarged top-view schematic of the substrate showing the distribution of the aligned nanosheets on the substrate surface. The region of aligned nanosheets extends 1-2 mm from the wire contact point, and the aligned nanosheets have a radial distribution with the long axis of the nanosheet aligned towards the Ta wire contact point.

Figure 5.24 shows top-view SEM micrographs of aligned CNS deposited on a doped (0.005 Ω·cm) Si wafer at magnifications of 10k (a) and 100k (b). Compared to the SEM images shown in Figure 5.1(a), the nanosheets in Figure 5.24 are more clearly arranged in a parallel manner, though the nanosheets are not perfectly flat. This bending and curving of the surface is most likely caused by defects in the nanosheet structures.

It is known that the sheath around a grounded electrode placed in plasma may form a strong electric field around the electrode surface, and it is believed that this additional E field is the key for the aligned CNS formation. A more detailed analysis of this hypothesis will be presented in Chapter 6.

5.4.2 CNS from other gas compositions

Reproduced with permission of the copyright owner. Further reproduction prohibited without permission.

Previous results are all about CNS deposited from CH_4 in H_2. However, other gas mixtures, such as C_2H_2 in H_2 and C_2H_2 in NH_3, were also used to obtain sheet-like carbon nanostructures. The resulting depositions are discussed in this section.

Figure 5.25 illustrates CNS deposition using 10% to 100 % C_2H_2 in a H_2 mixture (10 sccm total gas flow rate) at a pressure of ~100 mTorr, an input RF power of 900 W, and a substrate temperature of ~700 °C. At lower C_2H_2 concentrations, *i.e.* 10% to 40%, the depositions maintain their sheet-like morphology, as seen in Figure 5.25 (a)-(c), but the sheets are crumpled and corrugated, similar to nanosheets deposited from CH_4 at higher substrate temperatures. However, when the C_2H_2 concentration increases to 80% (Figures 5.25 (d) and (e)), the structures began to agglomerate. When 100% C_2H_2 (Figure 5.25 (f)) is used, no sheet-like structure is observed; only big chunks of amorphous carbon were formed.

Carbon nanosheets were also deposited using C_2H_2 in an NH_3 gas mixture.[33] This gas mixture is typically used for carbon nanotube growth, as discussed in Chapter 4. Si wafers with patterned Ni dots were used as substrates. Figure 5.26 shows the SEM images of nanosheets deposited for 5 minutes in inductively coupled plasmas of various concentrations of C_2H_2 in NH_3 with a constant total gas flow rate of 10 sccm, a pressure of ~100 mTorr, and an input RF power of 900 W. Figure 5.26 (a) indicates that the nanosheet nucleation density was extremely low at 40% C_2H_2, because only a couple of nanosheets nucleated. At 60% C_2H_2, the nucleation density increased, as seen in Figure 5.26 (b), and the nanosheets grew around the Ni dots. At 80% C_2H_2 (Figure 5.26 (c)), sheet-like structures were formed, although not as flat and smooth as typical nanosheets produced with CH_4 in H_2.

Reproduced with permission of the copyright owner. Further reproduction prohibited without permission.

5.4.3 Metal coating on CNS for catalyst support

Since carbon nanosheets have high specific surface areas, they may have potential applications as gas storage or catalyst support materials in fuel cells. Here we present some preliminary results of using CNS for catalyst support.

After a 2-nm layer of platinum or nickel is evaporated on as-deposited CNS, the CNS prevent the metal layer from coalescing into big islands, and stabilize metal particles 3-5 nm in diameter. Figures 5.27 (a) and (b) are SEM images of CNS coated with Pt and Ni thin films, respectively. Rough surfaces with small metal particles on the surface of the CNS are clearly observed. Similar images are also observed on CNS coated with Zr, Hf, Nb, and Ta.

Figure 5.27 (c) presents a TEM micrograph showing Pt particles (dark dots) uniformly distributed over an individual nanosheet grown directly on a TEM grid. The high resolution TEM micrograph shown in Figure 5.27 (d) reveals that the diameter of the Pt particles is in the range of 3-5 nm, making them ideal for fuel cell applications. In fuel cells, chemical reactions only take place at the surface of the catalyst. Small particles have a high surface to mass ratio, therefore small catalysts can substantially reduce the costs and increase the efficiency of fuel cells.

5.4.4 Preliminary results of CNS-based, back-gated field emission devices

Initial back-gated field emission devices used carbon nanotubes (CNT) as cathode materials. Later, CNS became the cathode material of choice because of their promising

Reproduced with permission of the copyright owner. Further reproduction prohibited without permission.

field emission properties, robustness, and compatibility with the device fabrication process.

An improved "buried-line" configuration of back-gated devices, as shown schematically in Figure 5.28, was recently developed by partners working with our group.[42] The buried-line structure eliminates dielectric breakdowns caused by high electrostatic fields at the sharp edges of the previously used trapezoid cathode lines.

The CNS-based, buried line back-gated field emission device fabrication process starts with n-type (As dope) Si wafers with 1 μm thermal oxide. The cathode pattern is then developed utilizing a positive photo-resist. An isotropic etch forms trenches 0.5 μm deep, where a thin Cr/Au layer is evaporated. The photo-resist is removed, and the trenches are electroplated with Au or Ni, as the cathode metal lines. A blanket layer of typical CNS is then deposited over the entire surface of the wafer, as shown in Figure 5.29 (a). CNS fully cover both the metal line and the underneath SiO_2 surfaces, as shown by the cross-section SEM image of CNS deposited on a trapezoid back-gated device illustrated in Figure 5.29 (b).

After the wafer is patterned, CNS are etched, except on the centers of the cathode lines, and the devices are ready for field emission testing. Figure 5.29 (c) shows CNS centered at the cathode line after the final etch, and Figure 5.29 (d) is a cross-section profile of the nanosheets in a buried-line, back-gated device.

The back-gated devices were tested in triode modes. Before the back-gate voltage was applied, a diode field of 9 V/μm was established between the cathode and the anode, which yielded an emission current of 5 μA. With this diode field fixed, the back-gate voltage was increased and the corresponding I-V curves were measured, as seen in Figure

Reproduced with permission of the copyright owner. Further reproduction prohibited without permission.

5.30. Variations of the individual I-V curves for the 20 ramps are very small. At a back-gate voltage of 180 V for each ramp, the emission current was increased to ~1.33 mA, almost 3 orders of magnitude higher than the value for zero-voltage bias of the gate. This result is consistent with theoretical predictions.

5.5 Summary

We successfully synthesized a two-dimensional carbon nanostructure — carbon nanosheets — by radio frequency plasma enhanced chemical vapor deposition on a variety of substrates without the need for any catalyst.

Typical CNS were deposited in inductively coupled plasma using 40% CH_4 in H_2 atmosphere, at a substrate temperature of 680 °C, a total gas pressure of 100 mTorr, and an input RF power of 900 W. We characterized the morphology, composition, and structure properties of CNS via SEM, TEM, AES, XPS, PIXE, ERDA, TDS, Raman, FTIR, and XRD. The results revealed that CNS have 2-D surface morphologies with atomically thin edges, and are free-standing off the substrate surface. CNS growth is a catalyst-independent process, therefore the CNS are free from metallic impurities. The CNS have defective crystalline graphitic structures with large amounts of H atoms incorporated. CNS have large specific surface area, making them promising candidates for catalyst support materials. Furthermore, CNS have good field emission properties, such as low turn-on field, long lift-times with stable emissions, a high emission current, and a high emission current density.

We investigated how growth parameters, including substrate temperature, CH_4 concentration, input RF power, and total gas pressure, affect the morphology, growth rate,

Reproduced with permission of the copyright owner. Further reproduction prohibited without permission.

and orderliness of the CNS. Carbon nanosheet growth is not possible if the substrate temperature is lower than a critical value. Increasing substrate temperature resulted in a faster growth rate and an increased number of defects. Changing CH_4 concentration did not change CNS morphologies significantly, but higher CH_4 concentration yielded a faster growth rate and more defective CNS. Similarly, lower gas pressure resulted in a faster growth rate and a more defective structure. Higher RF power, however, yielded a faster growth rate and fewer defects in CNS.

Aligned arrays of CNS were obtained in the vicinity of an external grounded electrode on conductive substrates. Carbon nanosheet-like structures were also synthesized in inductively coupled plasma using C_2H_2 in H_2 and NH_3 atmospheres at similar conditions as for typical CH_4/H_2 CNS growth.

Carbon nanosheets may have wide applications in various research fields. Preliminary results indicate that CNS are good candidates for catalyst support material in fuel cell applications. Furthermore, a carbon nanosheet-based, back-gate device was fabricated and tested for triode performance.

Reproduced with permission of the copyright owner. Further reproduction prohibited without permission.

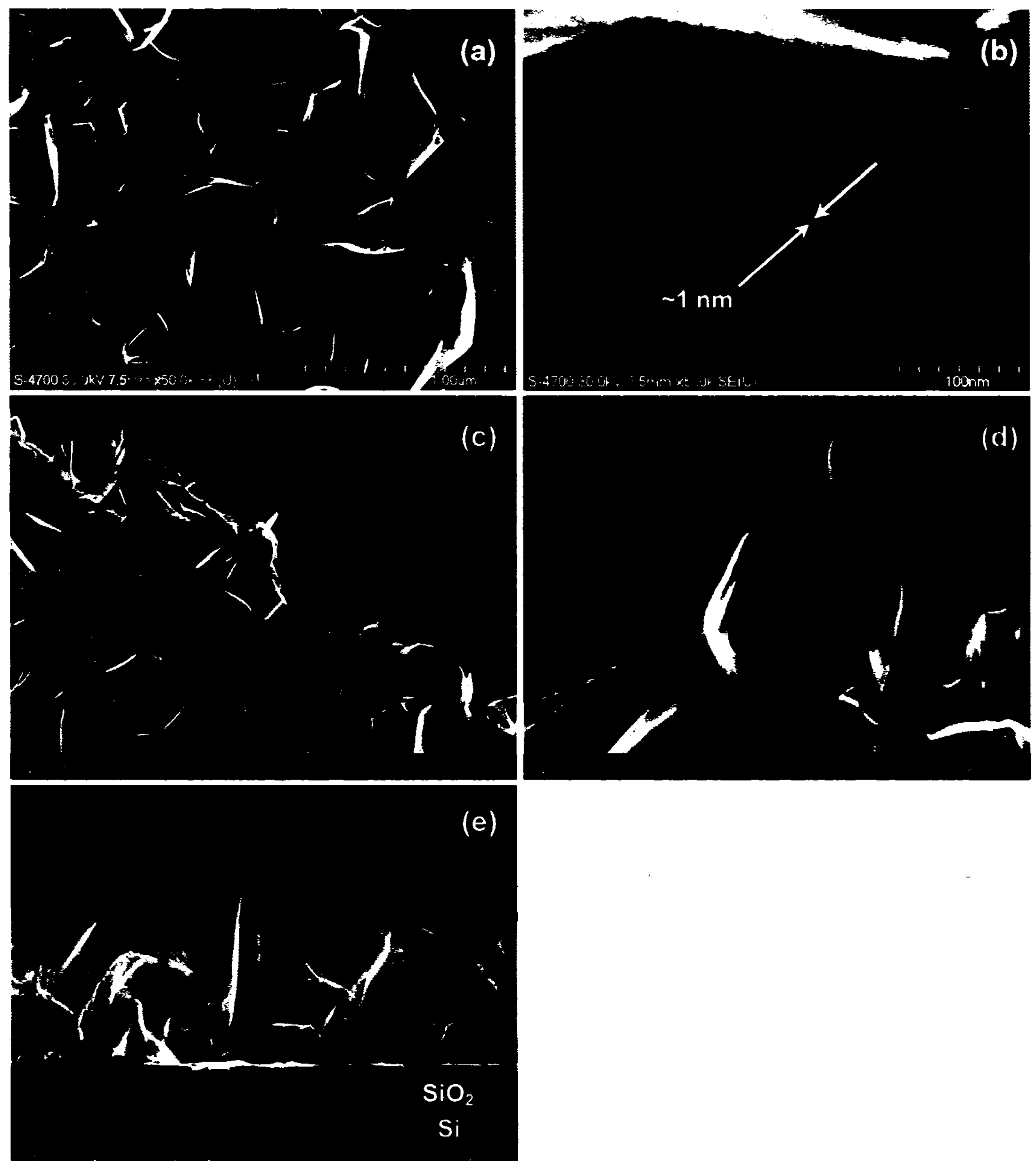

Figure 5.1: Representative SEM images of typical CNS deposited with 40% CH_4 in H_2, at 100 mTorr total gas pressure, 680 °C substrate temperature, and 900 W RF power. (a): Top view image shows the 2-D surface morphology of the CNS. (b): Enlarged image shows the CNS edge is ~1 nm thick. (c): CNS on a curved Ni TEM surface, showing both top and cross-section views. (d): Enlarged image of CNS on curved surface, showing vertical orientation of the CNS. (e): Cross-section view of as-deposited CNS on cleaved SiO_2/Si substrates.

Reproduced with permission of the copyright owner. Further reproduction prohibited without permission.

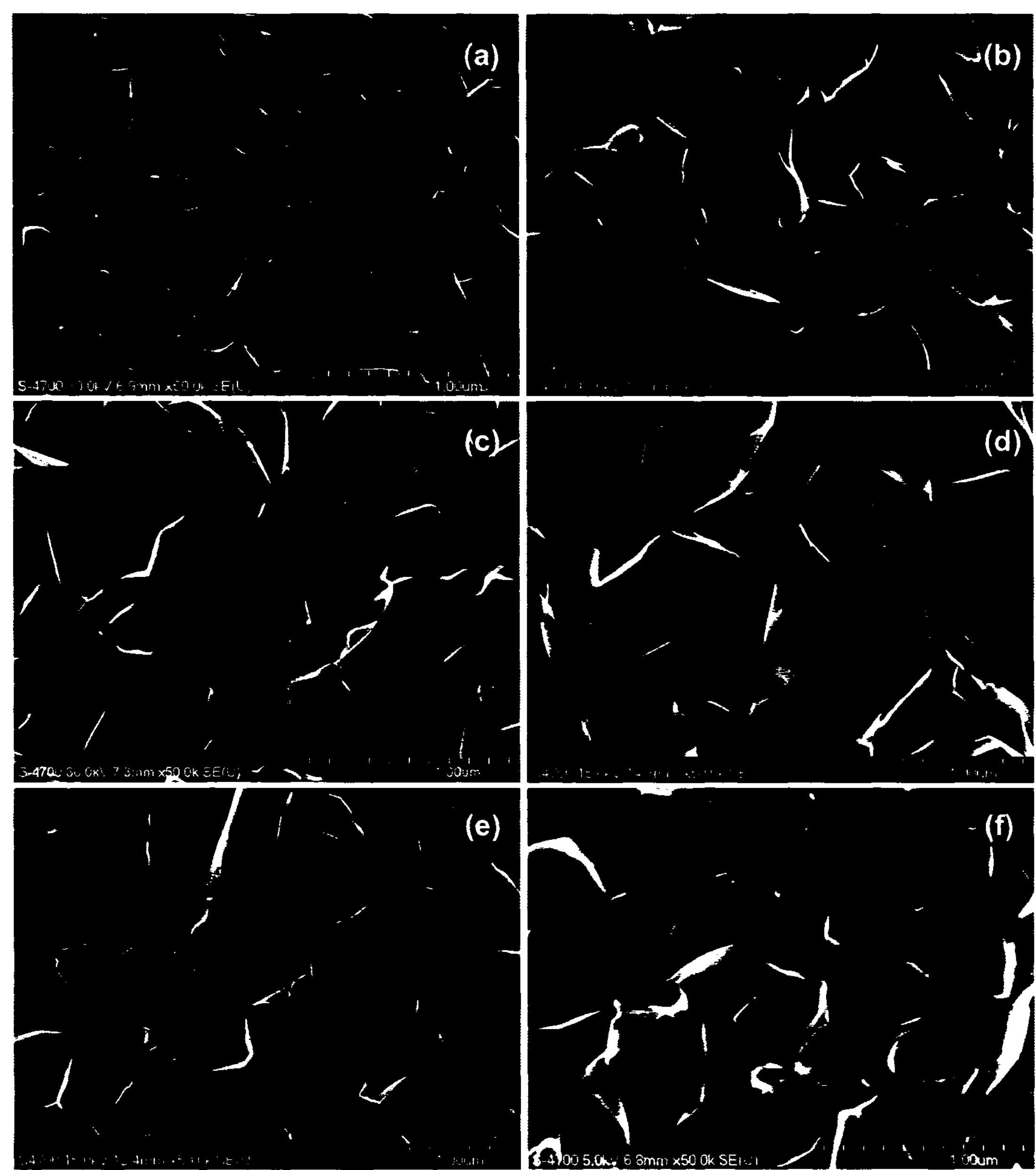

Figure 5.2: SEM images of CNS deposited on (a): Si, (b): graphite, (c): stainless steel, (d): Ta, (e): Quartz (SiO_2), and (f): Al_2O_3 substrates reveal similar surface morphologies, regardless of the substrate material.

Reproduced with permission of the copyright owner. Further reproduction prohibited without permission.

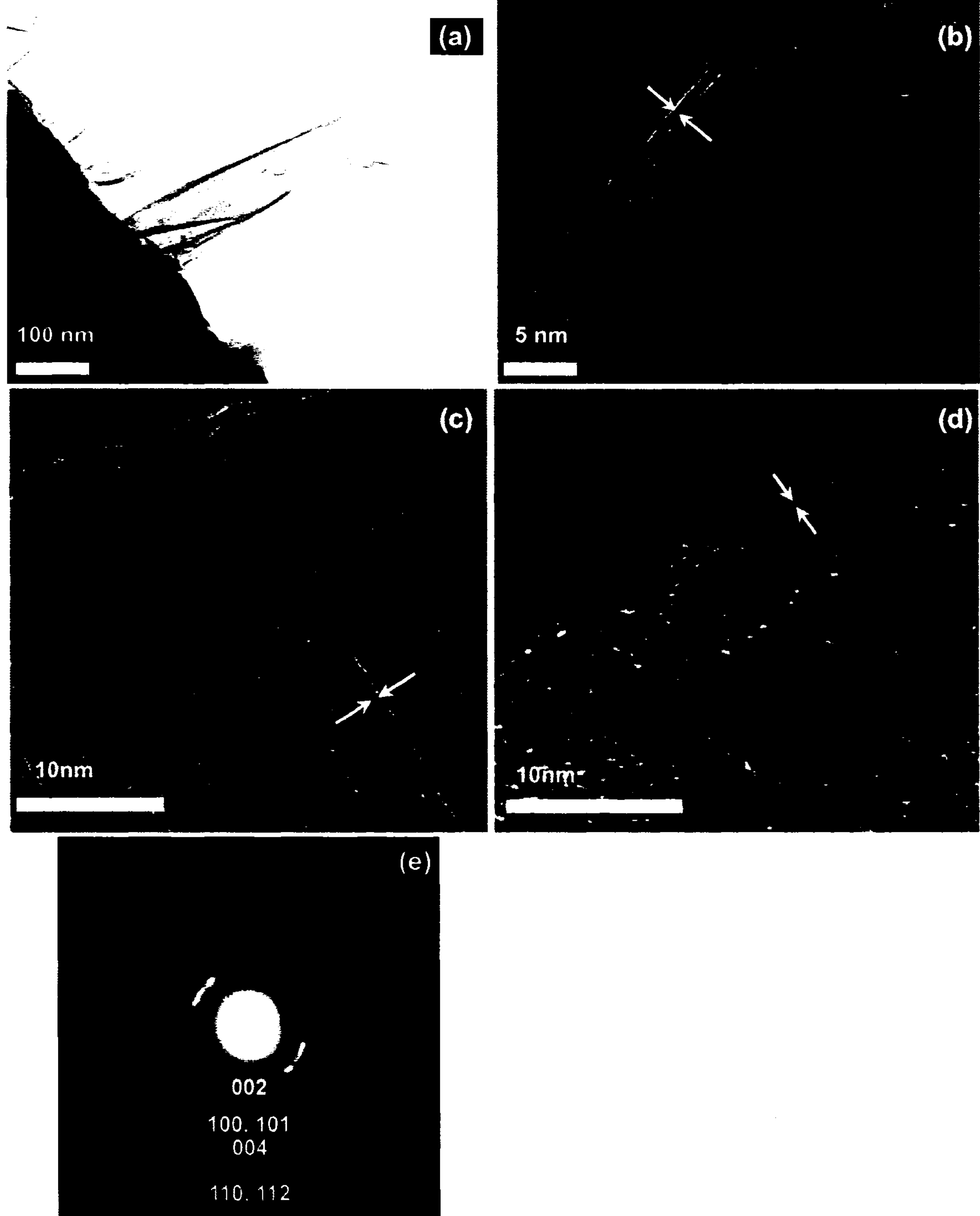

Figure 5.3: (a) TEM image showing CNS grown directly on a grid. (b)-(d) HRTEM of single pieces of nanosheets showing double parallel fringes with a distance 0.34-0.37 nm at the edge of CNS. (e) The electron diffraction pattern of CNS observed in TEM, matches that of a graphitic structure.

Reproduced with permission of the copyright owner. Further reproduction prohibited without permission.

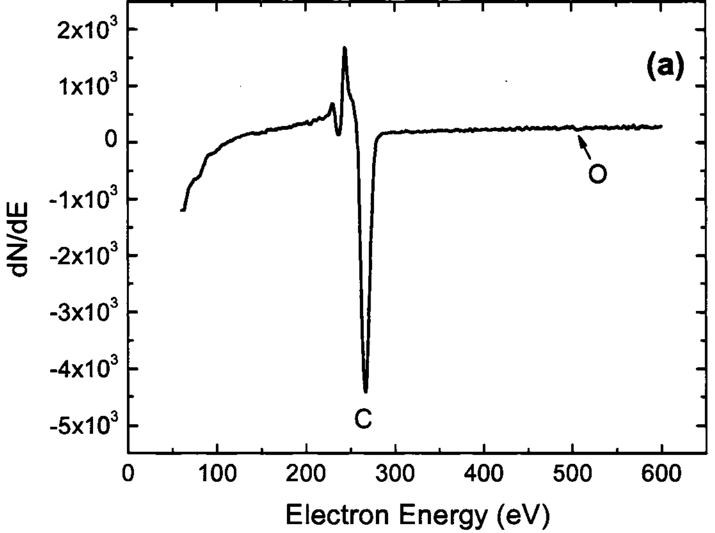

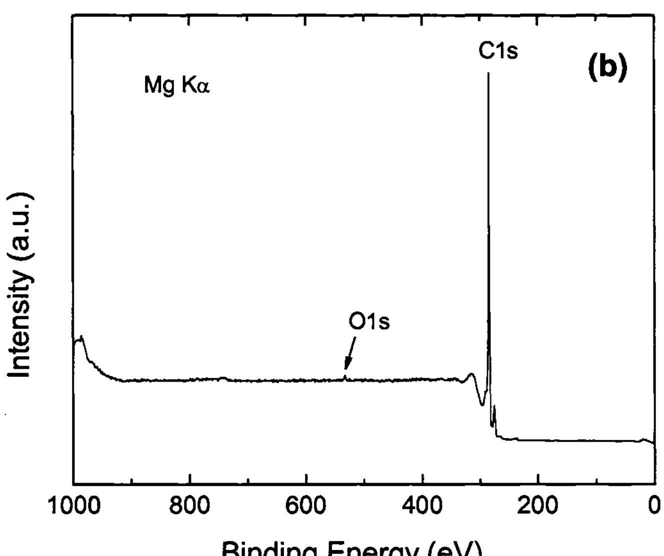

Figure 5.4: AES (a) and XPS (b) spectra of typical CNS samples have only C features, with a negligible amount of O from absorbed water due to ambient exposure.

Reproduced with permission of the copyright owner. Further reproduction prohibited without permission.

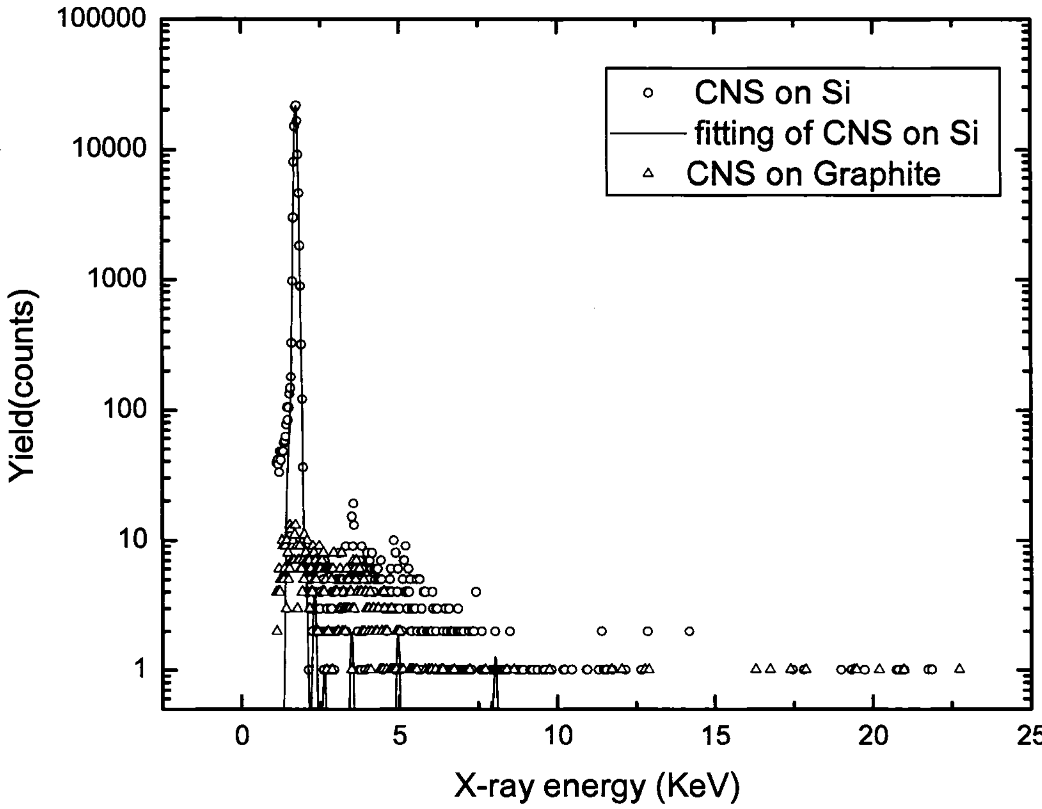

Figure 5.5: PIXE spectra of CNS coated on Si and graphite substrates. The fitted data reveals a Si peak only from CNS on Si substrates. No element is detected for CNS grown on graphite substrates, indicating extremely low contamination concentrations.

Reproduced with permission of the copyright owner. Further reproduction prohibited without permission.

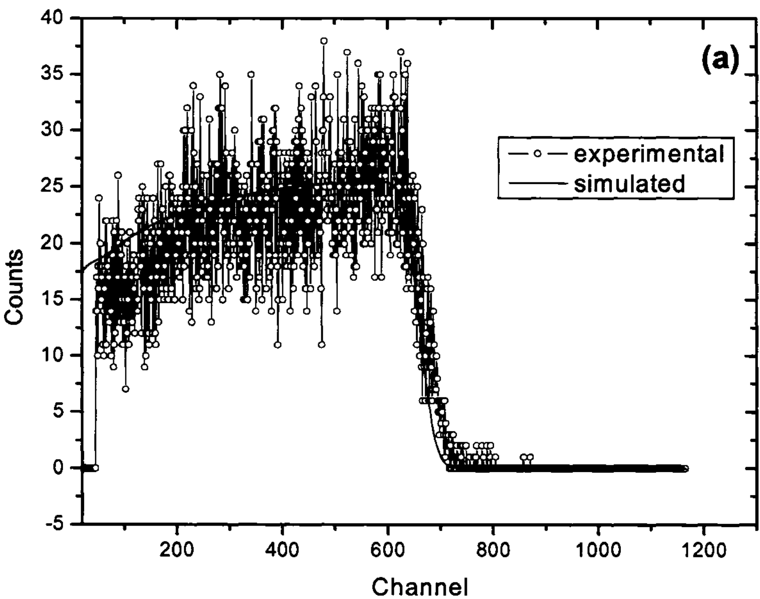

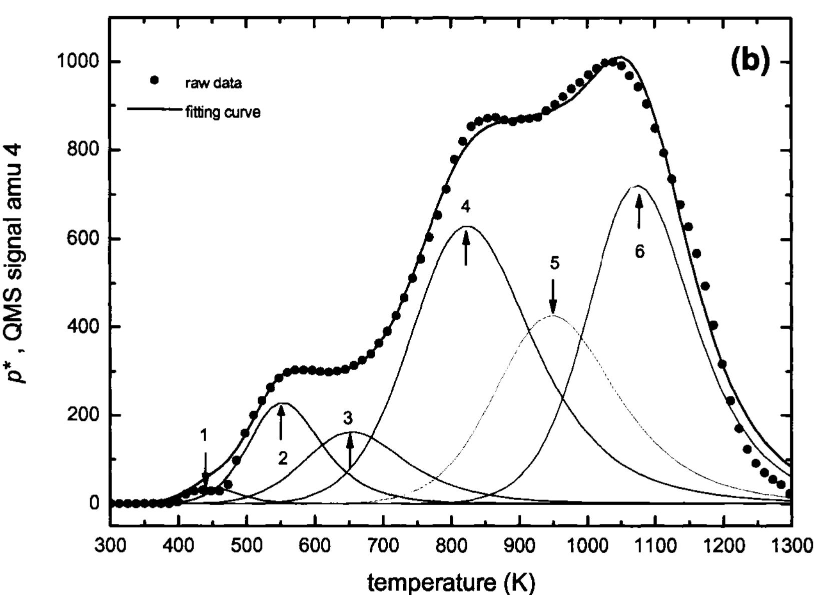

Figure 5.6: Both ERDA (a) and TDS (b) measurements indicate large amounts of H incorporated into CNS.

Reproduced with permission of the copyright owner. Further reproduction prohibited without permission.

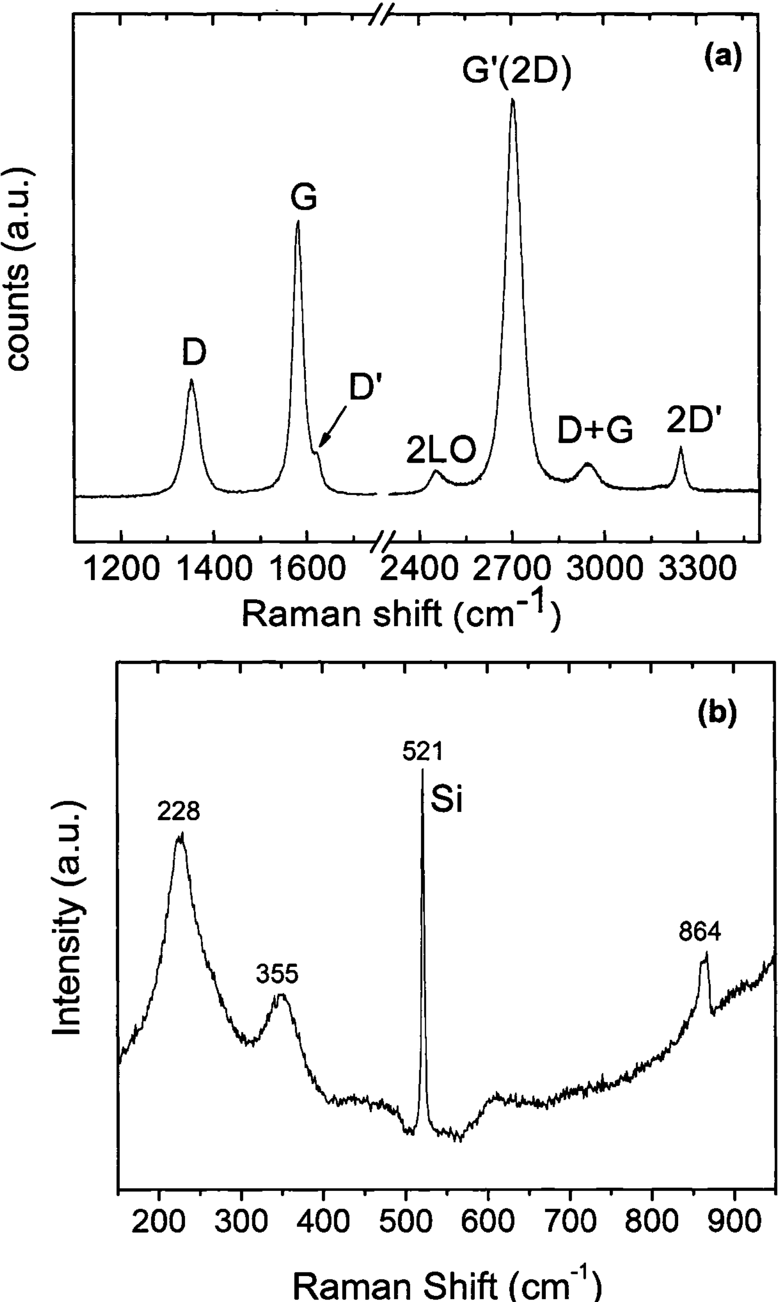

Figure 5.7: (a) Raman spectrum of typical CNS samples using a 514 nm excitation laser wavelength. The first order peaks and second-order over-tunes are labeled. (b) Low energy peaks observed from typical CNS samples using a 633 nm excitation laser wavelength.

Reproduced with permission of the copyright owner. Further reproduction prohibited without permission.

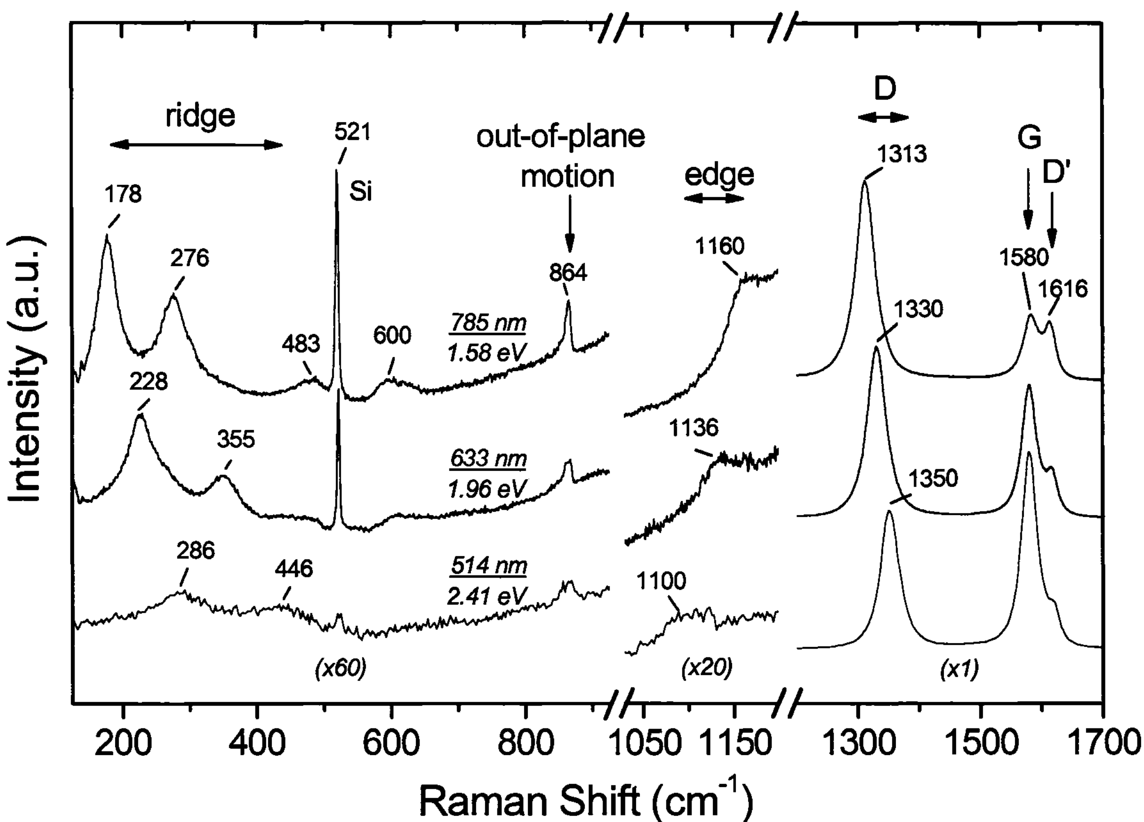

Figure 5.8: Raman spectra of typical CNS excited by three different wavelength lasers. Note how the position and/or the intensity changes with variation in laser energy/ wavelength.

Reproduced with permission of the copyright owner. Further reproduction prohibited without permission.

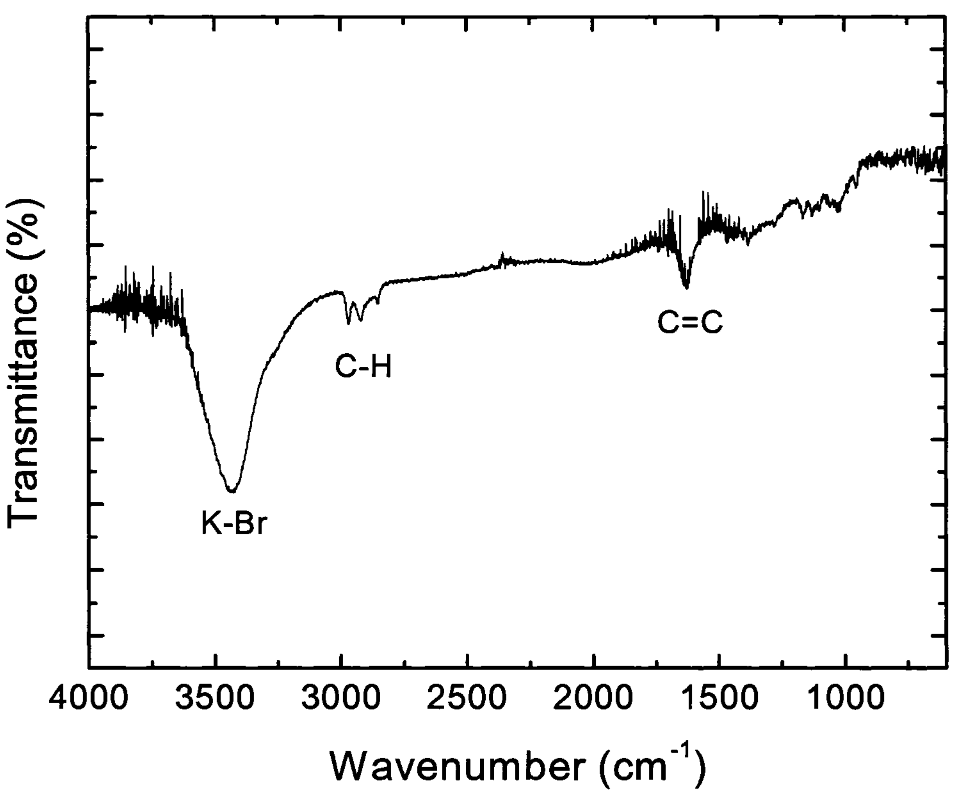

Figure 5.9: Representative absorption FTIR spectrum of typical CNS. The C-H stretching vibrational mode and C=C stretching vibrational mode were observed in the spectrum.

Reproduced with permission of the copyright owner. Further reproduction prohibited without permission.

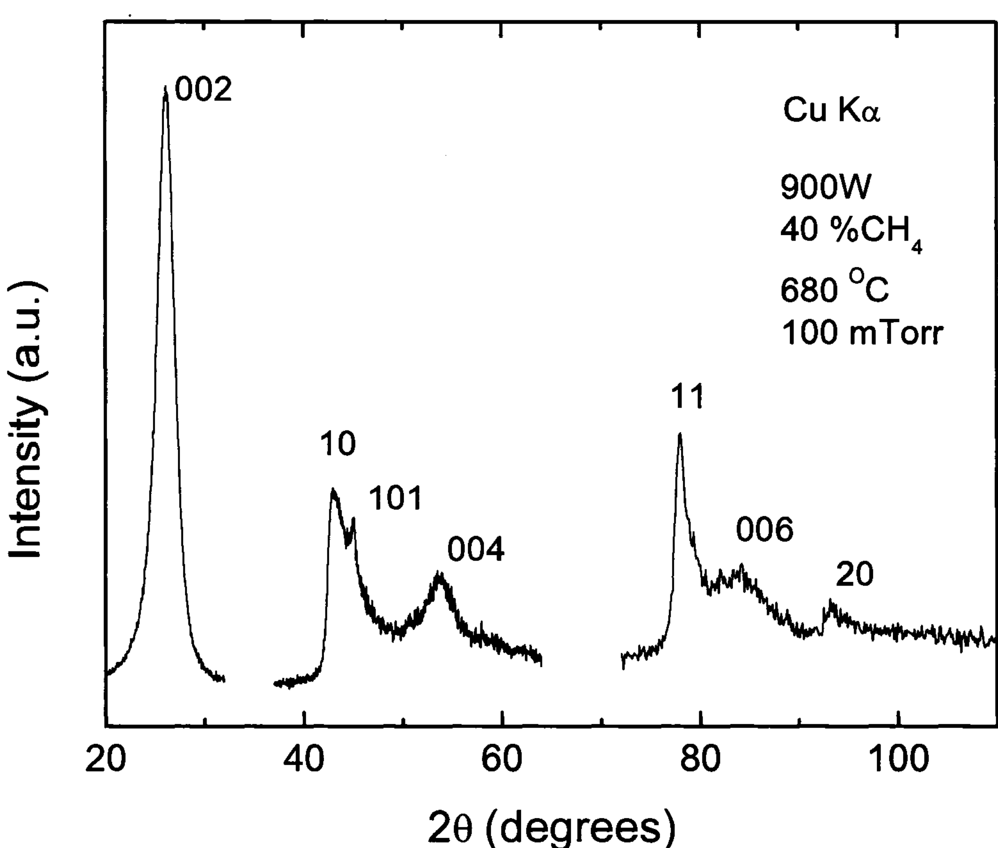

Figure 5.10: Asymmetric glancing angle XRD spectrum of a typical CNS sample. The (101) reflection indicates a crystalline structure.

Reproduced with permission of the copyright owner. Further reproduction prohibited without permission.

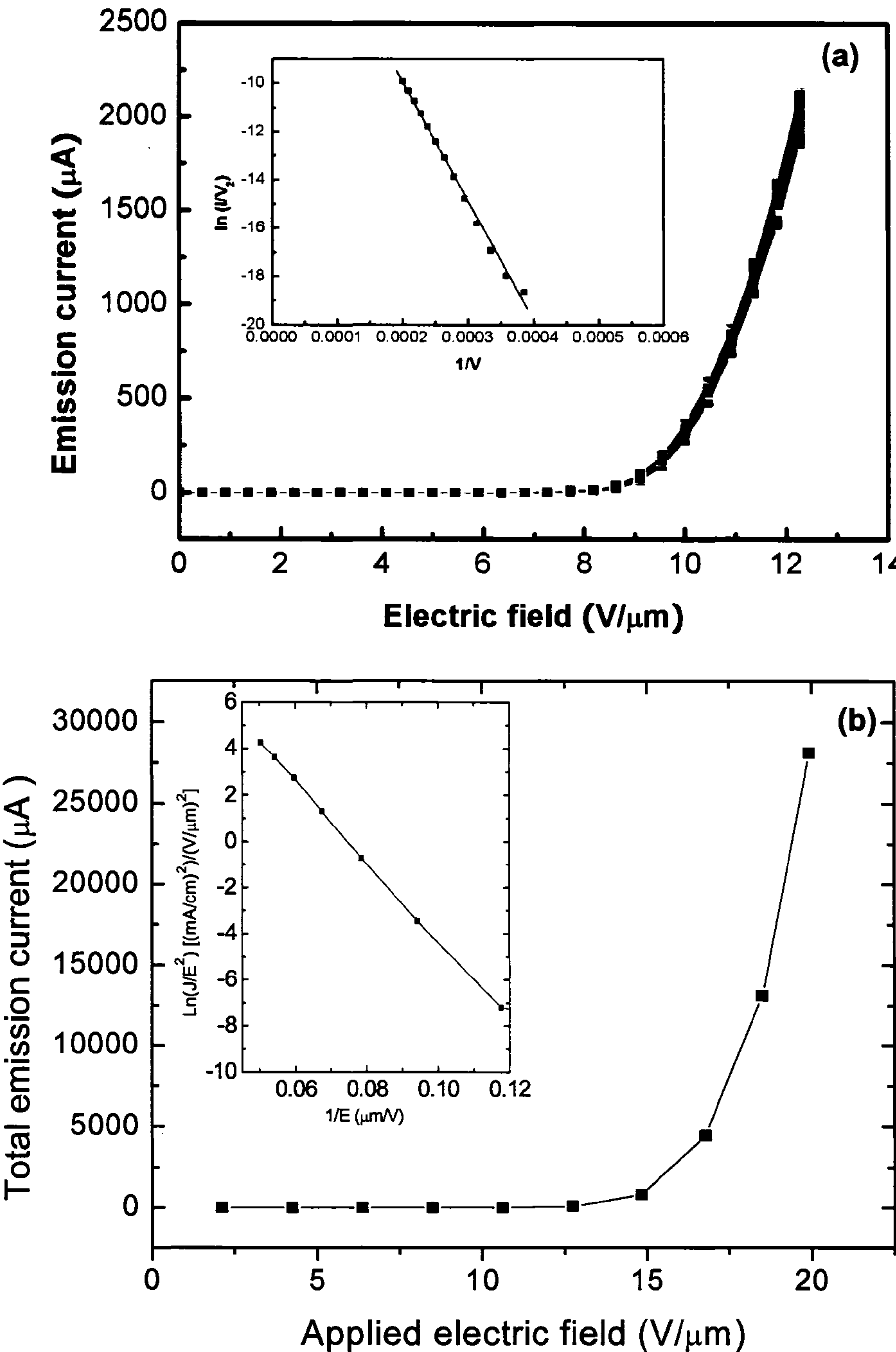

Figure 5.11: Two field emission I-V curves of typical CNS showing (a) a turn-on field of ~7.8 V/μm and (b) a total emission current of 28 mA. The insets illustrate corresponding Fowler-Nordheim plots. The straight lines indicate unsaturated exponential field emission behavior.

Reproduced with permission of the copyright owner. Further reproduction prohibited without permission.

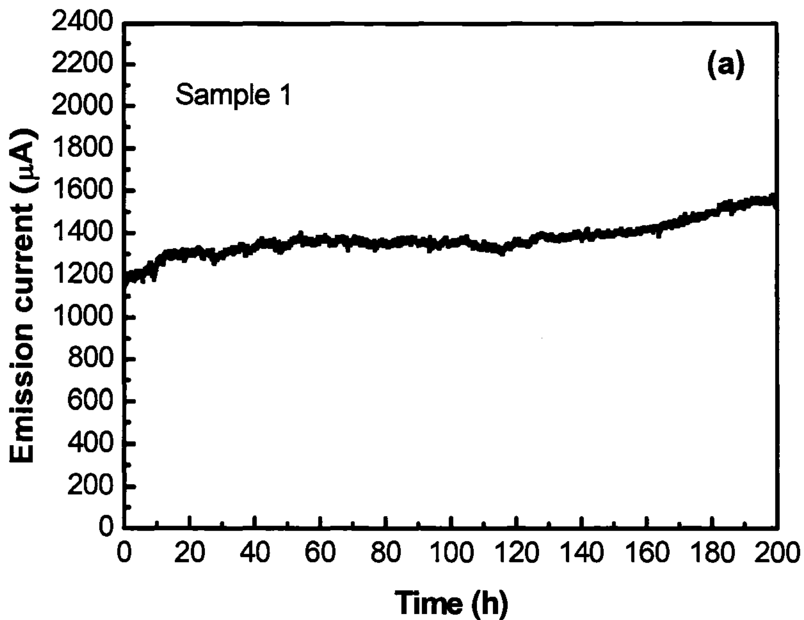

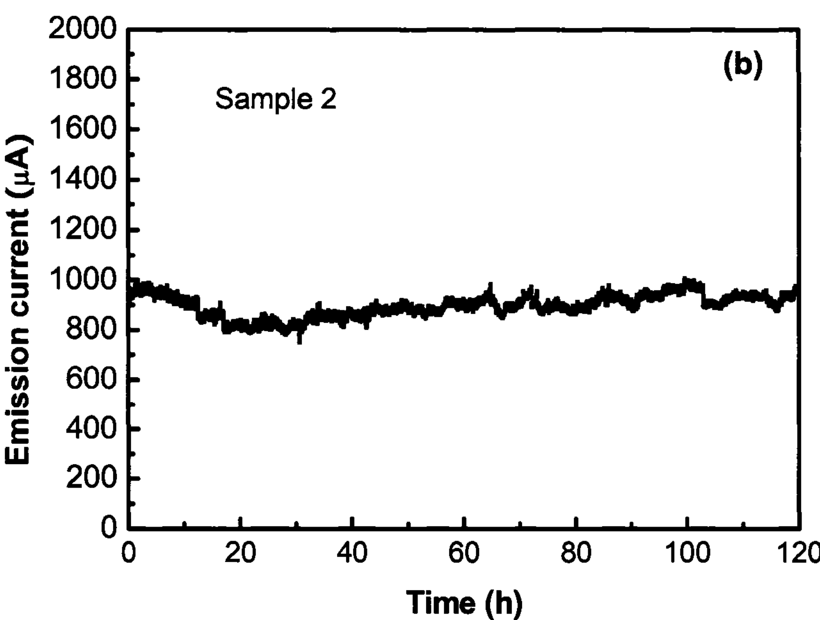

Figure 5.12: The I_{max} *vs.* t curves of two CNS samples showing stable electron emission over (a) 200 hours and (b) 120 hours. No degradation was observed in either sample.

Reproduced with permission of the copyright owner. Further reproduction prohibited without permission.

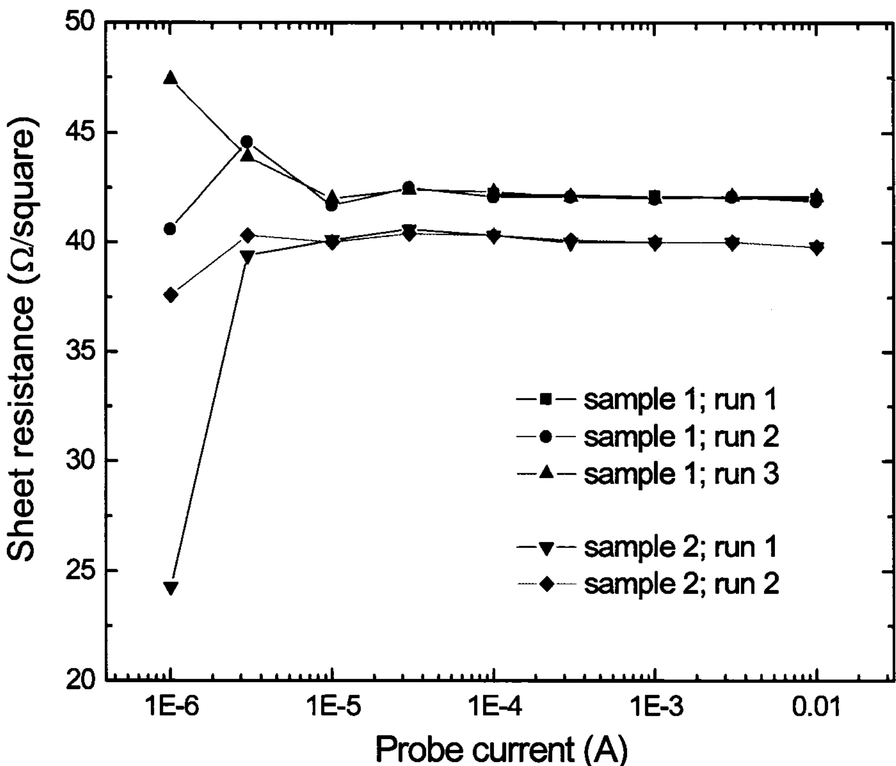

Figure 5.13: Sheet resistance of CNS on quartz substrates measured by a 4-point probe at various probe currents. The measurements are reproducible for probe currents greater than 3×10^{-5} A.

Reproduced with permission of the copyright owner. Further reproduction prohibited without permission.

Table 5.1: Comparison of typical carbon nanosheet surface area of to that of activated charcoal and the theoretical surface areas of single-, double-, and triple-layered graphite sheets.

Materials	**Surface area (m^2/g)**
Typical CNS	**1086**
Activated charcoal	**~1000**
Theoretical single-layer graphite sheets	**2630**
Theoretical double-layer graphite sheets	**1315**
Theoretical triple-layer graphite sheets	**877**

Reproduced with permission of the copyright owner. Further reproduction prohibited without permission.

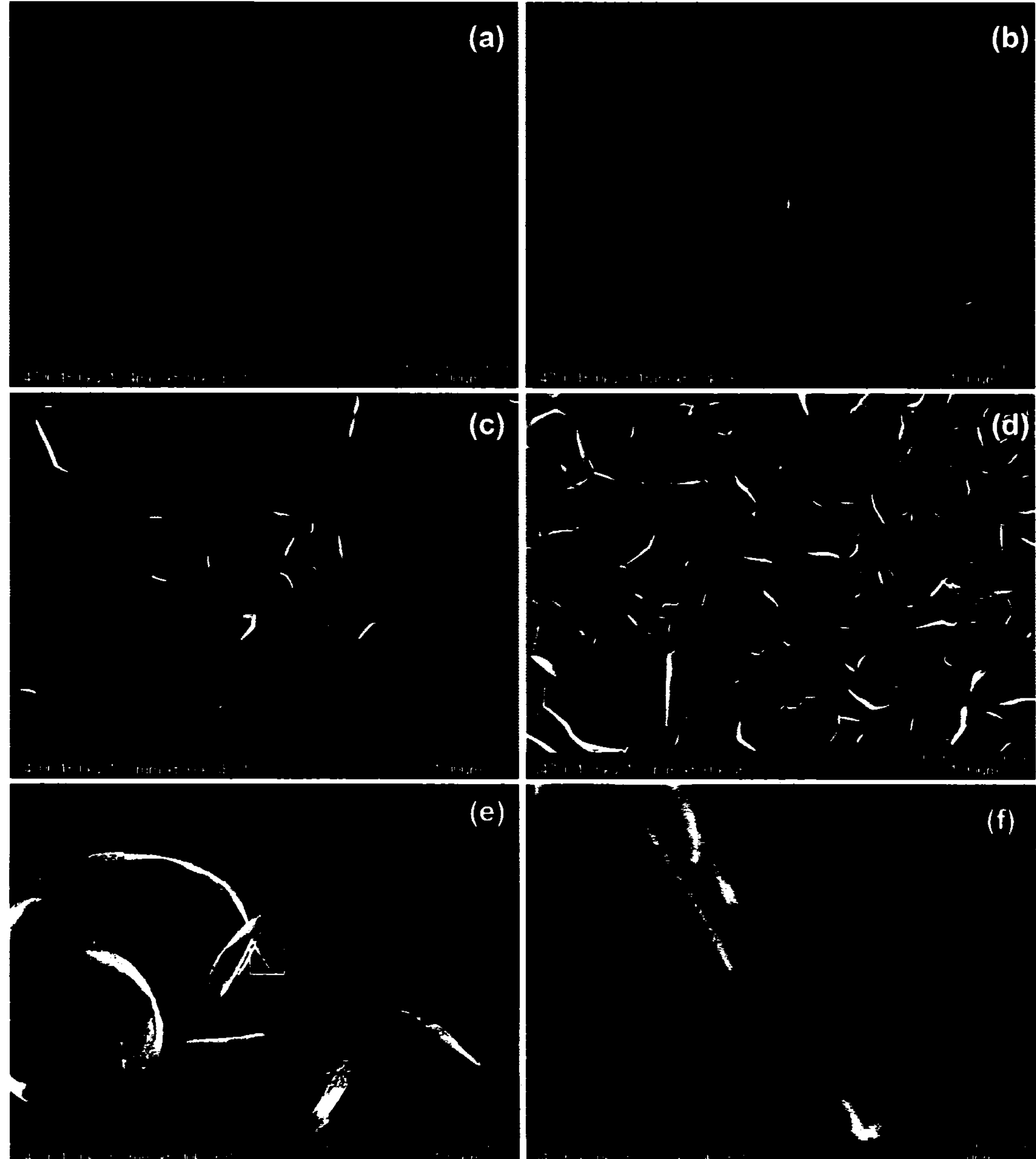

Figure 5.14: SEM images of CNS deposited for (a) 90 sec, (b) 2 min, (c) 4 min, (d) 8 min at 680 °C substrate temperature, 100 mTorr total pressure, and 1000 W input RF power. (e): Peeled-off CNS from the sample shown in (d), and (f): magnified image of the area within the red frame in (e) showing the base layer under the vertically oriented sheets.

Reproduced with permission of the copyright owner. Further reproduction prohibited without permission.

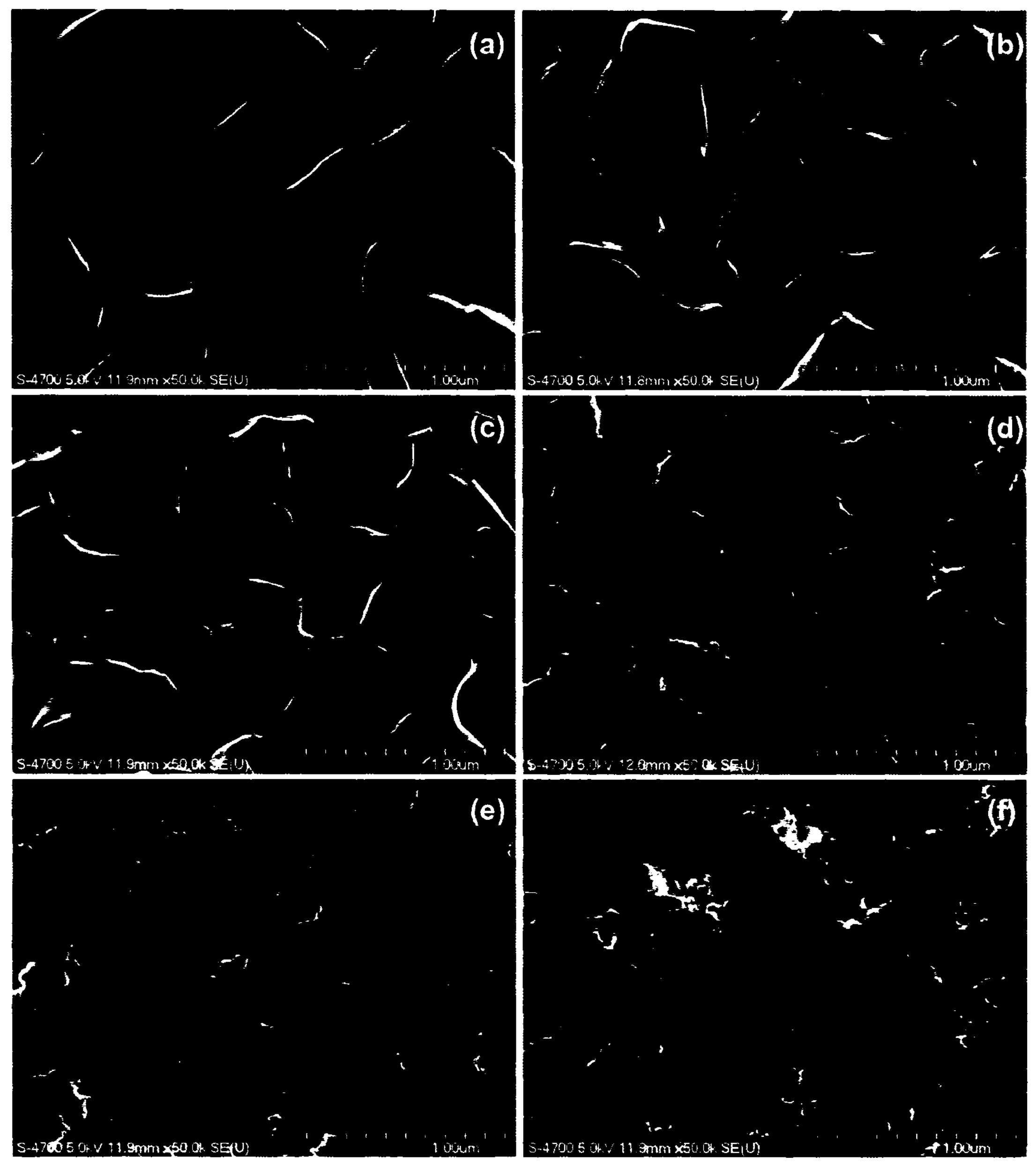

Figure 5.15: SEM images of CNS deposited on Si substrates at various substrate temperatures of (a) 630 °C, (b) 655 °C, (c) 680 °C, (d) 730 °C, (e) 780 °C, and (f) 900 °C.

Reproduced with permission of the copyright owner. Further reproduction prohibited without permission.

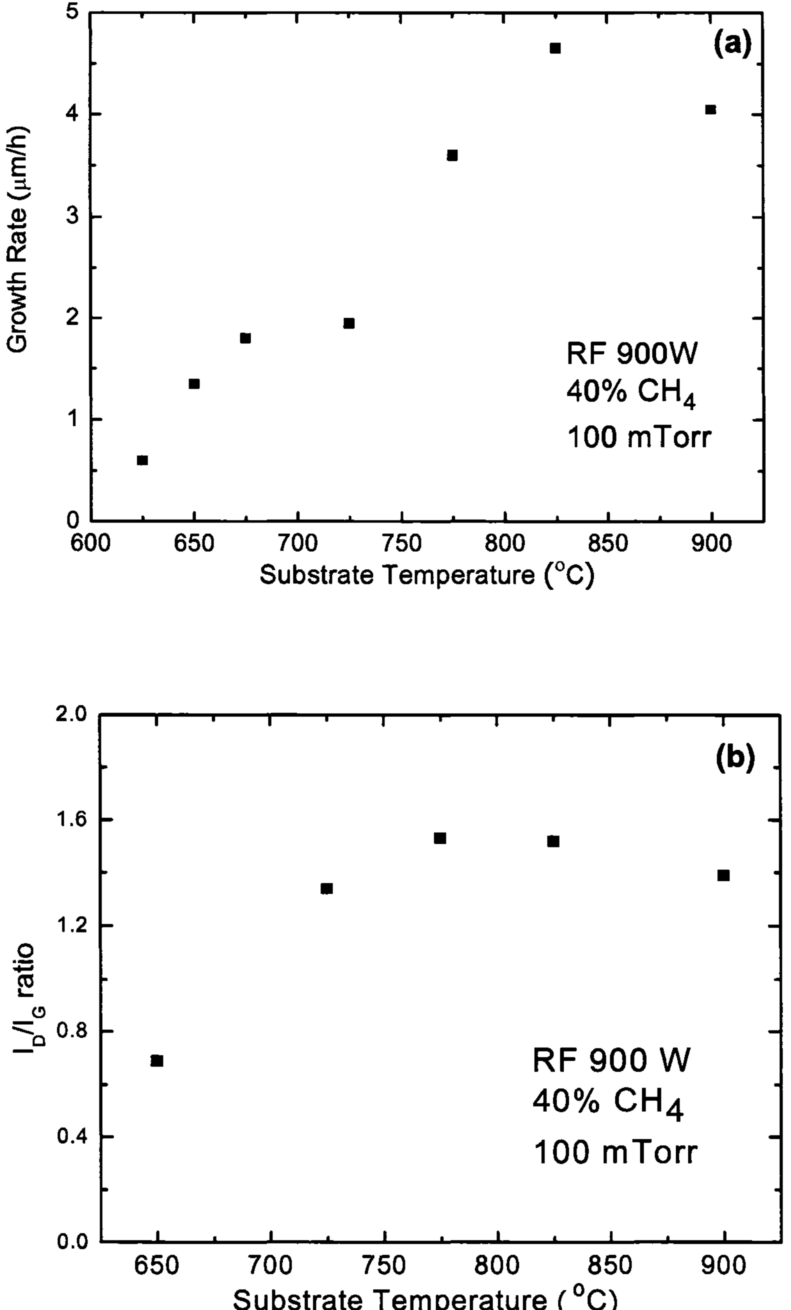

Figure 5.16: (a) the growth rate and (b) the I_D/I_G ratio in Raman spectrum of CNS deposited at various substrate temperatures.

Reproduced with permission of the copyright owner. Further reproduction prohibited without permission.

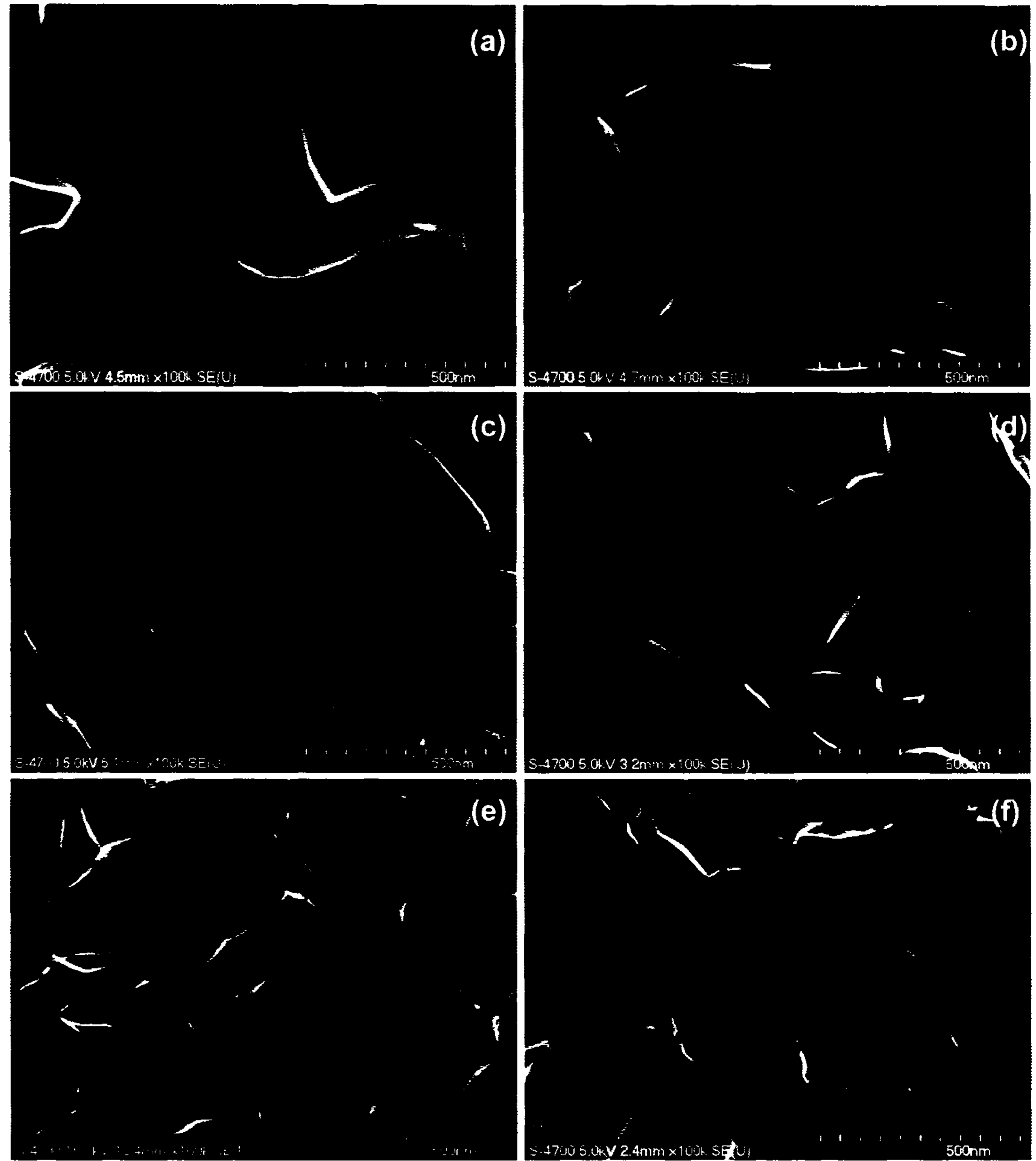

Figure 5.17: SEM images of CNS deposited on Si substrates using (a) 10%, (b) 20%, (c) 40%, (d) 60%, (e) 80%, and (f) 100% CH_4 in H_2.

Reproduced with permission of the copyright owner. Further reproduction prohibited without permission.

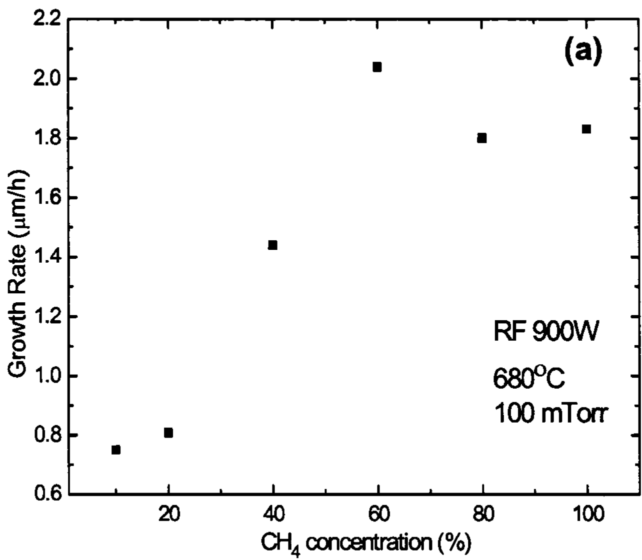

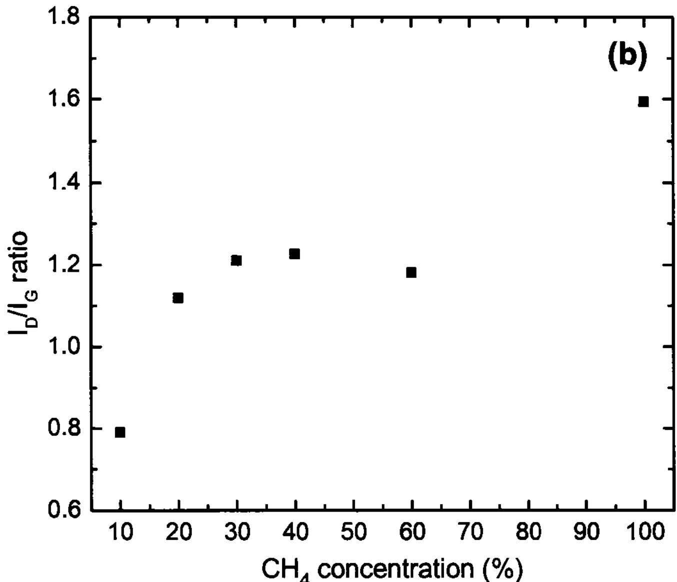

Figure 5.18: (a) the growth rate and (b) the I_D/I_G ratio in Raman spectrum of CNS deposited at various CH_4 in H_2 concentrations.

Reproduced with permission of the copyright owner. Further reproduction prohibited without permission.

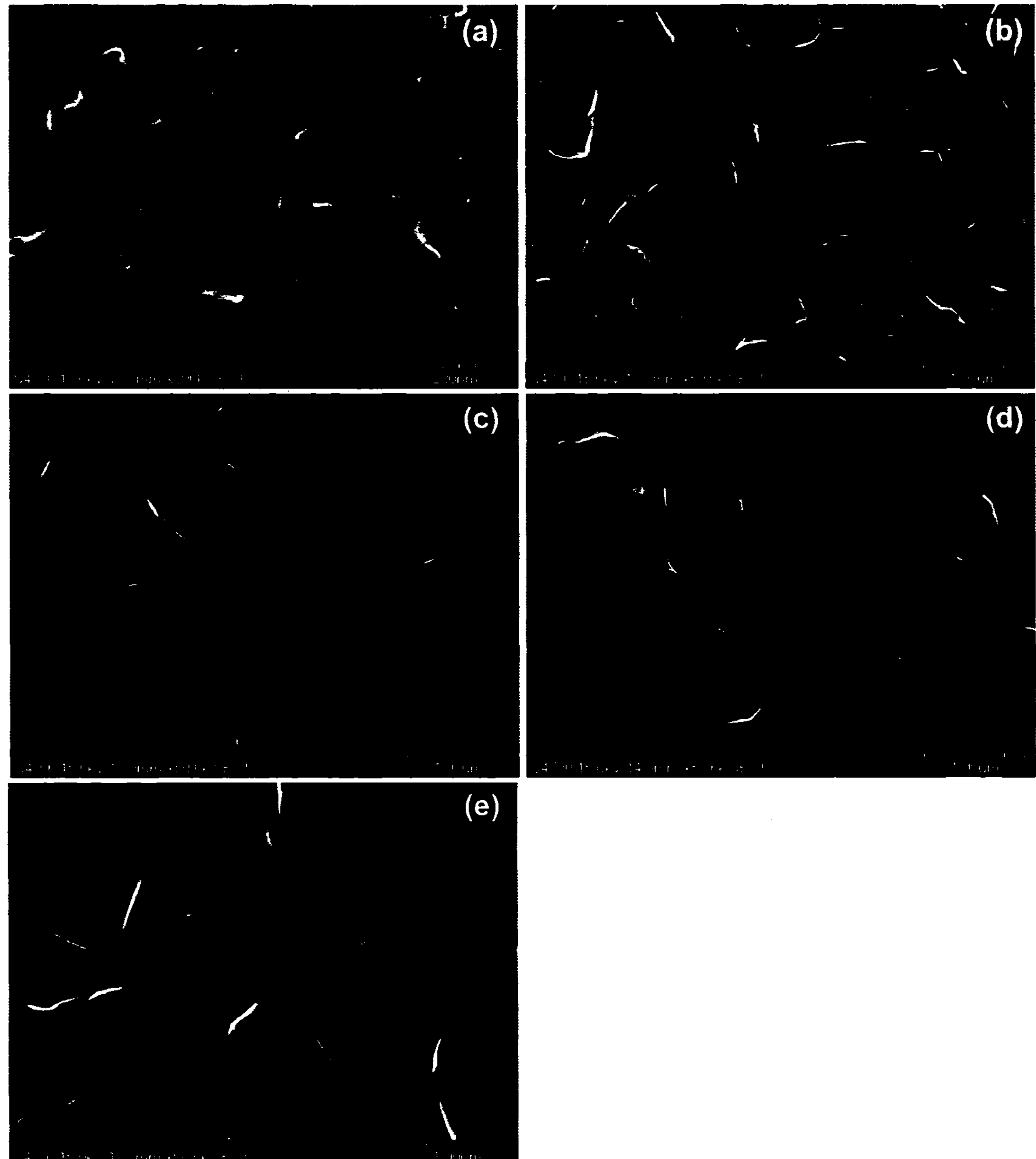

Figure 5.19: SEM images of CNS deposited on Si substrates at input RF powers of (a) 400 W, (b) 500 W, (c) 800 W, (d) 1000 W, and (e) 1200 W.

Reproduced with permission of the copyright owner. Further reproduction prohibited without permission.

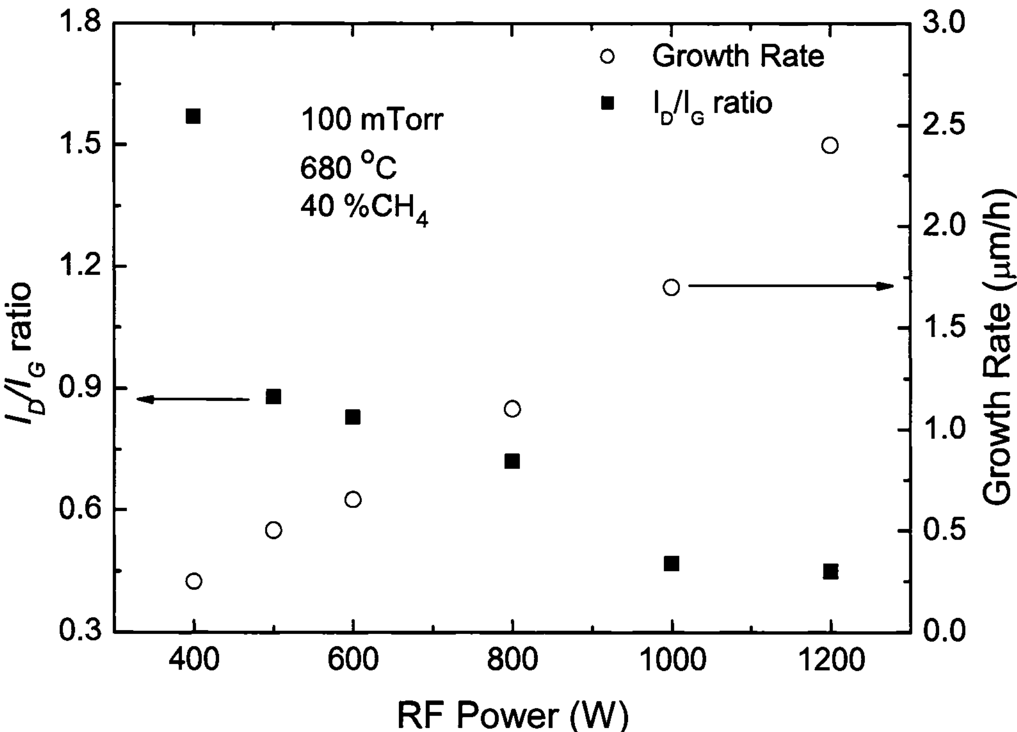

Figure 5.20: The growth rate and the I_D/I_G ratio in Raman spectrum of CNS deposited with different input RF powers.

Reproduced with permission of the copyright owner. Further reproduction prohibited without permission.

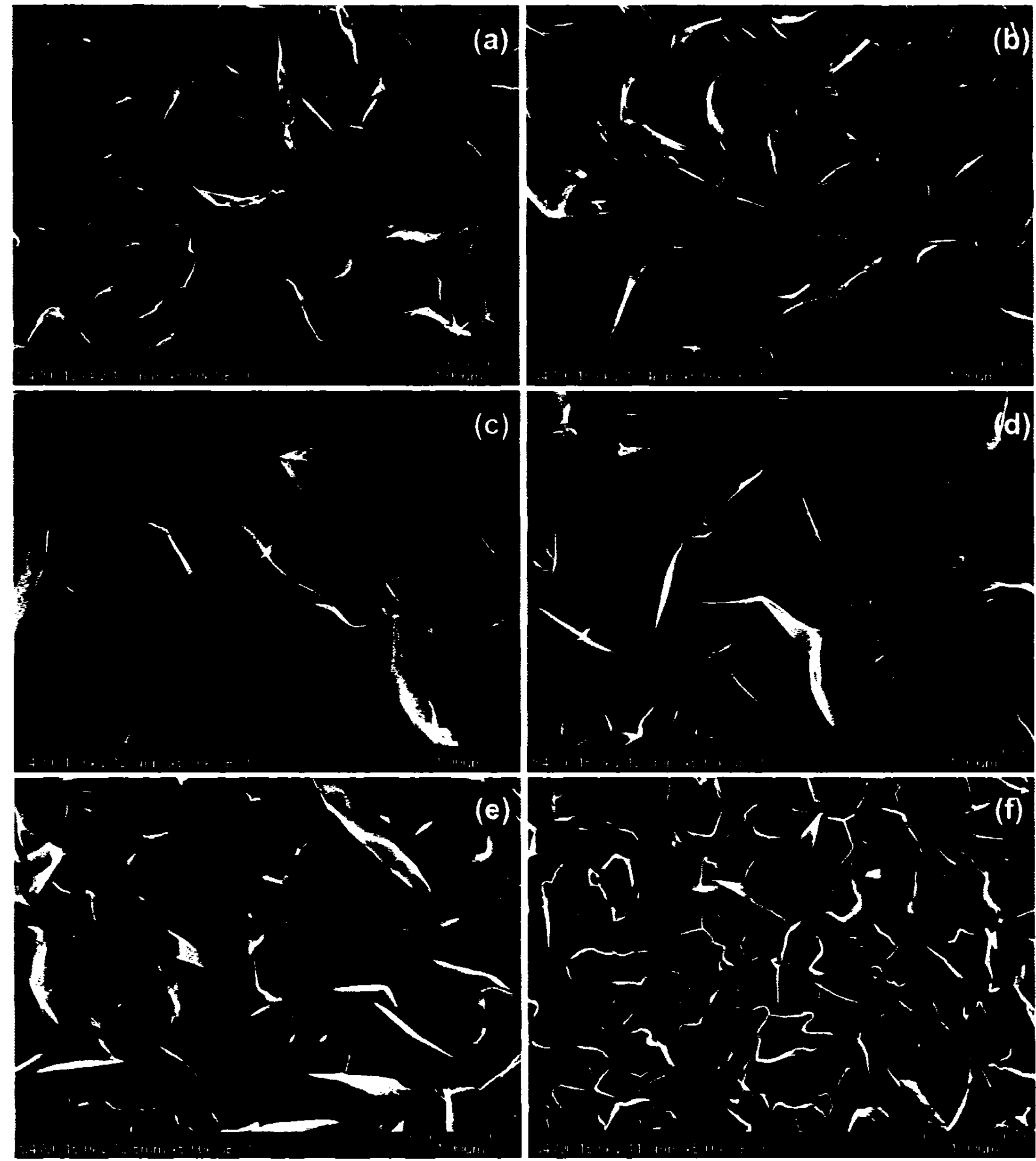

Figure 5.21: SEM images of CNS deposited on Si substrates at total gas pressures of (a) 20 mTorr, (b) 50 mTorr, (c) 100 mTorr, (d) 200 mTorr, (e) 300 mTorr, and (f) 400 mTorr.

Reproduced with permission of the copyright owner. Further reproduction prohibited without permission.

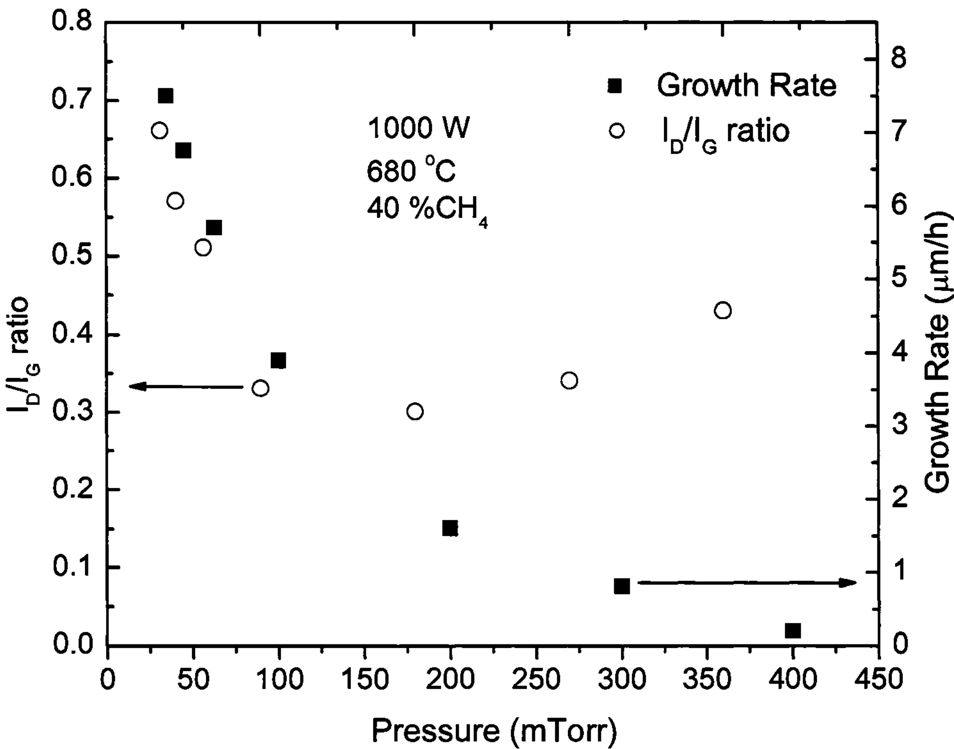

Figure 5.22: The growth rate and the I_D/I_G ratio in Raman spectrum of CNS deposited at various total gas pressures.

Reproduced with permission of the copyright owner. Further reproduction prohibited without permission.

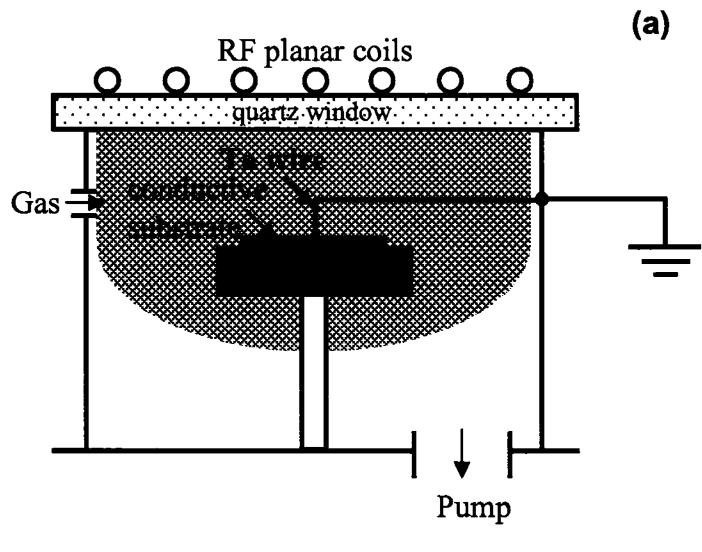

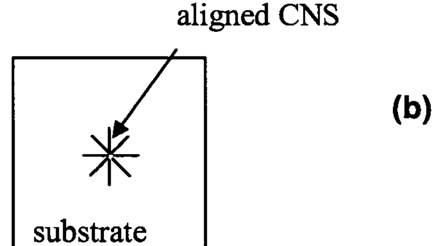

Figure 5.23: (a) Schematics of the experimental setup for aligned CNS formation. (b) Schematics showing the area on the substrate where aligned CNS formed, and the direction of the aligned CNS.

Reproduced with permission of the copyright owner. Further reproduction prohibited without permission.

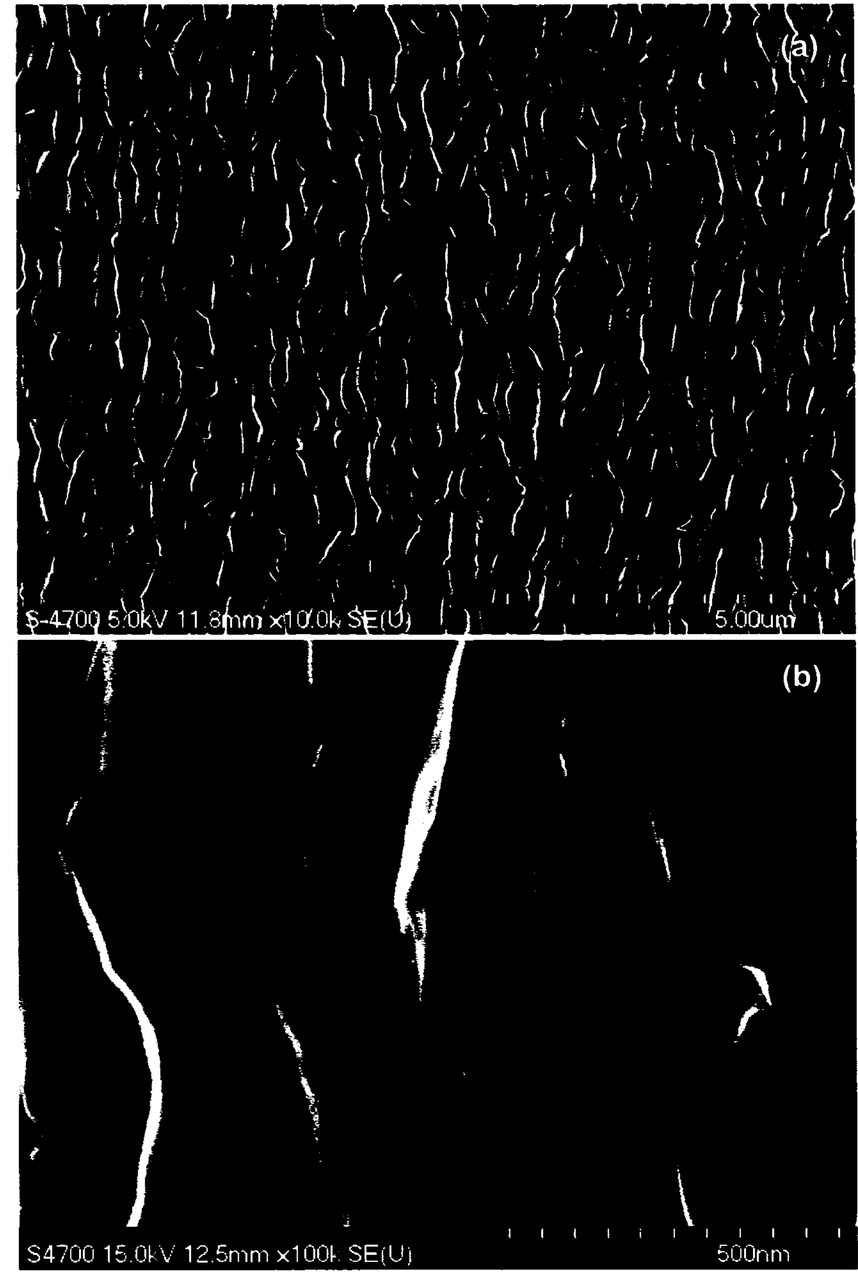

Figure 5.24: SEM images of aligned CNS deposited near the grounded Ta electrode on a heavily doped Si wafer. (a): lower magnification (b): higher magnification images.

Reproduced with permission of the copyright owner. Further reproduction prohibited without permission.

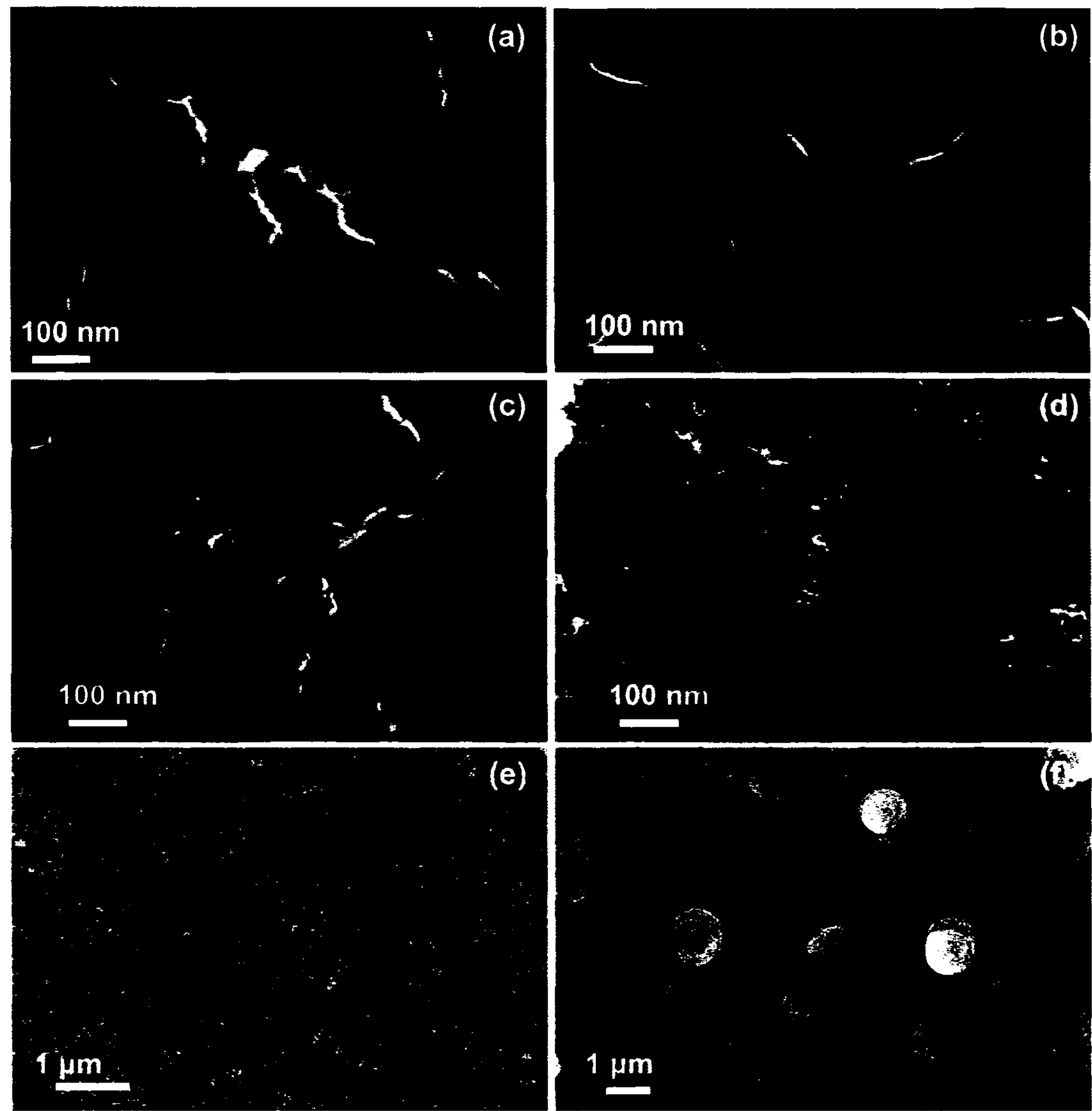

Figure 5.25: SEM images of sheet-like structure deposited on Si substrates in inductive plasmas from (a) 10%, (b) 20%, (c) 40%, (d) 80%, (e) 80% at a lower magnification, and (f) 100% C_2H_2 in H_2 gases. Other conditions are the same as typical CH_4/H_2 CNS depositions.

Reproduced with permission of the copyright owner. Further reproduction prohibited without permission.

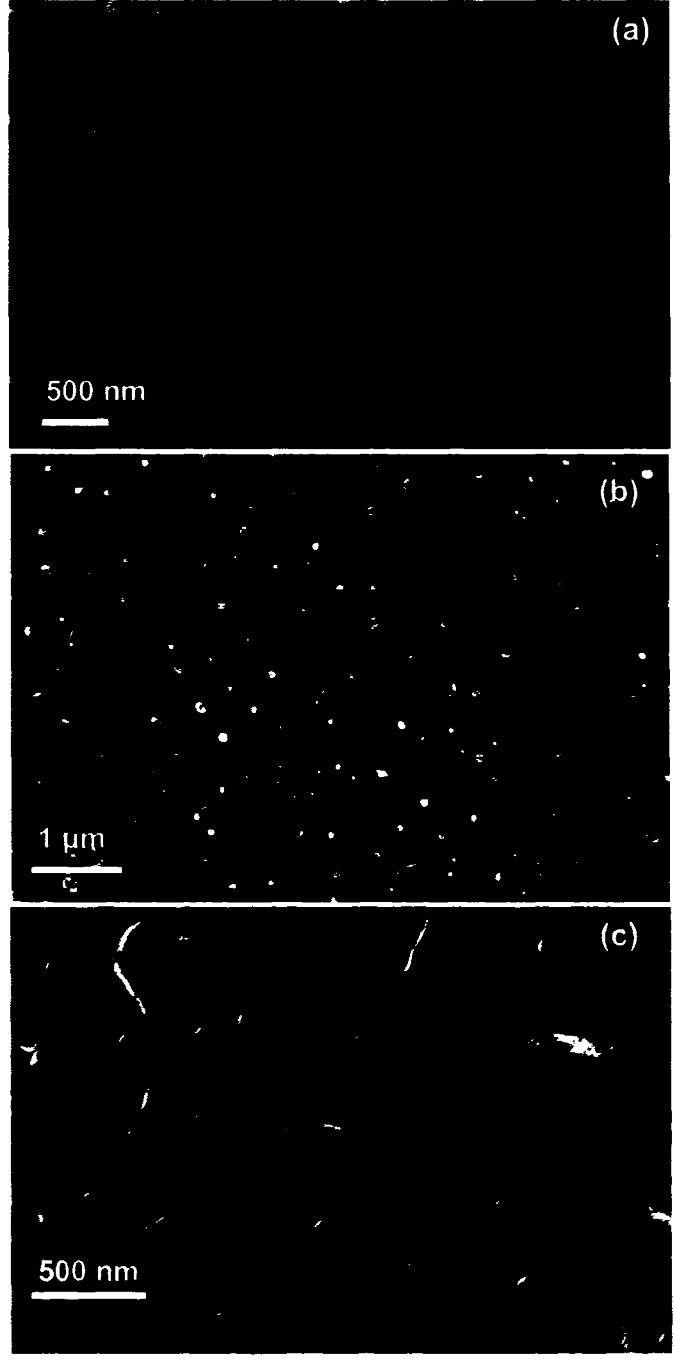

Figure 5.26: SEM images of sheet-like structure deposited on Ni nano-dots patterned Si substrates in inductive plasmas. The gas composition varied from (a) 40%, (b) 60%, and (c) 80% C_2H_2 in NH_3 gases. Other conditions are the same as typical CH_4/H_2 CNS depositions.

Reproduced with permission of the copyright owner. Further reproduction prohibited without permission.

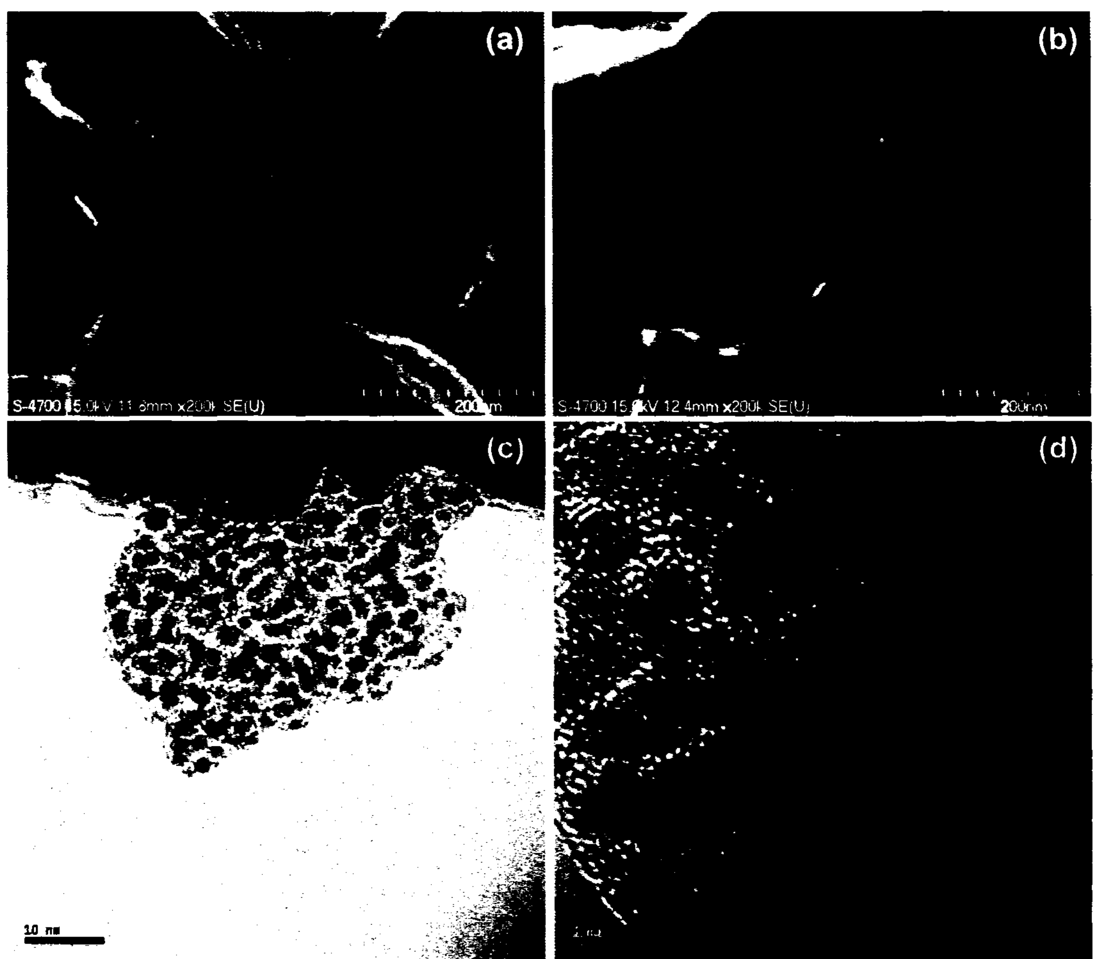

Figure 5.27: SEM images reveal the rough surface morphologies of CNS coated with (a) 2nm Pt and (b) 2 nm Ni via evaporation. (c) TEM micrograph of Pt coated CNS. (d) A high resolution TEM micrograph of Pt coated CNS reveals Pt particles 3-5 nm in diameters.

Reproduced with permission of the copyright owner. Further reproduction prohibited without permission.

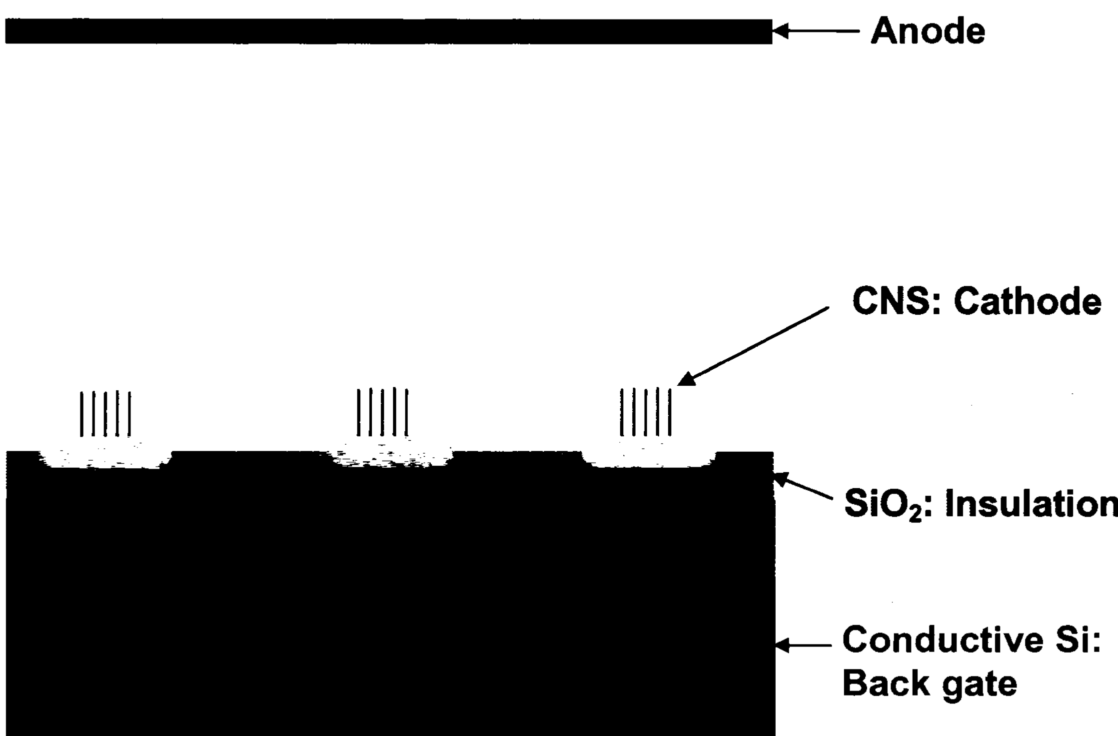

Figure 5.28: Schematics of CNS-based "buried line" back-gated triode field emission device.

Reproduced with permission of the copyright owner. Further reproduction prohibited without permission.

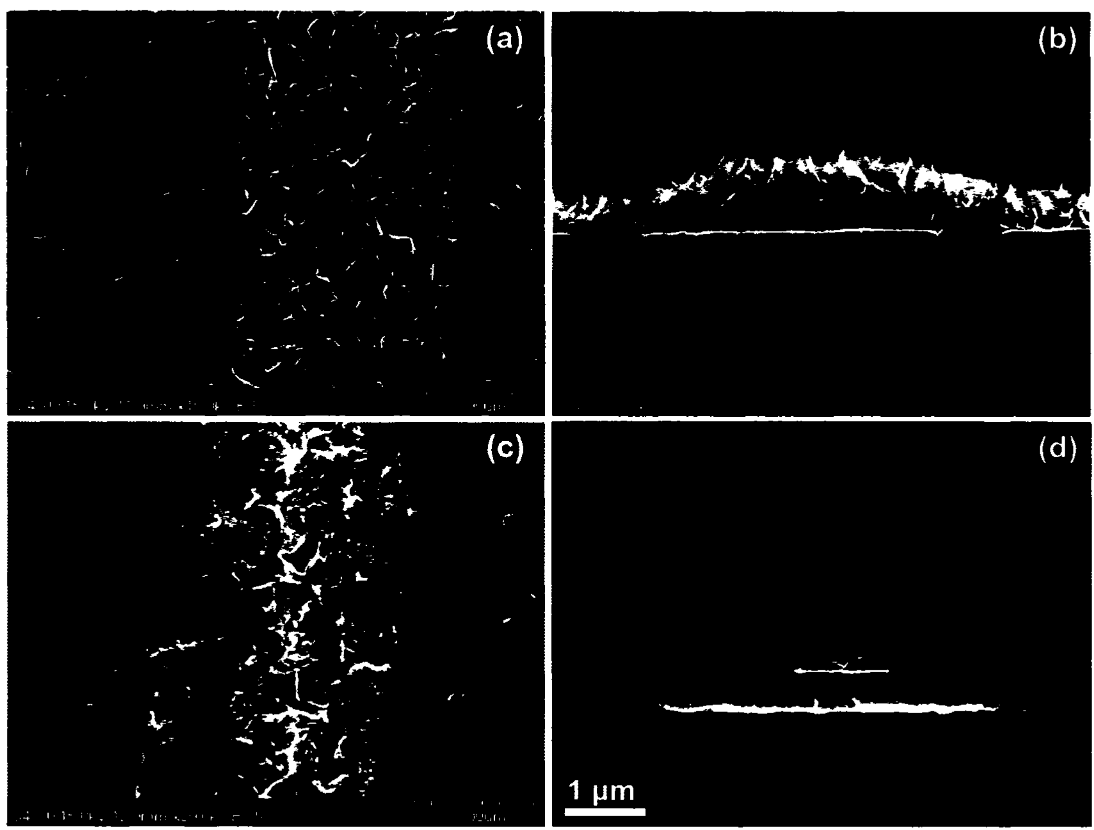

Figure 5.29: (a): Top view and (b) cross-section view SEM images of a blanket layer of as-deposited CNS on both the line and the street areas of a back-gated device. (c): Top view and (d): cross-section view SEM images of patterned CNS on the lines only.

Reproduced with permission of the copyright owner. Further reproduction prohibited without permission.

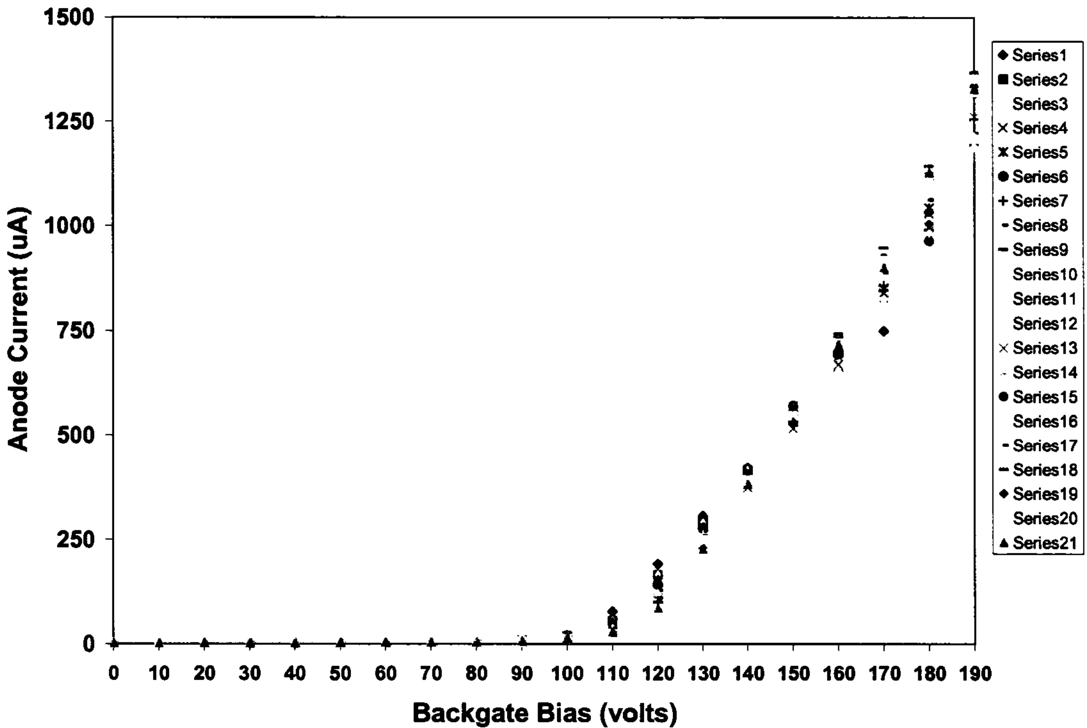

Figure 5.30: Emission current (I) *vs.* the back-gate voltage (V) behavior of a CNS-based buried-line, back-gated device. The diode field is fixed at 9 V/μm.

Reproduced with permission of the copyright owner. Further reproduction prohibited without permission.

Chapter 6

Carbon Nanosheet: Interpretive Model of Growth Mechanism

6.1 Introduction

In previous chapters, we presented experimental results of two carbon nanostructures — carbon nanosheets (CNS) and carbon nanotubes (CNT) — deposited in a radio frequency (RF) plasma enhanced chemical vapor deposition (PECVD) system using inductively and capacitively coupled plasma discharging modes. Our parametric studies of CNS deposition were also presented previously. In this chapter, we discuss the theoretical aspects of the carbon nanosheet growth process, as well as a CNS growth model based on our experimental evidence.

Carbon nanotube growth mechanisms have been investigated thoroughly.[53] It has been suggested that the growth of one-dimensional carbon nanotubes and nanofibers via chemical vapor deposition involves dissolution, bulk diffusion, saturation, and separation

Reproduced with permission of the copyright owner. Further reproduction prohibited without permission.

of carbon from the catalyst particles. The catalyst is important to determine the size and location of the carbon nanotubes.

In contrast, no catalyst is needed for CNS deposition. In our work, the key to CNS deposition is that the plasma is inductively coupled. Table 6.1 compares growth parameters for CNT and CNS depositions.[33] It is clear that all parameters have some overlapping ranges for the growth of these two structures, except for the effects of catalyst and the plasma discharge mode. In fact, as previously discussed in section 5.4.2 and shown in Figure 5.25, CNS deposition is favorable in an inductive plasma even in the presence of a catalyst, and when we use the feedstock gases of typical CNT deposition. Thus, there is no doubt that the set of plasma parameters associated with the inductively coupled plasma is the most important factor for CNS formation in our RF PECVD system.

In this chapter, we propose a semi-quantitative CNS growth mechanism based on the experimental results we obtained from CNS deposition, optical emission spectroscopy (OES) investigation, the analysis of the electric field near the substrate surface in the plasma, and some theoretical thermodynamic calculations. We will also verify the proposed growth mechanism using our parametric study results.

6.2 A phenomenological growth mechanism of CNS

Experimental observations presented in Chapter 4 and 5 reveal that inductively coupled plasmas favor nanosheet growth, as opposed to nanotube growth. In contrast to lower power capacitive plasmas, an inductive discharge using a lower neutral gas pressure and higher input powers results in a plasma density ~10 times higher than a similar capacitive plasma because the ionization rate of the inductively coupled plasma is ~100 times higher

Reproduced with permission of the copyright owner. Further reproduction prohibited without permission.

than capacitively coupled plasma.[30] During the deposition of typical CNS in the RF system, OES indicates that inductive coupling yields a very high atomic hydrogen to growth species ratio,[33,44] which we believe is critical for CNS growth. We discuss this effect in the next sections.

6.2.1 Optical emission spectra of inductively and capacitively coupled plasma

The coupling mechanisms for inductively and capacitively coupled plasmas are different, as previously discussed in Chapter 3 (see Table 3.1). In general, inductively coupled plasma has a higher plasma density compared to capacitively coupled plasma, as a result of the higher power coupling efficiency of inductively coupled plasma. A comparison of these two plasmas was also listed in Table 3.1. Here the differences between these two plasmas are discussed in more detail using the OES observations.

OES is a straightforward and direct method of identifying the composition of a gas mixture because excited species in plasma have unique emission spectra. With some additional effort, one can determine the concentration of activated species in plasma discharges. Using a fiber-optic spectrometer (Ocean Optics, USB2000) with a resolution of 1.3 nm over the wavelength range of 200-800 nm, we collected the spectra of both inductively and capacitively coupled plasmas used for CNS and CNT depositions. As shown in Figure 3.3, one end of the optical fiber was mounted at the top-hat through the antenna, located ~2 cm from the center of the substrate. The other end of the optical fiber was connected to the spectrometer, which was controlled by a computer.

Reproduced with permission of the copyright owner. Further reproduction prohibited without permission.

Figure 6.1 shows a representative optical emission spectrum collected during the deposition of typical CNS in an inductively coupled CH_4/H_2 plasma, and during the deposition of typical CNT in a capacitively coupled C_2H_2/NH_3 plasma. The signal integration times were 300 ms and 2000 ms, respectively. The reduced collection time for the inductive CH_4/H_2 plasma was chosen in order to avoid detector saturation from the very bright emission of the inductive plasma. That is, the total emission intensity of inductive CH_4/H_2 plasma for CNS deposition is much higher than that of the capacitive C_2H_2/NH_3 plasma for CNT deposition. The atomic hydrogen emission peaks, H_α (656.1 nm) and H_β (486.1 nm), dominate the spectrum of the inductive CH_4/H_2 plasma; the peaks from CH (387.0 nm and 431.5 nm) are also labeled.

The dominant peak in the capacitive C_2H_2/NH_3 plasma for CNT deposition, however, is the CH peak at 387.0 nm; the atomic hydrogen peaks are not distinguishable from the background noise. Note that for the direct comparison of the absolute values of the spectra in Figure 6.1, the capacitive C_2H_2/NH_3 plasma spectrum should be reduced by a factor of 6.7. This was not done in order to display the smaller structures of the spectrum.

We also collected OES spectra of inductively coupled plasma for nanosheet deposition with varying growth parameters. The results will be presented in section 6.3 when we interpret how these parameters affect the formation of CNS in terms of the model growth mechanism discussed in the next section.

6.2.2 Interpretive model for CNS growth

Reproduced with permission of the copyright owner. Further reproduction prohibited without permission.

As discussed in Section 5.3, it seems that base layers parallel to the substrates were formed first before the onset of vertically grown sheets. These parallel layers are not visible under SEM because they are flat and uniformly distributed over the substrate surface; however, when the substrate was scratched by a sharp tip, the base layers were peeled off the substrate and could thus be observed under SEM, as seen in Figure 5.14 (e) and (f).

The observation of the base layer suggests that during the first few minutes of growth, graphene layers grow parallel to the substrate surface until the onset of the vertical growth. The exact mechanism of the initiation of this vertical orientation is not completely clear, but possibilities include the stress developed during the growth of parallel layers, which could curl the leading edge of the top layers upward, defects in the parallel layers that cause the flat sheets to curve, an electric field near the substrate surface inducing the vertical orientation of the leading edge into the field direction, normal to the substrate surface, or the combination of two or more of these possibilities.

After the top layers of the base layers curl in the direction of electric field, the very high in-plane mobility of incoming carbon-bearing growth species, and the induced polarization associated with the local electric field near the substrate surface, result in the nanosheets becoming taller rather than thicker. We can only speculate on the precise identity of the mobile species, but carbon atoms, carbon poly-atomic molecules, or small hydrocarbon molecules (all of which are known to be present in our plasma) are likely to have sufficiently high surface diffusion rates to provide the edge growth of the vertical planes.

Reproduced with permission of the copyright owner. Further reproduction prohibited without permission.

For a carbon atom on an ideal graphite surface, for example, the surface diffusion energy, E_d, is 0.13 eV,[54] while the surface adsorption energy, E_a, is ~1.8 eV.[55] So the surface diffusion length, *i.e.* the average distance an atom can migrate along a surface before being re-evaporated,[56] is $\lambda_d = 2a_0 \exp[(E_a - E_d)/2kT_s] = 3.7\,\mu m$ for typical nanosheet growth conditions (a_0=0.1 nm, T_s=1000 K). Here a_0 is the intersite distance, k is Boltzmann's constant (1.381x10^{-23} J/K or 8.62x10^{-5} eV/K), and T_s is the substrate temperature. So in the absence of a high flux of H atoms, which might etch the accreting layers or remove adatoms, we can confidently assume that carbon-bearing species landing on the surface of a growing nanosheet would rapidly diffuse along the sheet surface, reach the edge of the nanosheet, and covalently bond to the edge atoms before being re-evaporated.

After the nucleation of vertical nanosheets, the nanosheets continue to grow while keeping their 2-dimensional structure. Theoretical calculations indicate that there exists an activation energy barrier, ΔE, for distorting the covalent bonds in a flat graphene sheet,[57] even though enclosed structures, such as fullerenes and nanotubes, have a lower total energy due to the elimination of dangling bonds at their edges. Calculations of the value of ΔE for 100 atom graphene layers[57] yield estimates on the order of 10 eV. Furthermore, for a bent nanosheet, the probability of the edges bonding with each other and forming a seamless structure is small, so it is reasonable that the nanosheets intend to keep their 2-dimensional shape. In addition, the vertical electric field near the substrate surface helps to sustain the vertical orientation of CNS.

Electric-field dependent orientation has been observed by others during the growth of carbon nanotubes[58] and thick carbon nanowalls.[59] Electric fields have also been

Reproduced with permission of the copyright owner. Further reproduction prohibited without permission.

used to orient isolated nanotubes for device applications and for purification purposes.[60,61] The alignment of nanosheets in our apparatus is thus expected, since both prior calculations, and measurements, yielded a three-fold difference between in-plane and perpendicular (c-axis) polarizability for ideal graphene layers.[62] The relatively higher in-plane mobility of basal-plane electrons allows a field-induced force to align the dipole moments of the nanosheets along the electric field's direction.

The atomic hydrogen in the plasma acts as an etchant to rapidly remove amorphous carbon defects. This etching promotes a graphitic crystalline structure in the growing layers by preventing the formation of secondary nuclei which might interfere with sheet growth. It removes cross-linking at the free edges of growing sheets, thus, preventing edge thickening, and thereby keeping them atomically thin. A schematic is shown in Figure 6.2 to illustrate the proposed mechanism.

6.2.3 Role of the electric field in CNS growth

In the above analysis, the electric field in the plasma near the substrate surface plays an important role both in promoting the growth at the nanosheet edges, and in inducing an orientation of the growing planes that is perpendicular to the substrate. This section will discuss the formation of the electric field and how it interacts with the nanosheets.

An electric field always exists in the vicinity of a solid object immersed in plasma. The mechanisms for the formation of the sheath field depend on the details of the geometry, the composition of the plasma, the total gas pressure, the time-dependent energy source of the ionization (DC, inductive, capacitive, high or low frequency electric

Reproduced with permission of the copyright owner. Further reproduction prohibited without permission.

fields, laser, incoherent photon, or particle-beam driven), and the details of the solid material at the boundary and its electrical connection to an external circuit.[32]

In our deposition system, the ionization source operates with a pressure-dependent combination of an inductive source and a capacitive source, both coupling in phase at 13.56 MHz. The capacitive contribution comes from the fact that the antenna above the quartz window has peak RF voltages exceeding 1000 volts. The resulting potential oscillations in the plasma are rectified at the conducting boundary of the substrate[32] to provide a strong DC field, oriented downward toward the substrate.[30]

Positive evidence of the importance of the local electric field to the overall CNS growth mechanism is the growth of radially aligned CNS near a grounded electrode, as discussed in section 5.4.1. A grounded electrode, in contrast to a floating object, can conduct a substantial current (to ground), thus the sheath formation is approximately described by a Langmuir-Child mechanism.[30,32] In the vicinity of the substrate, the resulting local electric field along the central length of this electrode is predominately oriented radially with respect to the cylinder axis.

The electric field may also play a significant role by providing ion bombardment to overcome the activation energy barrier (ΔE) associated with the distortion of network of sp^2 bonds in the parallel base layers, which is one of the possible initiation factors for the nucleation of the vertically grown nanosheets.

6.3 Parametric study analysis

Results in section 5.3 show the effects of the growth parameters on the morphology and structure of deposited CNS. The results are summarized in Table 6.2. Ascending and

Reproduced with permission of the copyright owner. Further reproduction prohibited without permission.

descending straight lines with arrows are used to indicate the increases and decreases in the growth rate and degree of order of CNS as their growth parameters change. This section explains how these growth parameters affect the resulting CNS structures according to the growth mechanism described in the previous section.

6.3.1 Substrate temperature

As mentioned in section 5.3.1, increasing substrate temperature causes both the growth rate and disorder of nanosheets to increase. We interpret this in terms of surface diffusion and growth from adsorbed carbon-bearing species. The details depend quite heavily on the exact identity of such species and on the band-structure and surface states of the substrate,[63,64] but a very general argument is all we require here to roughly account for our observations.

In the model introduced in the previous section, we assumed that the primary traps associated with atom-to-atom excursions, as the growth species hop along the planar graphene layer, have depths (E_d) of about 1-2 eV. We also assert that the traps associated with reaching the dangling bonds at the edge of the growing layer lead to covalent bonding with very deep wells (~4-5 eV). The mean time for adsorbates hopping on the surface is $\tau_d = \nu_1^{-1} \exp[E_d /(kT_s)]$, where ν_1 is the lattice vibrational rate constant ($2kT/h$, $\sim 3\times10^{13}$ Hz for T=1000 K),[56] and T_s is the substrate temperature. In such a model, a higher substrate temperature results in a much faster surface diffusion, and consequently, a much faster growth rate. A faster growth rate results in a smaller coherent-layer size and an increased number of defects in the nanosheets.

Reproduced with permission of the copyright owner. Further reproduction prohibited without permission.

6.3.2 Methane concentration

In section 5.3.2, we showed that the growth rate and degree of disorder of CNS also increase with increasing CH_4 concentration, and we believe this is mainly due to the impingement rate of growth species.

The impingement rate is determined by $R = \sqrt{\frac{1}{2\pi\, m\, k\, T_g}} \cdot P_{gs}$, where m, T_g, and P_{gs} represent mass, gas phase temperature, and partial pressure of the growth species, respectively. The impingement rate is roughly linearly proportional to the CH_4 concentration, as revealed by the OES data shown in Figure 6.3, in which the peak intensities were plotted as functions of the CH_4 concentration. We observed that the level of disorder also increased with increasing CH_4 concentration, as measured by Raman spectroscopy and XRD.[43,45] Similar to the effects of higher substrate temperatures, a faster growth rate yields a smaller coherent-layer size and more defects in the nanosheets. Figure 6.4 also indicates a much faster decrease (compared to the emission of CH) of atomic hydrogen emission intensity with increasing CH_4 concentration. A lower atomic hydrogen etching effect is another reason for the smaller coherent-size, and the higher number of defects in the resulting nanosheets.

6.3.3 Input RF power

By increasing the RF power at fixed total pressure and fixed CH_4 in H_2 concentration, both the growth rate and the degree of order of CNS increase, as presented in section 5.3.3. The increased growth rate at a higher RF power is believed to be a result of increased growth species density, similar to the effects of a higher CH_4 concentration.

Reproduced with permission of the copyright owner. Further reproduction prohibited without permission.

Figure 6.4 (a) shows the increase of growth species OES emission peak densities with increasing input RF powers, which is the result of a higher neutral gas dissociation rate at higher input RF powers.

However, the faster growth did not yield a more defective structure, as it did in response to increasing substrate temperature or CH_4 concentration. We interpret this as the result of a dramatic increase in the atom hydrogen density in the plasma. Figure 6.4 (b) shows the ratios of atomic hydrogen to growth species emission intensity as the input RF power is varied. The higher ratios at higher RF powers result in faster etch rates for defects. Therefore the relative level of disorder decreases as the RF power increases, even with a faster growth rate.

6.3.4 Total gas pressure

The effect of variations in the total gas pressure is a bit more complicated than variations in other parameters. In the range studied (20-400 mTorr), the dissociation rate in our system is inversely proportional to total pressure, as revealed by the OES spectra (Figure 6.5). Thus one might expect the effects of lowering total pressure to be similar to that of raising RF power. However, this is not what we observed.

At lower total pressures, the expected faster growth rate was achieved, but the sheets contained more defects, rather than fewer defects, as previously seen in section 5.3.4. To account for this, we considered a somewhat more involved analysis of the effects of the sheath on the ion bombardment energy, which happen wherever collisions occur between the fast ions accelerating through the sheath electric field and the slow

Reproduced with permission of the copyright owner. Further reproduction prohibited without permission.

neutral atoms in the background gas. Lieberman[2] and Manos[30,32] provide more details of these analyses.

Using Langmuir probe methods,[32] we measured a plasma potential $V_p \sim 70$ V in the plasma used for nanosheet growth. For singly ionized ions, in the absence of collisions, this is an upper boundary for the energy of an incident ion. Note that this energy is well above the binding energy of a carbon atom in a graphene sheet (~7.4 eV).[65] However, when elastic and charge-exchange collisions with the background gas are taken into account,[66] the actual distribution of ions can be approximated by a decaying exponential with a mean energy that falls as $P^{-1/2}$, where P is the total gas pressure, yielding numerical values of mean energy far lower than the collisionless sheath voltage.[67] The essence of this analysis is derived from the primary length parameters that dictate the number of collisions in the sheath, n, leading to a slowing of the energy distribution. These length parameters are the sheath thickness, which in such plasmas is proportional [68] to $P^{-1/2}$, and the mean free path for elastic collisions, which is proportional to P^{-1}. These combine to yield n proportional to $P^{1/2}$, and thus a mean energy per ion that is proportional to $P^{-1/2}$. For the experimental conditions for nanosheet deposition, we estimate the particle energy to be ~2-8 eV over the total pressure range of 400-20 mTorr. At lower pressures, the top of this energy range is adequate to break the sp^2 hybridized C-C bonding energy (7.4 eV) in graphene layers. Recall that the detailed distribution has a high energy tail that falls off roughly exponentially, therefore the most energetic particle bombardment at lower pressure can produce etchable defects in crystalline carbon structures. Such damage production is

Reproduced with permission of the copyright owner. Further reproduction prohibited without permission.

similar to that accounting for ion-enhanced etching during carbon nanofiber synthesis, as reported by Wei, *et al.*[69]

6.4 Summary

This chapter presents a plausible CNS growth mechanism primarily based on the experimental observations of the material morphology, when interpreted in combination with plasma observations by optical emission spectroscopy (OES). The plasma parameters associated with our radio frequency inductively coupled plasma strongly favor the formation of atomically thin, free-standing 2-dimensional carbon nanosheets over the formation of carbon nanotubes.

Under typical CNS growth conditions, there is a 2-4 minute latency period, during which a base layer parallel to the substrate surface forms, before the onset of vertically grown CNS. The possible initiation of the vertical sheet growth includes the stress in the parallel layers, defects in the graphene network, and the electric field near the substrate surface.

High surface diffusion lengths of the growth species on graphene surfaces indicate that such surface diffusion is the main source of growth at the edges. The two-dimensional flat graphitic sheet structure is stable according to the thermodynamic calculations.

The vertical electric field at the substrate surface plays an important role in promoting and preserving the 2-D morphology and the vertical orientation of free-standing CNS. The large amounts of atomic hydrogen in the inductive plasma is critical to the formation of atomically thin sheets, by etching amorphous carbon defects,

Reproduced with permission of the copyright owner. Further reproduction prohibited without permission.

preventing the formation of secondary nuclei, and removing cross-linking at the free edges of growing sheets.

Our growth mechanism is consistent with, and accounts for, our experimental observations of the growth of carbon nanosheets with varying parameters, *i.e.* the changes of CNS growth and structure with variations in the substrate temperature, the gas composition, the input RF power, and the total gas pressure.

This initial semi-quantitative analysis of the CNS growth process, mostly based on experimental observations is quite qualifying. It leads us to be optimistic about undertaking theoretical and computational work to develop a complete and quantitative model for CNS formation.

Reproduced with permission of the copyright owner. Further reproduction prohibited without permission.

Table 6.1: Parameters for CNT and CNS deposition in the RF PECVD system.

Parameters	CNT	CNS
Catalyst	Necessary	No effect
Plasma pre-etching	Yes	No effect
Deposition temp. (°C)	~700	~700
Gas compositions	20%CH_4 in H_2; 20%C_2H_2 in NH_3	10-100%CH_4 in H_2; 20-80% C_2H_2 in NH_3
Pressure (Torr)	~1.0	0.02-0.4
Plasma power (W)	700	400-1200
Sample stage	Grounded	No effect
Plasma coupling mode	Capacitively coupled	Inductively coupled

Reproduced with permission of the copyright owner. Further reproduction prohibited without permission.

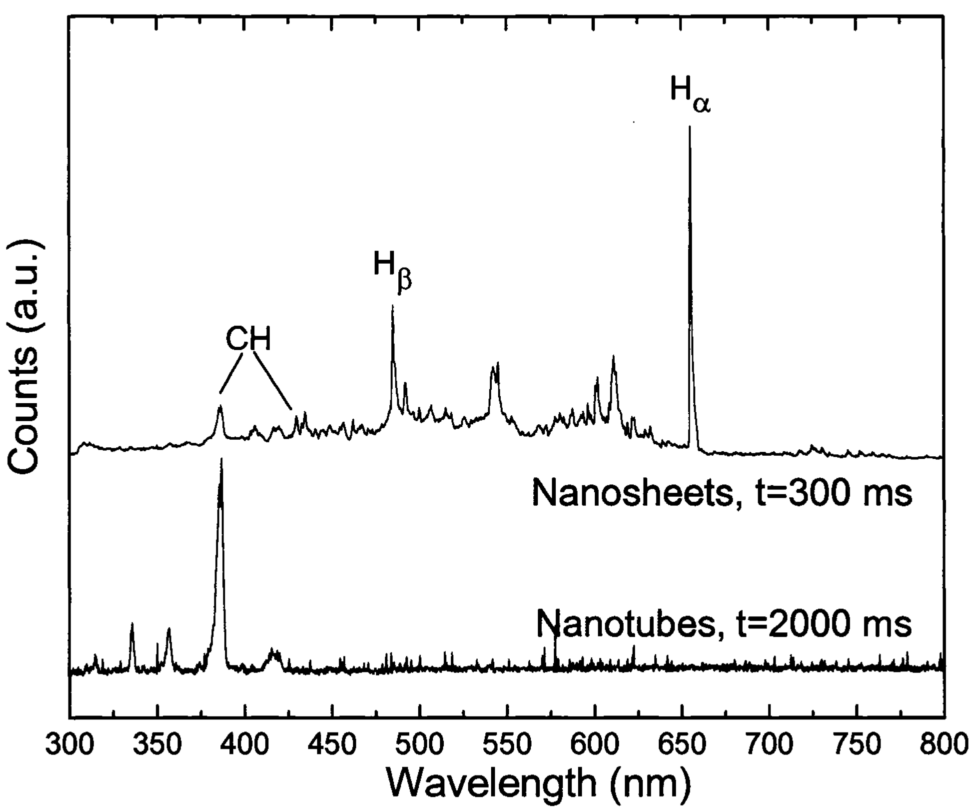

Figure 6.1: Optical emission spectra for inductively coupled plasma of typical CNS deposition and capacitively coupled plasma for CNT deposition. The collection times were 300 ms and 2000 ms, respectively.

Reproduced with permission of the copyright owner. Further reproduction prohibited without permission.

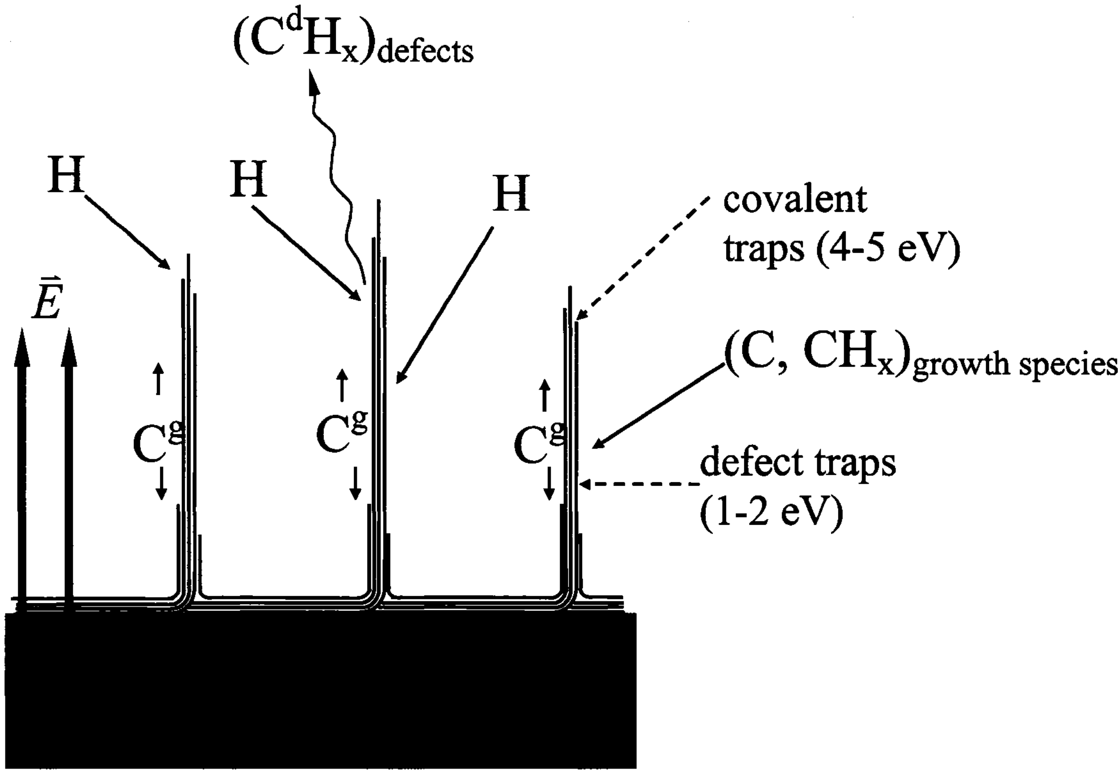

Figure 6.2: A schematic representing the CNS growth mechanism. C^g = "crystalline" graphitic carbon; C^d = defect site carbon; H= atomic hydrogen.

Reproduced with permission of the copyright owner. Further reproduction prohibited without permission.

Table 6.2: Trends in growth rate and orderliness of CNS as their growth parameters, including substrate temperature, CH_4 concentration, input RF power, and total gas pressure, change.

Parameters	**Growth rate**	**Degree of order**
Substrate Temp. (600-900 °C)	↗	↘
CH_4% (5-100%)	↗	↘
RF power (400-1200 W)	↗	↗
Total pressure (50-200 mTorr)	↘	↗

Reproduced with permission of the copyright owner. Further reproduction prohibited without permission.

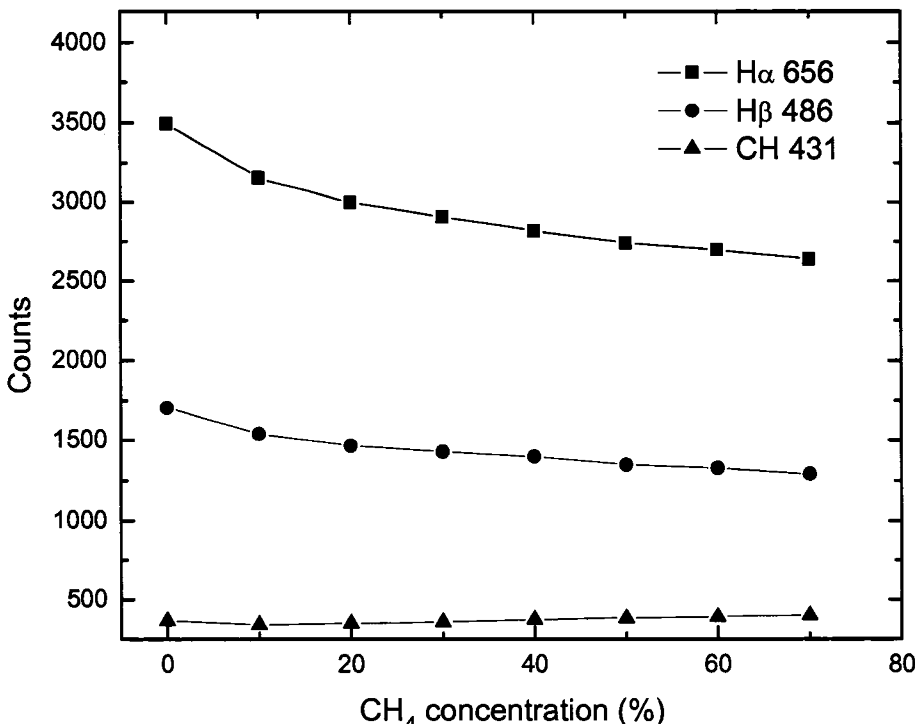

Figure 6.3: Peak intensities of the OES for the plasma used for CNS deposition at various CH_4 concentrations. The CH peak intensity increases with CH_4 concentration, while the atomic hydrogen peaks decrease.

Reproduced with permission of the copyright owner. Further reproduction prohibited without permission.

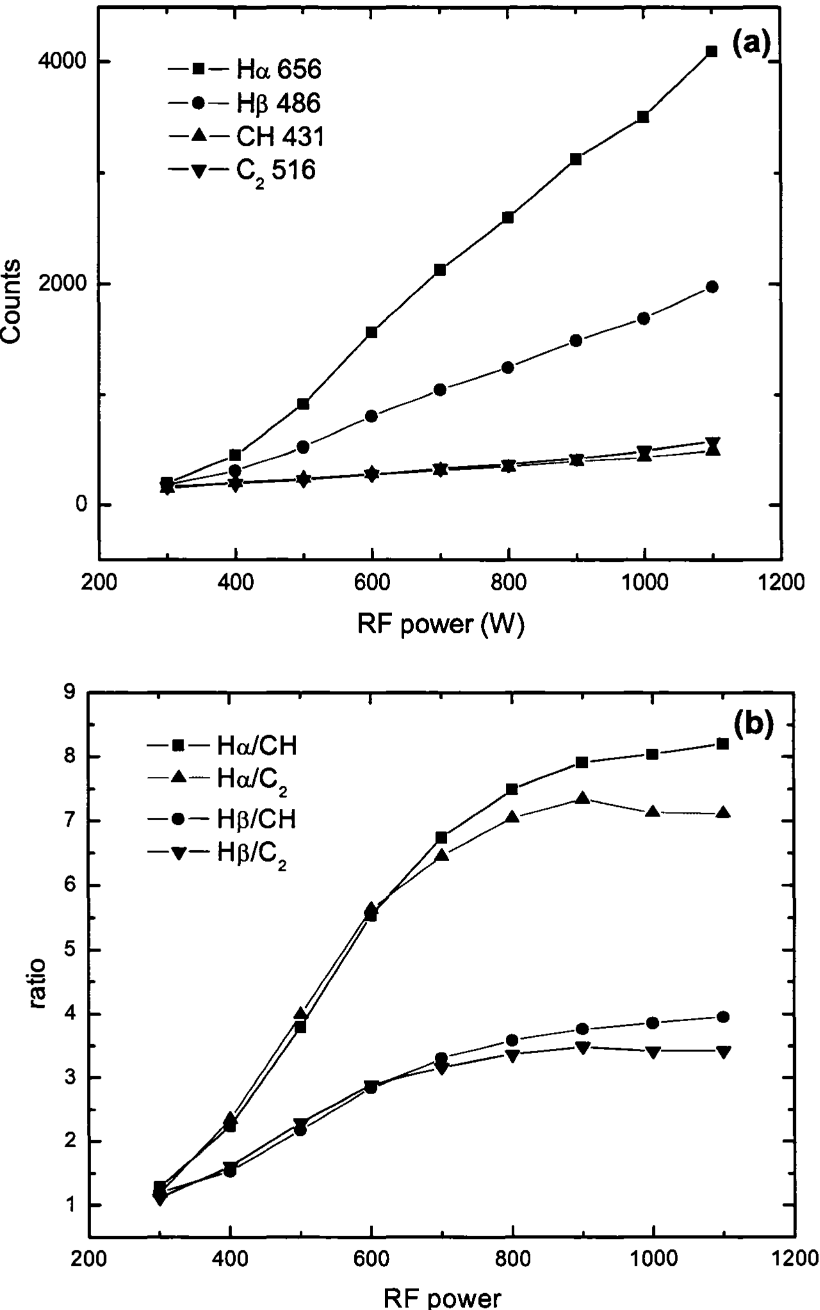

Figure 6.4: Optical emission peak intensities as functions of the input RF power. (a) All the peaks plotted increase with input RF power, and (b) the atomic hydrogen to growth species intensity ratio also increases with input RF power.

Reproduced with permission of the copyright owner. Further reproduction prohibited without permission.

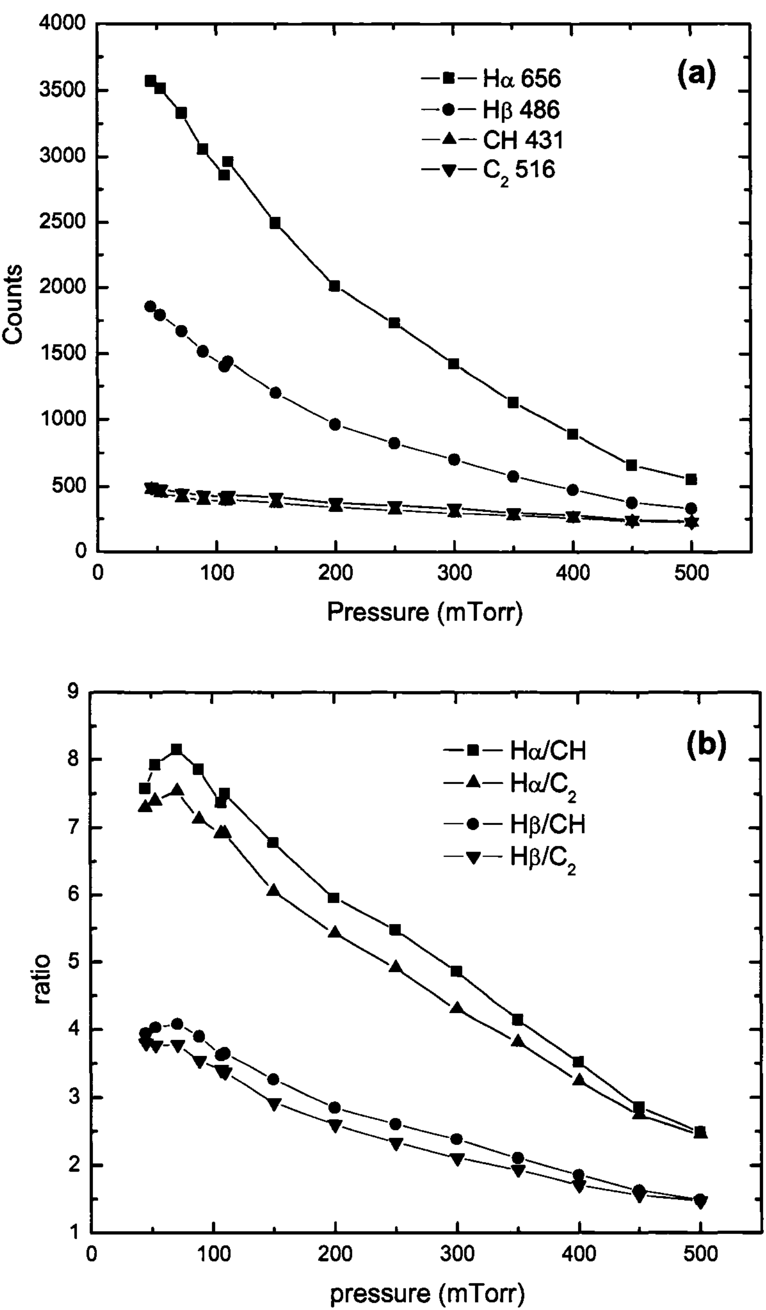

Figure 6.5: Optical emission peak intensities as functions of the total gas pressure. (a) All the peaks plotted decrease with total gas pressure, and (b) the atomic hydrogen to growth species intensity ratio also decreases with total gas pressure.

Reproduced with permission of the copyright owner. Further reproduction prohibited without permission.

Chapter 7

Conclusion and Future work

7.1 Conclusion

During the course of this work, a planar antenna RF PECVD system was designed and built for carbon nanostructure synthesis. When operated in different plasma coupling modes, two different carbon nanostructures were obtained. One-dimensional (1-D) CNT were deposited using capacitively coupled plasma with Ni nano-dots as the catalyst, while 2-D CNS were deposited using inductively coupled plasma without a catalyst. The unique setup of this planar antenna configuration enables quick switchover between these two plasma coupling modes, and consequently the synthesized carbon nanostructures, by simply adjusting the input RF power and gas pressure. Generally, the inductive plasma is dramatically brighter than the capacitively coupled plasma. Consequently, a sudden change in brightness is associated with an abrupt transition between these two plasma coupling modes. Therefore, the optical emission density, or the brightness of the plasma discharge, is a useful indicator of the plasma coupling mode.

Reproduced with permission of the copyright owner. Further reproduction prohibited without permission.

Our group used various characterization techniques to investigate the morphology, structure, composition and properties of the carbon nanostructures synthesized in the RF PECVD system. Brief introductions of the principles and instrument setup of these techniques were presented in Chapter 2. The characterization techniques used include SEM, EDS, TEM, SAD, AFM, Raman, FTIR, XRD, AES, XPS, PIXE, ERDA, TDS, Field emission, 4-point resistivity, and BET surface area measurement.

In addition, a simple, economical, and effective lithography technique, nanosphere lithography (NSL), was developed to pattern catalysts on substrates used for CNT synthesis. Nanosphere lithography has an advantage over the self-assembling mask nanospheres, as NSL can pattern catalysts over a large area, up to centimeter scale. In our work, periodic arrays of Ni dots were patterned from single-layer and double-layer NSL using polystyrene spheres 419 nm in diameter. Randomly oriented, base-grown, multi-wall CNT were successfully synthesized on Si substrates with Ni catalyst patterned in capacitively coupled plasma, using C_2H_2 and NH_3 as feedstock gases. Vertically aligned arrays of tip-grown CNT were prepared on SiO_2-coated Si substrates with Ni catalysts under typical CNT growth conditions. Furthermore, one-dimensional carbon nanofibers were deposited when using CH_4 and H_2 as feedstock gases. Finally, back-gated field emission devices using CNT as cathode material were fabricated and tested, with promising results.

An atomically thin, free-standing, and impurity-free 2-D carbon nanostructure, carbon nanosheets, was deposited for the first time in a RF PECVD system. The CNS deposition in our RF PECVD system is catalyst free, non-selective of substrate material, and viable over a wide range of growth parameters. The catalyst independency and non-

Reproduced with permission of the copyright owner. Further reproduction prohibited without permission.

selective substrate material compatibility could give CNS great potential and flexibility in both research and industry applications. The CNS prepared in the RF PECVD system are the first reported 2-D carbon structures that are atomically thin, free-standing, and free from metallic impurities and other carbon allotropes (CNT or fullerenes). However, our CNS do have defective crystalline graphitic structures with large amounts of hydrogen incorporated via surface absorption, bulk adsorption, and chemical bonding at defects and edge sites.

The orderliness of the CNS was measured by the D to G peak ratio, I_D/I_G, in the Raman spectra of CNS samples, and the crystalline size of the CNS was calculated from I_D/I_G, as well. Low energy peaks in Raman spectra were observed for the first time in 2-D carbon nanostructures.

A systematic parametric study was conducted to investigate the effects of growth parameter variations on the morphology and properties of CNS deposited in the RF PECVD system. The parameters studied include the substrate temperature, the concentration of CH_4 in H_2 atmosphere, the input RF power, and the total gas pressure. When varying one of the parameters, all others were kept constant at their typical values. There exists a critical substrate temperature, below which no CNS deposition was observed. The critical temperature is dependent on other growth parameters, for typical CNS growth condition, it is 600 °C. An increase in substrate temperature decreases the degree of order of CNS, but yields a faster growth rate and more corrugated surface morphologies. Variations in the CH_4 concentration change the morphology of CNS only slightly; however, higher CH_4 concentrations increase the growth rate and decrease the degree of order of the CNS. An increase in input RF power increases the growth rate and

Reproduced with permission of the copyright owner. Further reproduction prohibited without permission.

the degree of order of CNS, and yields a smoother morphology. The effect of total gas pressure variations is two-folded. At low pressures, increasing the total gas pressure results in CNS with a better surface morphology and a higher degree of order, but a slower growth rate. However, at high pressures, both the growth rate and the degree of order decrease with increasing total gas pressure, and the CNS are significantly thickened at high pressures. The pressure not only affects CNS growth directly, but also changes the plasma behavior. At high pressures, the inductive plasma shrinks to a small range underneath the antenna.

Carbon nanosheets were deposited in inductively coupled plasma from various gas compositions, including CH_4/H_2, C_2H_2/H_2, and C_2H_2/NH_3, though the growth parameters and the morphologies of the structures are slightly different. By applying an external electric field near a conductive substrate surface using a grounded electrode, we obtained CNS arrays aligned parallel to the substrate surface.

We demonstrated that CNS have promising application properties. For field emission applications, CNS material has better total emission current, better emission current density, and longer lifetime emission stability than the state-of-art metallic-tip field emission arrays (FEA) and CNT FEA. Furthermore, because they do not require catalyst, nor are they substrate specific, it is much easier to fabricate and pattern CNS than metal tips and CNT cathodes. CNS have also been successfully used as cathode material and fabricated into back-gated field emission devices.

In addition to their potential a field emission material, the high surface area of CNS make them good candidates for catalyst support materials. Preliminary results show that CNS can stabilize 1-2 nm thick Pt thin films as nanoparticles 3-5 nm in diameter.

Reproduced with permission of the copyright owner. Further reproduction prohibited without permission.

These Pt nanoparticles are ideal for fuel cell applications. The high surface area of CNS may also make them good candidates for gas uptake and storage materials.

A semi-quantitative mechanism of CNS growth in the RF PECVD system was proposed, based primarily on experimental evidence, combined with OES results, analyses of electric fields in plasma, and theoretical thermodynamic calculations. A series of short duration depositions revealed the formation of a base layer parallel to the substrate surface which occurred before the onset of the vertically oriented sheet growth. Overall results indicate that the high plasma density and atomic hydrogen ratio of the inductively coupled plasma is the most important factor for CNS growth. This growth is achieved through the surface diffusion of growth species. The vertical orientation is a result of interactions with the local electric field, and the atomic thickness is due to the atomic hydrogen etches. Furthermore, the proposed mechanism is consistent with the results of our parametric study.

7.2 Future work

The study of two-dimensional carbon nanostructure is still relatively new. Indeed there are very few 2-D materials of any sort that can be compared to theoretical study; the comparison to ideal (single-sided) surfaces of bulk 3-D materials is not direct. However, the inductively coupled RF PECVD system was quite successful in the synthesis of this nearly ideal 2-D (double-sided sheet) carbon nanostructure. There is huge potential in many research fields for investigating both the fundamental science, and application potential of this novel 2-D structure.

Reproduced with permission of the copyright owner. Further reproduction prohibited without permission.

The effects of multi-parameter variations on the growth of CNS could yield some interesting results. In our parametric study, we only varied one of the parameters while maintaining all others at fixed values. By varying more than one parameter simultaneously, CNS with unique structures and properties could be obtained. For instance, at higher input RF power and CH_4 concentration, CNS could grow at substrate temperatures lower than the typical critical temperature. This is useful for coating CNS on temperature sensitive substrate materials. Growing CNS with better crystallinity might be possible at low temperatures, low CH_4 concentrations, and high input RF power, while CNS with more defects could be obtained by changing these growth parameters into the opposite direction.

Scanning tunneling microscopy (STM) experiments on CNS samples would be very useful in detecting local defects in CNS and the local density of state at the edges of CNS. Transport properties along the basal plane can be derived by measuring *i-v* curves from individual nanosheets. STM in a vacuum, with dosing capability, can study the absorption properties of different gases on CNS surfaces. It would also be interesting to measure the surface roughness of CNS using atomic force microscopy (AFM), though an appropriate procedure to detach the CNS from the base layer and attach them parallel to a substrate must be developed. CNS thickness is currently measured by SEM and TEM observation for as-deposited CNS. Direct measurements of the edge thickness using AFM could confirm current SEM and TEM results.

Also, to better understand and control the growth of CNS, a quantitative growth mechanism of CNS is needed. Characterization of the plasma under various deposition conditions can provide more information regarding plasma density, sheath thickness, and

Reproduced with permission of the copyright owner. Further reproduction prohibited without permission.

electric field intensity. Computer modeling, such as MAGIC, could also be used to calculate the electric fields near substrate surfaces in plasma.

Scaling up the RF PECVD system could yield uniform CNS coatings on 6 inch, 8 inch, or even 12 inch substrates. Scaling up the inductive RF PECVD system is not an easy task, but it is possible, and very promising. Colpo, *et al.*,[70] have demonstrated ICP uniformities better than 12% over an area of 60×60 cm^2. CNS growth is not self-limited; therefore mass production of CNS could easily be realized in a large scale system, simply by increasing the deposition duration.

Along the same line, but probably somewhat more difficult, aligned CNS could be deposited over a larger area. In our work, the sheath thickness near the surface of a grounded electrode in plasma was relatively small; therefore, the aligned CNS we obtained only covered a small area around the electrode contact point on the substrates. Large areas of aligned CNS deposition are possible by utilizing careful designs that can apply additional electric fields with enough intensity over a large area in the plasma near the substrate surfaces.

Finally, there are numerous areas for potential applications of CNS. We already demonstrated the potential of using CNS as field emission electron sources for flat-panel displays, microwave tubes, X-ray tubes, and electron microscopes. We also presented preliminary but promising results of using CNS as catalyst supporting materials, which could greatly lower the cost for fuel cell manufactures. Further efforts are needed to test the catalyst efficiency of the Pt/CNS structure and integrate it with practical fuel cell units. The high surface area of CNS also makes it a potential gas uptake and storage material.

Reproduced with permission of the copyright owner. Further reproduction prohibited without permission.

Solar energy is one of the alternative energies with great potentials. The good conductivity and large surface area of CNS could increase the conversion efficiency of solar energy, thus expanding its potential. By using CNS as electrode material in photovoltaic applications, scientists can continue to develop solar energy as a viable alternative energy source.

In the past, carbon nanotubes have been used as electromagnetic interference (EMI) shielding material. But because of their good conductivity, easy synthesis, light weight, and low-cost mass production capabilities, CNS could be as good as, or better than, CNT in this capacity.

Finally, CNS are self-assembled free-standing structures. Most biological materials are self-assembled, as well. It might be possible to use CNS in biological applications. CNT have been used as scaffold material for cell, tissue, and organ growth, but CNS might be even better because of their large surface areas and self-assembled vertical orientation.

Reproduced with permission of the copyright owner. Further reproduction prohibited without permission.

Bibligraphy

[1] H. Gleiter, Acta Materialia **48** (1), 1 (2000)

[2] J. J. Wang, M. Y. Zhu, R. A. Outlaw *et al.*, Applied Physics Letters **85** (7), 1265 (2004)

[3] Y. H. Wu, P. W. Qiao, T. C. Chong *et al.*, Advanced Materials **14** (1), 64 (2002)

[4] H. W. Kroto, J. R. Heath, S. C. O'Brien *et al.*, Nature (London, United Kingdom) **318** (6042), 162 (1985)

[5] Thomas W. Ebbesen, *Carbon Nanotubes: Preparation and Properties.* (CRC Press, Inc., 1997) 296 pp.

[6] Mildred. S. Dresselhaus, Gene Dresselhaus and Phaedon Avouris, *Carbon Nanotubes Synthesis, Structure, Properties, and Applications.* (Springer, 2001) 447 pp.

[7] Sumio Iijima, Nature (London, United Kingdom) **354** (6348), 56 (1991)

[8] Y. Ando, X. Zhao and M. Ohkohchi, Carbon **35** (1), 153 (1997)

[9] Alfred T.H. Chuang, Bojan O. Boskovic and John Robertson, Diamond and Related Meterials **15**, 1103 (2006)

Reproduced with permission of the copyright owner. Further reproduction prohibited without permission.

[10] N. G. Shang, F. C. K. Au, X. M. Meng *et al.*, Chemical Physics Letters **358**, 187 (2002)

[11] Takashi Itoh, Seiji Shimabukuro, Shigeo Kawamura *et al.*, Thin Solid Films **501** (1-2), 314 (2006)

[12] K. Shiji, M. Hiramatsu, A. Enomoto *et al.*, Diamond and Related Materials **14** (3-7), 831 (2005)

[13] Guohua Chen, Wengui Weng, Dajun Wu *et al.*, Carbon **42** (4), 753 (2004)

[14] K. S. Novoselov, A. K. Geim, S. V. Morozov *et al.*, Science **306** (5296), 666 (2004)

[15] Lisa M. Viculis, Julia J. Mack and Richard B. Kaner, Science **299** (5611), 1361 (2003)

[16] Ludwig Reimer, *Scanning Electron Microscopy: Physics of Image Formation and Microanalysis*, 2nd ed. (Springer-Verlag, 2000) 527 pp.

[17] B Fultz and J. M. Howe, *Transmission Electron Microscopy and Diffractometry of Materials*. (Springer-Heiderberg, 2002) 748 pp.

[18] G. Binnig, C. F. Quate and Ch. Gerber, Physical Review Letters **56** (9), 930 (1986)

[19] John R. Ferraro, Kazuo Nakamoto and Chris W. Brown, *Introductory Raman Spectroscopy*, Second Edition ed. (Academic Press, 2003) 434 pp.

[20] Willes H. Weber and Roberto Merlin, *Raman Scattering in Materials Science.* (Springer-Verlag, 2000) 402 pp.

[21] Henning Hubert and Holger Jenett, *Surface and Thin Film Analysis, Principles, Instrumentations, Application*. (Wiley-VCH Verlag, 2002) 336 pp.

[22] Xin Zhao, Ph. D. dissertation, College of William and Mary, 2006

Reproduced with permission of the copyright owner. Further reproduction prohibited without permission.

[23] Sven A. E. Johansson, John L. Campbell and Klas G. Malmqvist, *Particle-Induced X-Ray Emission Spectrometry (PIXE)*. (John Wiley & Sons, 1995) 451 pp.

[24] http://www.rzg.mpg.de/~mam/

[25] L. J. van der Pauw, Philips Technical Review **20**, 220 (1958)

[26] X. Zhao, R.A. Outlaw, J.J. Wang *et al.*, Journal of Chemical Physics **124**, 194704 (2006)

[27] Stephen Brunauer, P. H. Emmett and Edward Teller, Journal of American Chemical Society **60** (2), 309 (1938)

[28] Nimel Theodore, Ph. D., College of William and Mary, 2006

[29] Hugh O. Pierson, *Handbook of Chemical Vapor Deposition (CVD) Principle, Technology, and Applications*, 2nd. ed. (Noyes Publication/William Andrew Publishing, LLC, Norwich, 1999) 482 pp.

[30] Michael A. Lieberman and Allan J. Lichtenberg, *Principles of Plasma Discharges and Materials Processing*. (John Wiley & Sons, Inc., New York, 1994) 572 pp.

[31] M. Hiramatsu, K. Shiji, H. Amano *et al.*, Applied Physics Letters **84** (23), 4708 (2004)

[32] Dennis M. Manos and Daniel L. Flamm, *Plasma Etching, An Introduction*. (Academic Press, Inc., 1989) 476 pp.

[33] Mingyao Zhu, Jianjun Wang, Ronald. A. Outlaw *et al.*, Diamond and related materials (in press) (2006)

[34] Jie Liu, Andrew G. Rinzler, Hongjie Dai *et al.*, Science **280** (5367), 1253 (1998)

[35] H. W. Deckman and J. H. Dunsmuir, Applied Physics Letters **41** (4), 377 (1982)

Reproduced with permission of the copyright owner. Further reproduction prohibited without permission.

[36] H. W. Deckman and J. H. Dunsmuir, Journal of Vacuum Science & Technology B: Microelectronics and Nanometer Structures **1** (4), 1109 (1983)

[37] H. W. Deckman, J. H. Dunsmuir, S. Garoff *et al.*, Journal of Vacuum Science & Technology B: Microelectronics and Nanometer Structures **6** (1), 333 (1988)

[38] Z. P. Huang, D. L. Carnahan, J. Rybczynski *et al.*, Applied Physics Letters **82** (3), 460 (2003)

[39] J. J. Wang, M. Y. Zhu, X. Zhao *et al.*, Journal of Vacuum Science & Technology B: Microelectronics and Nanometer Structures **22** (3), 1269 (2004)

[40] M. Chhowalla, K. B. K. Teo, C. Ducati *et al.*, Journal of Applied Physics **90** (10), 5308 (2001)

[41] M. Y. Zhu, J. J. Wang, R. A. Outlaw *et al.*, Technical Digest of the International Vacuum Nanoelectronics Conference, 17th, 98 (2004)

[42] T. Tyler, O. Shenderova, M. Ray *et al.*, Journal of Vacuum Science and Technology B: Microelectronics and Nanometer Structures, accepted (2006)

[43] J. J. Wang, M. Y. Zhu, R. A. Outlaw *et al.*, Carbon **42** (14), 2867 (2004)

[44] J.J. Wang, M.Y. Zhu, H. Tian *et al.*, Journal of Vacuum Science & Technology B: Microelectronics and Nanometer Structures (submitted)

[45] B. L. French, J. J. Wang, M. Y. Zhu *et al.*, Journal of Applied Physics **97** (11), 114317/1 (2005)

[46] Sigen Wang, Jianjun Wang, Peter Miraldo *et al.*, Applied Physics Letters, in press (2006)

[47] T. W. Ebbesen and P. M. Ajayan, **358** (6383), 220 (1992)

Reproduced with permission of the copyright owner. Further reproduction prohibited without permission.

[48] Yoshinori Ando and Sumio Iijima, Japanese Journal of Applied Physics **32**, L107 (1993)

[49] S. Iijima, T. Wakabayashi and Y. Achiba, J. Phys. Chem. **100** (14), 5839 (1996)

[50] Q. Kuang, S. Y. Xie, Z. Y. Jiang *et al.*, Carbon **42** (8-9), 1737 (2004)

[51] S. Kurita, A Yoshimura, H Kawamoto *et al.*, Journal of Applied Physics **97** (10), 104320 (2005)

[52] R. J. Nemanich, G. Lucovsky and S. A. Solin, Materials Science and Engineering **31**, 157 (1977)

[53] Reginald B. Little, Journal of Cluster Science **14** (2), 135 (2003)

[54] Y. H. Lee, S. G. Kim and D. Tomanek, Physical Review Letters **78** (12), 2393 (1997)

[55] O. A. Louchev, Y. Sato and H. Kanda, Applied Physics Letters **80** (15), 2752 (2002)

[56] B. Lewis and J. C. Anderson, *Nucleation and Growth of Thin Films*. (Academic Press Inc., 1979) 518 pp.

[57] O. A. Louchev and J. R. Hester, Journal of Applied Physics **94** (3), 2002 (2003)

[58] A. Ural, Y. M. Li and H. J. Dai, Applied Physics Letters **81** (18), 3464 (2002)

[59] Yihong Wu and Bingjun Yang, Nano Letters **2** (4), 355 (2002)

[60] M. Senthil Kumar, T. H. Kim, S. H. Lee *et al.*, Chemical Physics Letters **383** (3-4), 235 (2004)

[61] B. W. Smith, Z. Benes, D. E. Luzzi *et al.*, Applied Physics Letters **77** (5), 663 (2000)

[62] David Nicholson, Surface Science Letters **181** (3), L189 (1987)

Reproduced with permission of the copyright owner. Further reproduction prohibited without permission.

[63] Gabor A. Somorjai, *Introduction to Surface Chemistry and Catalysis*. (Wiley, New York, 1994) 667 pp.

[64] Richard I. Masel, *Principle of Adsorption and Reaction on Solid Surface*. (Wiley, New York, 1996) 804 pp.

[65] M. S. Dresselhaus, G. Dresselhaus and P. C. Eklund, *Science of Fullerenes and Carbon Nanotubes*. (Academic Press, San Diego, 1996) 965 pp.

[66] Edward A. Mason and Joseph T. Vanderslice, Physical Review **108** (2), 293 (1957)

[67] W. D. Davis and T. A. Vanderslice, Physical Review **131** (1), 219 (1963)

[68] Nobuki Mutsukura, Kenji Kobayashi and Yoshio Machi, Journal of Applied Physics **68** (6), 2657 (1990)

[69] H. W. Wei, K. C. Leou, M. T. Wei *et al.*, Journal of Applied Physics **98** (4) (2005)

[70] P. Colpo, T. Meziani and F. Rossi, Journal of Vacuum Science and Technology A: Vacuum, Surfaces, and Films **23** (2), 270 (2005)

Reproduced with permission of the copyright owner. Further reproduction prohibited without permission.

Appendix A: Acronyms

0-D: Zero-dimensional

1-D: One-dimensional

2-D: Two-dimensional

3-D: Three-dimensional

AE: Auger electron

AES: Auger electron spectroscopy

AFM: Atomic force microscopy

BET: Brunauer-Emmett-Teller

BSE: Back-scattered electron

CCP: Capacitively coupled plasma

CNF: Carbon nanofiber, carbon nanoflake

CNS: Carbon nanosheet

CNT: Carbon nanotube

Reproduced with permission of the copyright owner. Further reproduction prohibited without permission.

CNW: Carbon nanowall

CVD: Chemical vapor deposition

DC: Direct current

ECR: Electron cyclotron resonance

EDS: Energy dispersive spectroscopy

EMI: Electromagnetic interference

ERDA: Elastic recoil detective analysis

FE: Field emission

FEA: Field emission array

FTIR: Fourier transform infra-red

GAXRD: Glancing angle X-ray diffraction

GIAB: Grazing incidence asymmetric Bragg

GIXS: Grazing incidence X-ray scattering

HOPG: Highly ordered pyrolytic graphite

HRTEM: High resolution transmission electron microscopy

ICP: Inductively coupled plasma

MW: Microwave

MWNT: Multi-walled carbon nanotube

Reproduced with permission of the copyright owner. Further reproduction prohibited without permission.

NSL: Nanosphere lithography

OES: Optical emission spectroscopy

PECVD: Plasma enhanced chemical vapor deposition

PIXE: Particle induced X-ray emission

RBM: Radial breathing mode

RF: Radio frequency

SAD: Selected area electron diffraction

SE: Secondary electron

SEM: Scanning electron microscopy

SPM: Scanning probe microscopy

STEM: Scanning transmission electron microscopy

STM: Scanning tunneling microscopy

SWNT: Single-walled carbon nanotube

TDS: Thermal desorption spectroscopy

TEM: Transmission electron microscopy

XPS: X-ray photoelectron spectroscopy

XRD: X-ray diffraction

Reproduced with permission of the copyright owner. Further reproduction prohibited without permission.

VITA

Mingyao Zhu was born in Gaoyou, Jiangsu Province, China on May 28, 1975. She graduated from Gaoyou High School in June 1994, after which she went to Nankai University, Tianjin, China, to study in Physics Department in Sept. 1994. She received her Bachelor of Science degree with a concentration in Applied Physics in July 1998. She was admitted to the graduate program in the same department to study in biophysics. In Aug. 2000, she entered the Physics Department of the College of William and Mary in Virginia, and received her Master of Science degree in 2002.

Reproduced with permission of the copyright owner. Further reproduction prohibited without permission.